UTTAC
ANNUAL REPORT 2018

TANDEM ACCELERATOR COMPLEX
Research Facility Center for Science and Technology
University of Tsukuba

https://www.tac.tsukuba.ac.jp/

UTTAC

ANNUAL REPORT 2018

April 1, 2018– March 31, 2019

Editors : Tetsuaki Moriguchi, Kimikazu Sasa, Yoshihiro Yamato, Masumi Matsumura, Masao Sataka, Hiroshi Naramoto, and Hiroshi Kudo (editor-in-chief)

PREFACE

This annual report covers researches carried out at University of Tsukuba Tandem Accelerator Complex (UTTAC) during the fiscal year 2018 (1 April 2018 ~ 31 March 2019). The topics include not only accelerator-based researches using the 6MV Pelletron and 1MV Tandetron accelerators, but also radioisotope-based researches including positron annihilation spectroscopy and Mössbauer spectroscopy.

September 2, 2019
Editorial board

HIGH SCHOOL STUDENTS MEET ADVANCED SCIENCE AT UTTAC

In FY2018, UTTAC has accepted totally 571 visitors, consisting of 397 high school students. Indeed, one of the important roles of the UTTAC facility is the promotion of physical science to young generation.

High school students listening to the staff's explanation of a series of electronic control systems at the experimental room of the Tandetron accelerator.

Number of yearly visitors to UTTAC from FY2013 to FY2018.

CONTENTS

5. BEAM IRRADIATION EFFECT

6. LIST OF PUBLICATIONS AND PRESENTATIONS

7. THESES·· 65

8. LIST OF PERSONNEL··· 67

1.

ACCELERATOR AND RELATED FACILITIES

1.1 Accelerator operation 2018

K. Sasa, S. Ishii, Y. Tajima, T. Takahashi, Y. Yamato, M. Matsumura, T. Moriguchi, A. Uedono

1 MV Tandetron accelerator

The operating time and the experimental beam time of the 1 MV Tandetron accelerator were 429 and 180.1 hours, respectively, during the total service time in fiscal 2018. A total of 46 days was used for beam experiments. A total of 135 researchers and students used the 1 MV Tandetron accelerator in fiscal 2018. Figures 1 and 2 show classification of the accelerated ions and of the experimental purposes, respectively. This accelerator was maximally used for RBS/ERDA which occupied 60.6% of the beam time. It should be noted that 4.5% of the beam time was used for RBS/ERDA by external users.

We performed alignment adjustment for the beam transport because there was an axis deviation after the earthquake in 2011. The accelerator tank was lifted up by about 1 cm for the alignment adjustment in the periodic maintenance in March 2019.
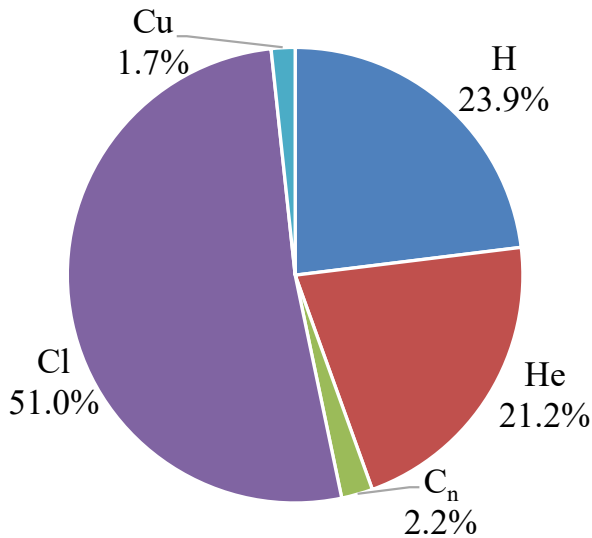
Fig. 1. Accelerated ions by the 1 MV Tandetron accelerator in fiscal 2018.
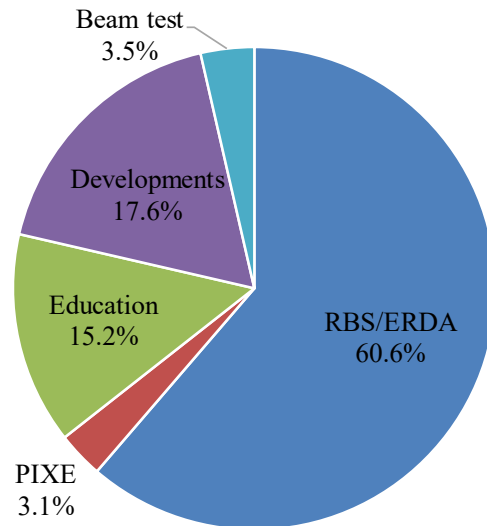
Fig. 2. Purpose of use of the 1 MV Tandetron accelerator in fiscal 2018.

6 MV Pelletron tandem accelerator

The operating time and the experimental beam time of the 6 MV Pelletron tandem accelerator were 1633.6 and 1286.4 hours, respectively, during the total service time in fiscal 2018. The total number of operation days was 115 in fiscal 2018. 60 research programs were carried out and a total of 459 researchers used the 6 MV Pelletron tandem accelerator in fiscal 2018. Figure 3 shows the beam time histogram with respect to the terminal voltage. Figures 4 and 5 show classification of the accelerated ions and of the experimental purposes, respectively. The operating time at the terminal voltage of 6 MV accounted for 60.1% of all the beam time. This accelerator was used most often for AMS which occupied 69.4% of the beam time. The next 16.8% was occupied by IBA using a micro beam, mainly for analysis of structural materials in the Strategic Innovation Promotion Program: SIP [1].

There was a major trouble in fiscal 2018 with the foil changer in the accelerator terminal, which caused

malfunction to circulate the carbon foil unit, as was the same trouble in the previous cases [2, 3]. We opened the accelerator tank and repaired the foil changer in March 2019.
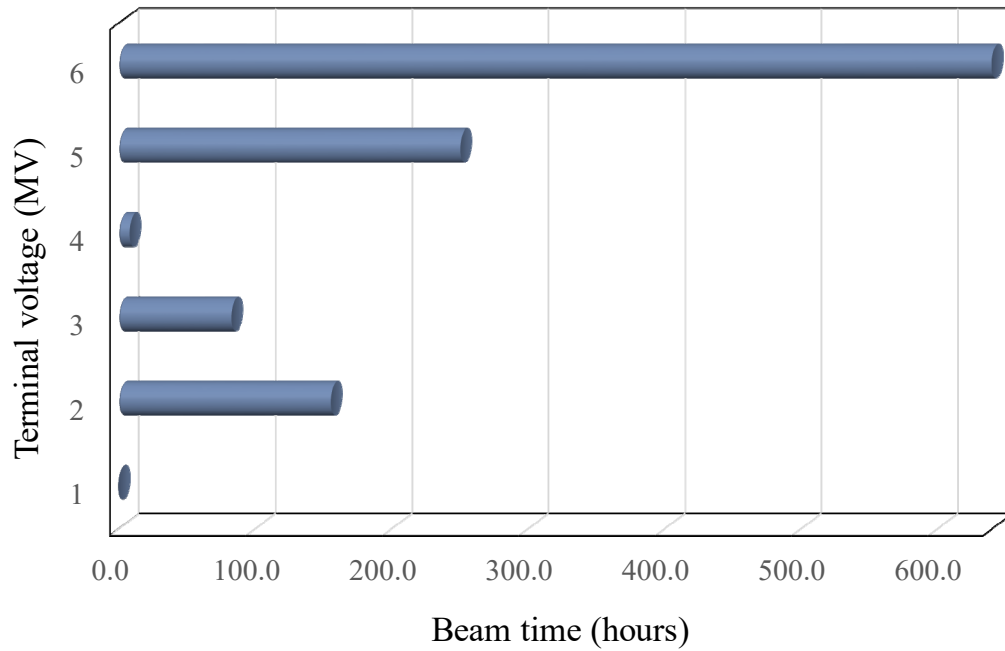
Fig. 3. Beam time histogram as a function of the terminal voltage for the 6 MV Pelletron tandem accelerator in fiscal 2018.
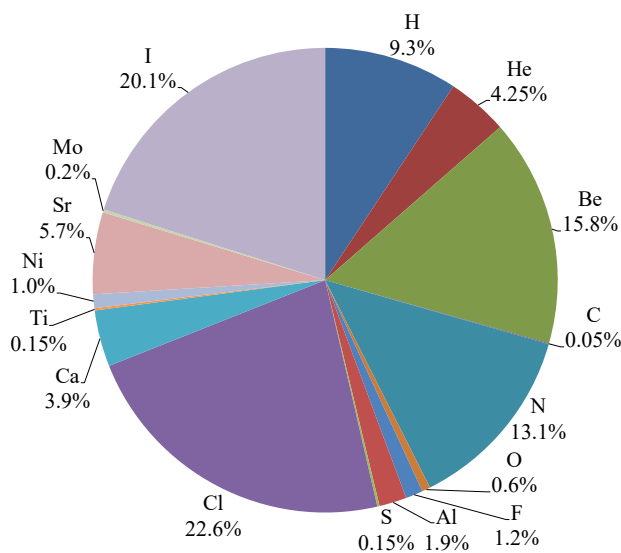
Fig. 4. Accelerated ions for the 6 MV Pelletron tandem accelerator in fiscal 2018.
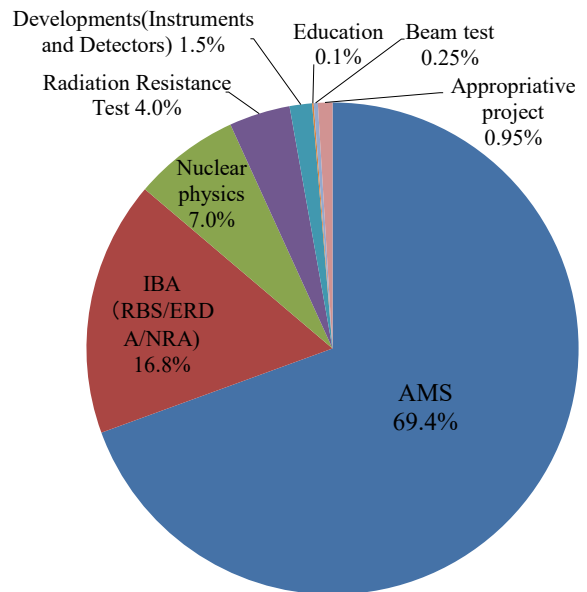
Fig. 5. Purpose of use of the 6 MV Pelletron tandem accelerator in fiscal 2018.

References

[1] SIP-IMASM: https://unit.aist.go.jp/tia-co/project/SIP-IMASM/index.html
[2] K. Sasa et al., UTTAC ANNUAL REPORT 2016, UTTAC-86 (2017) 1.
[3] K. Sasa et al., UTTAC ANNUAL REPORT 2017, UTTAC-87 (2018) 1.

1.2 Improvement of the Lamb-shift polarized ion source

T. Moriguchi, Y. Yamato, A. Ozawa, M. Mukai, D. Kamioka, R. Kagesawa

The Lamb-shift polarized ion source (PIS) is one of the ion sources installed at the 6 MV Pelletron tandem accelerator at UTTAC which has been operated since March 2016 [1]. PIS makes it possible to produce highly polarized negative proton and deuteron beams whose spin polarizations are approximately 80%. At present, PIS is mainly used for measuring nuclear moments of unstable nuclei [2]. In FY2017, we measured the spin polarization of the proton beam accelerated to 12 MeV, which was approximately 40%, and found that the depolarization occurred during the beam transport from PIS to the beam course [3, 4]. In this report, we refer to improvements for higher polarization as well as for stable operation of PIS.

One of the possibilities for the depolarization might be the electron exchange between the ions and residual gas in the beam duct. Indeed, defects of attachment around the previous valve were found when a stripper gas valve in the accelerator terminal was replaced with a new one in March 2018 [5]. It is therefore probable that the SF_6 gas in the accelerator tank leaks into the gas stripper canal, hence causing the depolarization. After repairing the attachment, we measured the spin polarization of the polarized proton beam at 12 MeV with a polarimeter using the p-^{4}He elastic scattering. The experimental method is the same as the previous one [3, 4]. The spin quantization axis was set to be perpendicular to the horizontal plane, and accordingly the spin direction was either upward (spin-up) or downward (spin-down). The scattered protons were detected by two silicon detectors on the left and right sides of the polarimeter. Figure 1 shows energy spectra measured with the silicon detectors, where the peak energy at ~370 channel corresponds to the elastically scattered protons. In the present measurement, the spin polarization of the proton beam was improved to approximately 60% in both spin-up and spin-down cases. This corresponds to a 20% increase compared with the previous case [3, 4]. However, cause of the depolarization is not completely elucidated yet. For example, the residual argon gas in the stripper canal, even when closing the stripper gas valve, might induce the depolarization.
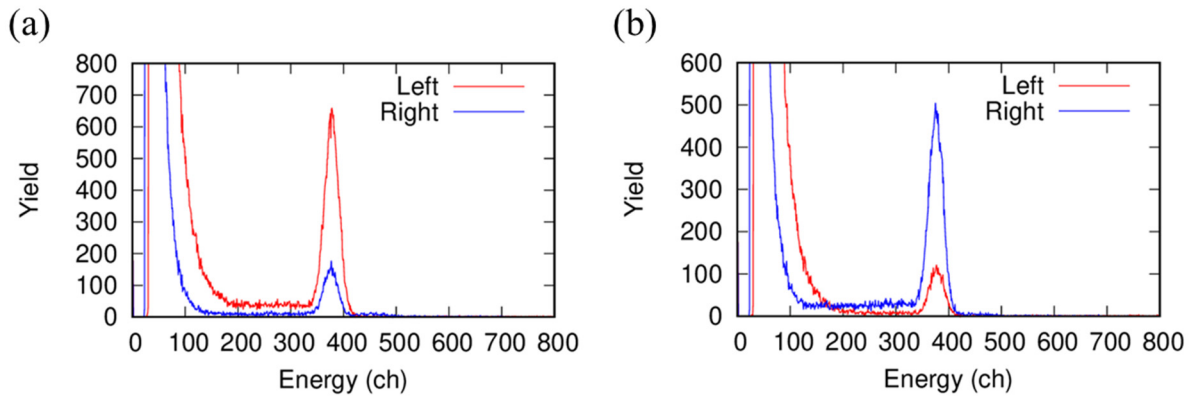
Fig. 1. Energy spectra obtained with silicon detectors at the left (red line) and the right (blue line) sides of the polarimeter. Shown in (a) and (b) are the results for spin-up and spin-down, respectively.

In FY 2018, we improved parts of PIS for its stable operation. Several electrodes for the extraction of ions in the duoplasmatron chamber were replaced with new ones because degradation of the vacuum condition and frequent discharges occurred by the leak of silicone fluid for cooling the electrodes. One of these electrodes is of the cylindrical type referred to as "middle electrode (ME)" as shown in Fig. 2 (a). The LaB_6 filament is mounted in ME, and positive ions are extracted from the center hole of ME. The cesium cell was also replaced with a new one because of the leak of circulating hot water which liquefies the cesium vapor to return to the reservoir attached with heater. Figure 2 (b) shows a photo of the new cesium cell. At present, we plan to change the variable leak valve for hydrogen gas supply to a high performance one.
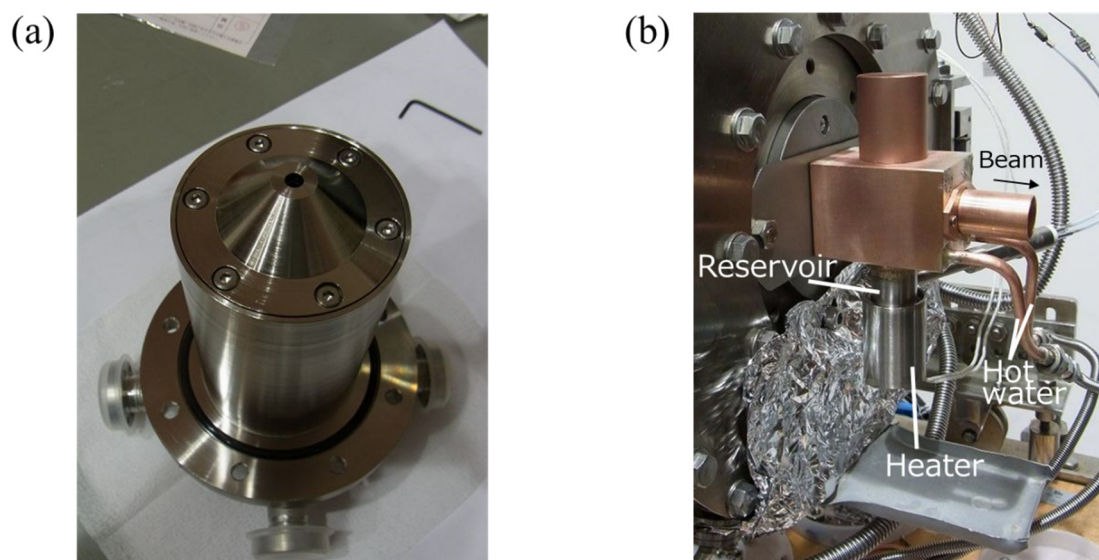
Fig. 2. Photos of (a) the middle electrode and (b) the cesium cell, which replaced the old ones in FY 2018.

References

[1] K. Sasa et al., UTTAC Annual Report 2015, UTTAC-85 (2016) 1.
[2] A. Ozawa et al., this Annual Report §2.1.
[3] T. Moriguchi et al., UTTAC Annual Report 2017, UTTAC-87 (2018) 3.
[4] T. Moriguchi et al., Proceedings of Science, PSTP2017 (2018) 018.
[5] K. Sasa et al., UTTAC Annual Report 2017, UTTAC-87 (2018) 1.

1.3 Approach to possible maximum energies of ions accelerated by the 6 MV tandem accelerator

M. Sataka, T. Takahashi, H. Naramoto, H. Kudo, K. Sasa

A series of ion acceleration tests with the 6MV tandem accelerator has been continued for 3 years [1, 2]. Actually, at three terminal voltages of 1, 3, and 6 MeV the beam current of the accelerated ion is measured as a function of the ion's charge state. For a given ion species, the highest charge state determines the highest beam energy obtainable from the accelerator. In this fiscal year, N, Al, S, and Mo ions were tested. Here, we describe the test results at the terminal voltage of 6 MV.

Figure 1 shows the beam current distributions of sulfur ions as a function of the charge state at the terminal voltage of 6 MV. Either argon gas or a carbon foil was used as a charge-changing stripper at the high-voltage terminal. The gas pressure was about 5−7 µPa, and the thickness of the carbon foil was about 5 µg/cm^2. When the foil stripper is used, the incident ion beam was weak enough to avoid radiation damage of the foil. The ion current distribution for the foil stripper shifts to higher charge state by 3 than for the gas stripper. For both the foil and the gas strippers, the practically available maximum energy obtained for sulfur ion is 66 MeV, employing the charge state of 10.
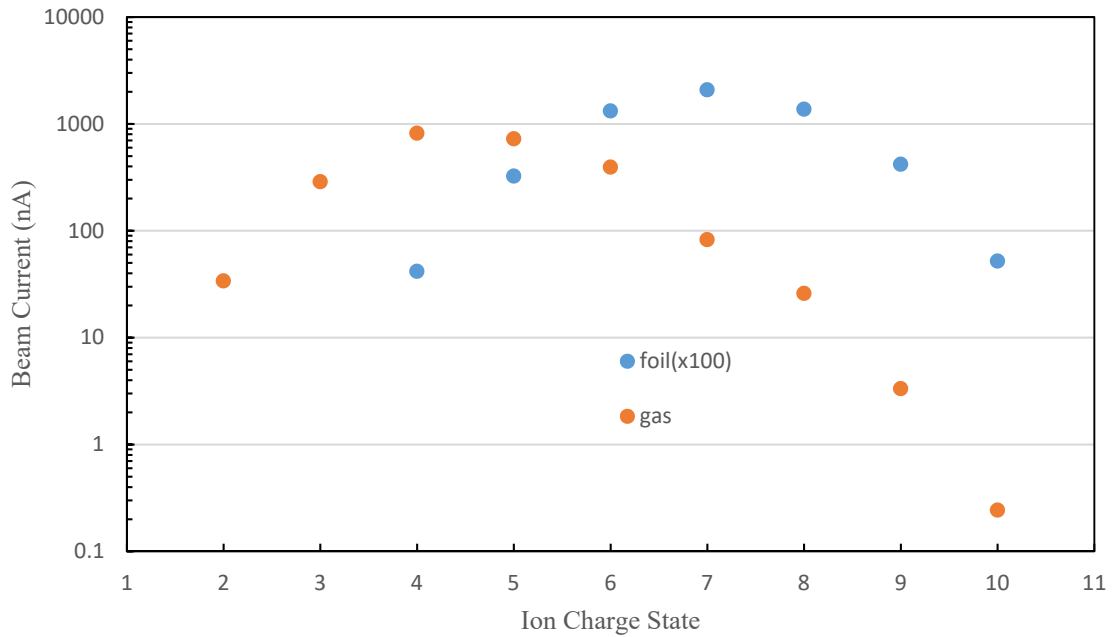
Fig. 1. Ion beam current distribution for sulfur ion at the terminal voltage of 6MV. Either the gas or the foil stripper was used at the high-voltage terminal.

In FY2018, we tested injection of negatively charged molecular ions (including cluster ions) to obtain ion beams of N, Al and Mo. In this case, the beam energy cannot be determined uniquely from the terminal voltage and the ion's charge state. The maximum acceleration energies in this test are about 39, 51, 65, and 71 MeV for N, Al, Mo, and W ions, respectively. Table 1 shows the summary of the acceleration test of N, Al, Mo and W ions. Table 2 shows the revised summary for injection of negatively charged single-atom ion,

which is based on the data collected from 2016 to 2018 for the 6 MV terminal voltage. For atomic Al (monomer) acceleration, the beam current is about one fifth of that for Al_2 (dimer) ion.

Table 1. Ion current distribution of N, Al, Mo, and W at the terminal voltage of 6MV.
The measured beam intensity is shown by the symbols: ○: ≥ 1nA, △: <1nA.

Charge state	N	Al	Mo	W
14				
13				
12				
11				△
10			△	△
9		○	△	○
8		○	△	○
7		○	○	
6	△	○	○	
5	○	○	○	
4	○		○	
3	○			
2	○			
1				

Table 2. The summary of the acceleration test for atomic negative ion injection at the terminal voltage of 6MV, carried out from 2016 to 2018. The measured beam intensity is shown by the symbols: ○: ≥ 1nA, △: <1nA. The results obtained with the foil stripper are shown in red.

Charge state	Energy (MeV)	H	He	Li	B	C	O	F	Al	Si	S	Cl	Ni	Br	Ag	I	Au
14	90													△(red)	△	○	△
13	84													△	△	○	△
12	78												△	○	○	○	○
11	72									○(red)			○	○	○	○	○
10	66								○(red)	○	○(red)		○	○	○	○	○
9	60								○	○	○	○(red)	○	○	○	○	○
8	54							○(red)	○	○	○	○	○	○	○	○	○
7	48						○	○	○	○	○	○	○	○	○	○	
6	42					○	○	○	○	○	○	○	○	○	○		
5	36				○	○	○	○	○	○	○	○	○	○	○		
4	30				○	○	○	○		○	○	○	○	○			
3	24			○	○	○	○	○		○	○		○				
2	18		○	○	○	○	○	○			○						
1	12	○	○	○	○												

References

[1] M. Sataka et al., UTTAC Annual Report 2016, UTTAC-86 (2017) 9.

[2] M. Sataka et al., UTTAC Annual Report 2017, UTTAC-87 (2018) 5.

2.

NUCLEAR AND ATOMIC PHYSICS

2.1 Measurements of magnetic moments of ^{29}P and ^{25}Al

A. Ozawa, T. Moriguchi, Y. Yamato, R. Kagesawa, D. Kamioka, M. Mukai

We are attempting to produce polarized unstable nuclei by using polarized proton beams for the aim of measuring nuclear moments of unstable nuclei. In FY2017, we have succeeded to produce and detect polarized unstable nuclei by using E_p=12 MeV with a Si target [1].

In FY2018, we have tried to measure nuclear magnetic moments (μ) of ^{29}P ($T_{1/2}$=4.2 s) and ^{25}Al ($T_{1/2}$=7.2 s) by using our nuclear magnetic resonance system for β-rays (β-NMR system). The μ values of ^{29}P and ^{25}Al have been reported in Refs. [2] and [3], respectively. Experimental setup in our β-NMR system was already described in Ref. [1]. In the present work, a 0.5 mm thick Si target placed in our β-NMR system was irradiated with a polarized proton beam accelerated to 12 MeV by the 6 MV tandem accelerator. The proton polarization-degree was about 70 %. In this work, to search μ for ^{29}P and ^{25}Al in our β-NMR system, we changed the static magnetic field instead of the radio frequency (RF) scanning, where RF was fixed to 4.75-5.25 MHz.

Figure 1 shows the NMR spectrum observed in the present experiment. We observed two clear resonances in the spectrum. In Fig. 1, values of the current corresponding to the previously measured μ for ^{29}P and

Fig. 1. NMR spectrum measured using a 12 MeV polarized proton beam with a Si target. RF was fixed to 4.75-5.25 MHz. Open circles indicate the data without RF. Arrows show values of the current corresponding to the previously measured μ for ^{29}P (left) and ^{25}Al (right), respectively.

^{25}Al are shown by arrows. Resonances observed in the present work are well consistent with the previously measured μ. Thus, we succeeded to measure μ of ^{29}P and ^{25}Al in our β-NMR system. In the next step, we will try to measure unknown nuclear moments, such as μ of ^{30}P ($T_{1/2}$=150 s).

References

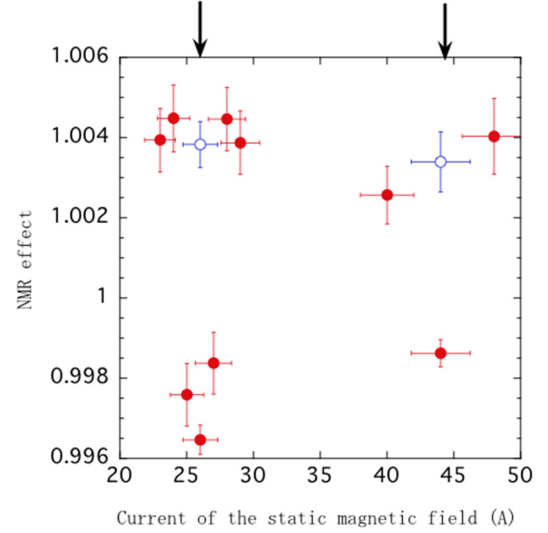[1] A. Ozawa et al., UTTAC Annual Report 2017 (2018) 7.
[2] K. Sugimoto et al., in Hyperfine Interactions in Excited Nuclei, edited by G. Goldring and R. Kalish (Gordon and Breach, New York, 1971), p. 325.
[3] T. Minamisono et al., Phys. Rev. C 14 (1976) 376.

2.2 Development of a position-sensitive detector using scintillating fibers

T. Yamaguchi[1,2], Y. Inada[2], S. Hosoi[2], R. Kagesawa, T. Moriguchi, A. Ozawa

In this study, we develop position-sensitive detectors using thin scintillating fibers and shaped plastic scintillators for the Rare-RI Ring facility at RIKEN RI Beam Factory [1]. In high-energy RI beam facilities, well-established gas position-sensitive detectors such as parallel plate avalanche counters (PPAC) [2] are used for beam diagnostics. As the Rare-RI Ring facility has many focal planes in an approximately 160-m-long injection beam line, numerous detectors are required for beam diagnostics. However, operating and maintaining these types of detectors can be expensive and often time-consuming. In addition, in-ring position-sensitive detectors are necessary for precise beam tuning during the injection phase. Because the Rare-RI Ring stores only a single particle at every injection, conventional beam instruments are not available. Thus, simple, compact, low-cost position-sensitive detectors with single ion sensitivity must be developed.

Thus far, we have developed a simple prototype detector that uses plastic scintillation bars with multi-pixel photon counters using a simple readout method [3]. The prototype has been shown to measure successfully the position distributions of heavy ions. This detector can be used in the injection beam line as well as in the storage ring on a movable platform. The present study is an extension of this direction. We produced a prototype of a long scintillating fiber detector to observe decay particles of stored ions in the storage ring. The detector will be installed along the circumference of an approximately 60-m storage ring. The original concept and results of experiments conducted at the HIMAC facility [4] will be published elsewhere [5].

In this study, we performed a detector test experiment at the 6-MV tandem accelerator facility at the University of Tsukuba. The prototype consists of nine scintillating fibers (Kuraray SCSF-78J, 2×2 mm and 2 m long) arranged to form a flat plane of 18 mm $\times$ 2 m as shown in Fig. 1. Each end of the nine scintillating fibers was assembled and connected to a common multi-pixel photon counter (MPPC S13360-6075CS Hamamatsu).

Fig. 1. Photograph of nine scintillating fibers forming a plane. The inset shows the cross section of the nine fibers before being connected to the MPPC.

A 12-MeV proton beam was used to test the detector response. The beam was incident on a 2.5-μm

thick Au foil placed at the target chamber of the A7 course. The protons scattered at $30°$ were directed on the prototype. By moving the detector, we changed the position of the beam spot every 40 cm. The timing and charge differences of the scintillation light pulses propagated to each end of the scintillating fibers were measured.

A position correlation was successfully observed, as shown in Fig. 2, where the plotted ratio T_{ratio} is sensitive to the beam hit position and is defined as

$$T_{\text{ratio}} = \frac{T_{\text{left}} - T_{\text{right}}}{T_{\text{left}} + T_{\text{right}}},$$

where T_{left} and T_{right} are the timing of the left and right fibers, respectively, as measured by a time-to-digital converter (TDC). The position resolution was approximately 2 cm. The charge difference was approximately 6 cm, the result that must be improved. Further developments are ongoing.

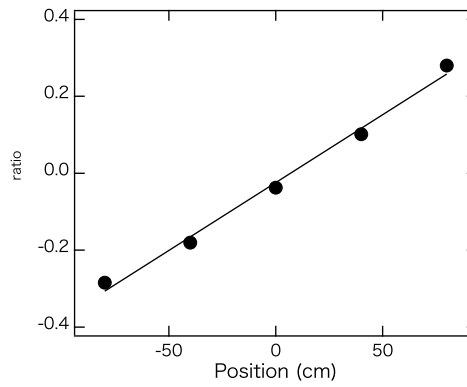Fig. 2. Position correlation of the timing difference observed for the proton beam.

References

[1] A. Ozawa et al., Prog. Theo. Exp. Phys. 2012 (2012) 03C009.

[2] H. Kumagai et al., Nucl. Instr. Meth. Phys. Res. B 317 (2013) 717.

[3] K. Wakayama et al., JPS Conf. Proc., to be published.

[4] M. Kanazawa et al., Nucl. Phys. A 746 (2004) 393c.

[5] K. Inomata et al., JPS Conf. Proc., to be published.

2.3   Generalization of a gain reduction model for the space charge effect in a wire chamber

Y. Kato[1], K. Fujii[1], S. Kajiwara[1], T. Mogi[1], N. Nagakura[1], D. Sekiba, Y. Sugisawa, S. Yamashita[2]

In our neutron lifetime precise measurement in J-PARC, we monitor and collect the tracks of proton and β-ray coincidently in a wire chamber. Under the condition that the parameters of the wire chamber are optimized to the β-ray detection, the output linearity for protons is crucially suffered from gain reduction due to the space charge effect. In order to collect the desirable events correctly, it is necessary to obtain the gain reduction factor s based on a phenomenological model.

A gain reduction model was previously proposed taking into account the self-induced space charge effect [1]. In this model, s is expressed as follows,

$$s \equiv \frac{\log(1 + fG_0 \frac{dE}{dl})}{fG_0 \frac{dE}{dl}}, \tag{1}$$

where f is a constant factor including all microscopic characteristics of the space charge effect, which determines the absolute scale of gain reduction, G_0 is the multiplication factor without the space charge effect, dE/dl is the energy loss per wire length.

We have conducted experimental verification of this model since last year with a multi-wire drift chamber (MWDC) filled with a mixed gas of He and CO_2 and a proton beam from the Tandetron accelerator at UTTAC. As a result, we determined the factor f under the condition of 85 kPa He gas and 15 kPa CO_2 gas, as shown in Fig. 1, and succeeded in correcting the gain reduction, as is seen in Fig. 2. For details, see Ref. [2].
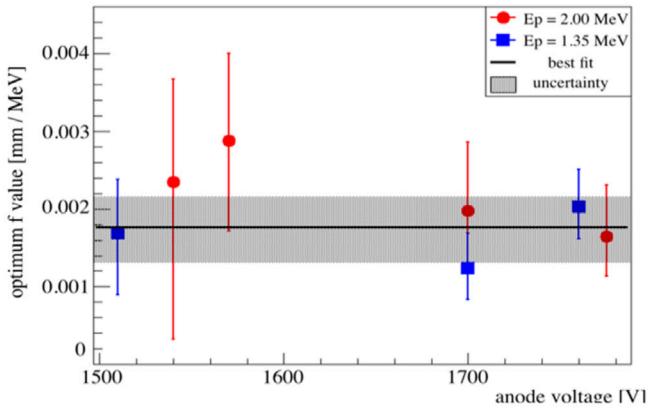
Fig. 1. Values of f derived for the proton energies of $E_p =$1.35 and 2.00 MeV as a function of the applied anode wire voltage. The f values seem to be a constant within the present uncertainties.
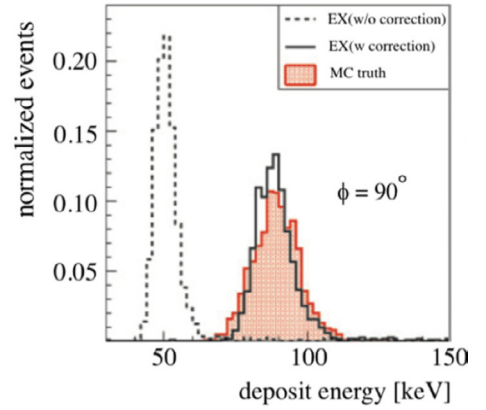
Fig. 2. The experimental energy deposit distributions with and without the correction of the gain reduction, together with the simulation results.

[1]Graduate School of Science, University of Tokyo
[2]International Center for Elementary Particle Physics, University of Tokyo

Although the validity of this model has been proved as described above, it is necessary to re-determine f in advance for application of the current model to other measurement. Hence, in this study, we aim to generalize this model, and in particular to evaluate the gas dependence of f.

In the model, f is defined as $f \equiv eBC/2\pi\varepsilon aw$, where e is the elementary charge, a is the anode wire radius, w is the average energy loss per electron-ion pair creation by the incident charged particle (w-value), B is a coefficient under the assumption that the multiplication factor exponentially depends on the electric field, and C is a coefficient describing the space charge effect [2] which should be approximately 1. According to the Diethorn's formula [3], assuming the Townsend coefficient α to be proportional to the electric field, the coefficient B should be proportional to a/w. Therefore f should be proportional to $1/w^2$.

To verify the dependence of f on the gas condition, we are going to measure gain reduction under several gas conditions. Change in the gas condition should lead to the change in the diffusion coefficient during electron drift, and therefore, affect the gain reduction. To extract only the effect of diffusion, it is necessary to measure the gain reduction while changing the total pressure of the same gas.

At present, MWDC is upgraded by implementation of the field cage to stabilize drift electric field and expansion of the sense area by increasing the number of wires, as shown in Fig. 3. In addition, we acquired data for 2 MeV H^+ with upgraded MWDC filled with a mixed gas of 85% He and 15% CO_2 to confirm the reproduction of the previous result in the current setup. The total gas pressure was changed to 40, 60, 80, and 100 kPa to evaluate the effect of electron diffusion during drift step. Analysis is currently in progress.

The next step is to measure the gain reduction with different gases. We are planning to use a mixed gas of 90% Ar and 10% CH_4, and finally to verify w-dependence of f.
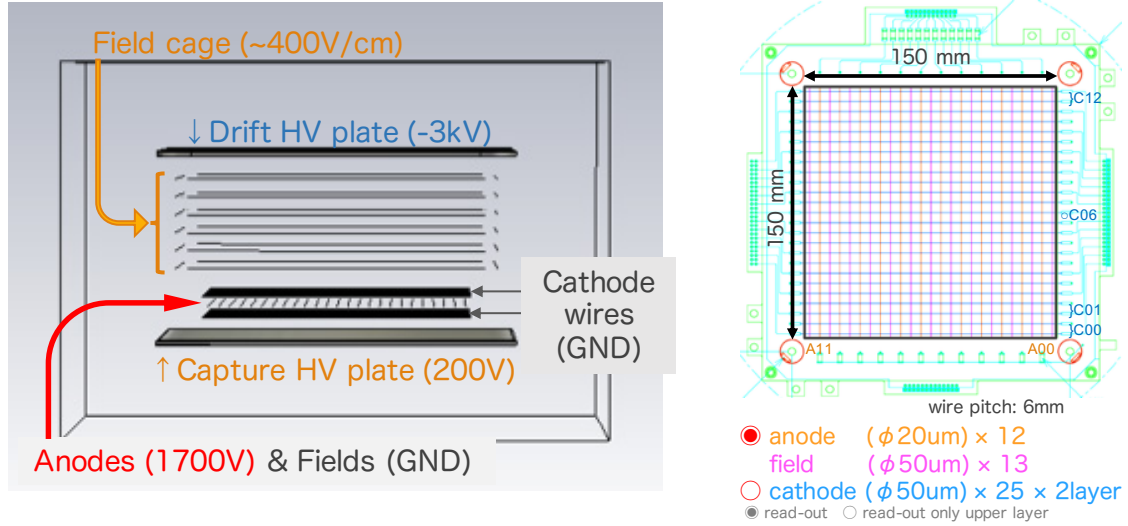
Fig. 3. The schematic layout of the upgraded MWDC.

References

[1] Y.Arimoto et al., Nucl. Instr. Meth. Phys. Res. A 799 (2015) 187.
[2] N. Nagakura et al., Prog. Theor. Exp. Phys. 013C01 (2018).
[3] W. Blum et al., "Particle Detection with Drift Chambers", Springer (2008).

3.

ACCELERATOR MASS SPECTROMETRY

3.1 Performance report of the Tsukuba 6 MV multi-nuclide AMS system in fiscal 2018

K. Sasa, T. Takahashi, K. Takano, Y. Ochiai, Y. Ota, M. Matsumura, T. Matsunaka[1], A. Sakaguchi, K. Sueki

The AMS system on the 6 MV tandem accelerator was operated for a total of 55 days in fiscal 2018. We measured 735 samples in total dealing with rare radionuclides such as ^{10}Be, ^{26}Al, ^{36}Cl, ^{41}Ca, ^{90}Sr and ^{129}I shown in Table 1. Figure 1 shows a breakdown by types of measured nuclides. Figure 2 shows monthly-measured nuclides from April 2018 to March 2019. ^{36}Cl and ^{129}I were measured most frequently in fiscal 2018 in order to investigate the radioactive contamination in rainwater and soil samples, caused by the Fukushima Daiichi Nuclear Power Plant accident. ^{129}I was also applied for the tracer of oceanic circulation in the Japan Sea. ^{10}Be and ^{36}Cl were applied for the tracer of cosmic ray events in the ice core and variations of solar activity. In addition, we have tried to develop new techniques for ^{90}Sr-AMS.

Table 1. Number of measured samples in fiscal 2018.

Nuclides	Number
Be-10	180
Al-26	13
Cl-36	196
Ca-41	23
Sr-90	29
I-129	294
Total	**735**
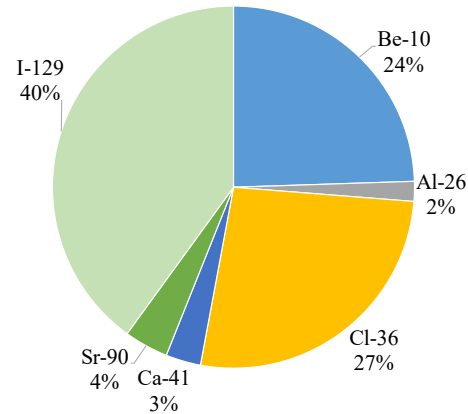
Fig. 1 Measured nuclides by the multi-nuclide AMS system in fiscal 2018.

Change in month

Fig. 2. Monthly-measured nuclides by the multi-nuclide AMS system from April 2018 to March 2019.

---

[1] Kanazawa University

We have developed ultrasensitive detection techniques for ^{10}Be, ^{14}C (graphite and CO_2), ^{26}Al, ^{36}Cl, ^{41}Ca, and ^{129}I in isotopic-ratio ranges of 10^{-10} to 10^{-16} with the multi-nuclide AMS system. AMS has satisfactory performance for analysis of cosmogenic nuclides in the geo-environmental resear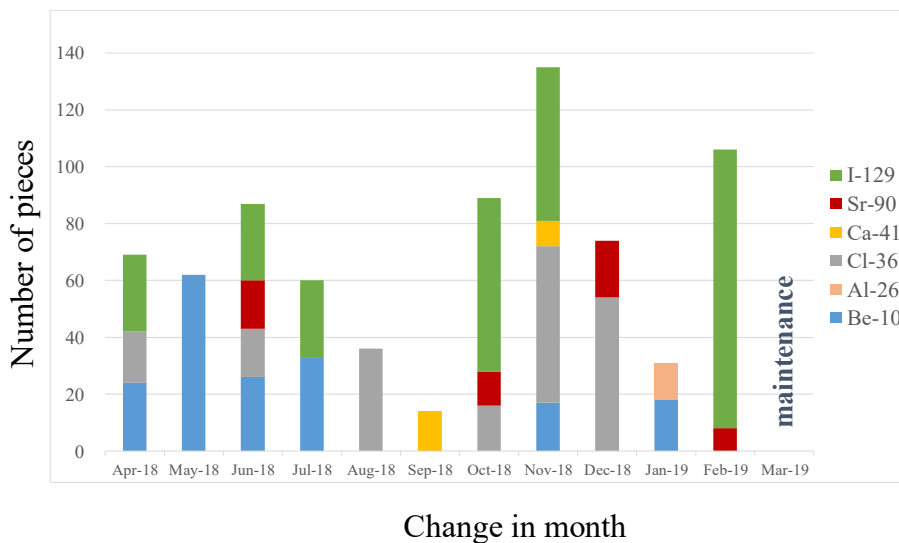ch. In fiscal 2018, we developed the sulfur removal method to reduce ^{36}S contamination in ^{36}Cl AMS. AgCl samples were pressed into an AgBr backing in a large Cu sample cathode (6 mm diameter). The sensitivity improvement due to the suppression of ^{36}S has been investigated [1]. ^{36}Cl measurements were performed at a 6.0 MV terminal voltage with a carbon stripper foil of 4.8 μg cm^{-2}. The analyzed charge state was 8+, hence ^{36}Cl^{8+} was injected into the detector at 54.0 MeV. A Si$_3$N$_4$ foil of 75 nm thickness was used for the detector window under an isobutane pressure of 38 Torr. ^{36}Cl$^-$ beam transmission was ~10%. AgCl blank samples were prepared from ACS-grade NaCl (Fisher Scientific, USA). The ^{36}Cl/Cl background was less than 3×10^{-15} with a run time of 500 s. Table 2 shows the performance summary of the Tsukuba 6 MV multi-nuclide AMS system since for the first two years of operation since 2016 [2].

Table 2. Performance summary of the Tsukuba 6 MV multi-nuclide AMS system.

Isotope	^{10}Be	^{14}C	^{26}Al	^{36}Cl	^{41}Ca	^{129}I
Chemical form	BeO	Graphite, CO_2	Al$_2$O$_3$	AgCl	CaF$_2$	AgI
Injected ion	BeO$^-$	C$^-$	Al$^-$	Cl$^-$	CaF$_3$$^-$	I$^-$
Typical ion current (μA)	1 − 5 (^{9}Be^{16}O$^-$)	5 [CO_2]− 60 (^{12}C$^-$)	0.2 (^{27}Al$^-$)	5 − 15 (^{35}Cl$^-$)	0.5 (^{40}Ca^{19}F$_3$$^-$)	1 − 8 (^{127}I$^-$)
Terminal voltage (MV)	6.0	5.0	6.0	6.0	6.0	5.0
Detected ion (stripper)	^{10}Be^{3+} (gas)	^{14}C^{4+} (gas)	^{26}Al^{5+} (gas)	^{36}Cl^{8+} (foil)	^{41}Ca^{5+} (foil)	^{129}I^{5+} (gas)
Beam energy (MeV)	20.3	25.0	36.0	54.0	32.5	30.0
Transmission (%)	30	40	25	10	10	10
Detector conditions						
Absorber cell	Havar (5 μm) + Ar (71.5 Torr)	–	–	–	–	–
Window material (thickness)	Mylar (6 μm)	Mylar (6 μm)	Si$_3$N$_4$ (75 nm)	Si$_3$N$_4$ (75 nm)	Si$_3$N$_4$ (75 nm)	Polyester (1.5 μm)
Detector gas (pressure)	P10 (75.5 Torr)	P10 (70 Torr)	Isobutane (19.5 Torr)	Isobutane (38 Torr)	Isobutane (16 Torr)	Isobutane (19 Torr)
Counting rate (cps)	120	115 (Graphite)	2	65	15	8.5
Sample to reference ratio	2.7×10^{-11}	1.4×10^{-12}	7.4×10^{-11}	1.0×10^{-11}	1.2×10^{-10}	8.38×10^{-12}
Ratio of measured to nominal ratios	0.65	−	0.50	0.50	0.70	0.90
Precision (%)	2	0.2 (Graphite) 0.6 (CO_2)	3	2	3	1
Background (atomic ratio)	$<1 \times 10^{-15}$	$\sim 2.4 \times 10^{-16}$ (Commercial Graphite) $\sim 5 \times 10^{-15}$ (CO_2)	$<6 \times 10^{-15}$	$<3 \times 10^{-15}$	$<3 \times 10^{-15}$	$<1 \times 10^{-14}$

References

[1] S. Hosoya et al., Nucl. Instr. Meth. Phys. Res. B 438 (2018) 131.
[2] K. Sasa et al., Nucl. Instr. Meth. Phys. Res. B 437 (2018) 98.

3.2 Challenge to the measurement of ^{90}Sr by accelerator mass spectrometry – application to environmental samples

A. Sakaguchi, S. Yamasaki, S. Asai, K. Sasa, T. Takahashi, Y. Ochiai, K. Takano, M. Honda[1],
M. Matsumura, K. Sueki

The goal of this study is the measurement of low-level strontium-90 (^{90}Sr, $T_{1/2}$=28.90 year), which has rarely been measured in environmental samples due to the complicated nature of its chemical separation and the time-consuming requirements for such measurements. Nevertheless, its behavior and biological impact are important. To achieve the purpose, a new and efficient chemical separation method has to be developed and combined with accelerator mass spectrometry. Furthermore, it is necessary to find appropriate Sr precipitates/salts, which efficiently accumulate Sr from the chemically separated solution and, accordingly, provide an intensive Sr beam required for accelerator mass spectrometry.

Experiment 1. Precipitation methods for Sr targets   To achieve a high Sr precipitation yield from a purified Sr solution, $SrCO_3$, $SrSO_4$, $Sr_3(PO_4)_2$, $Sr(COO)_2$ (SrO^- beam emitter) and SrF_2, SrF_2+EuF_3 (Sr:Eu = 1:1, 1:4, 1:9) (SrF_3^- emitter) precipitations were produced, and the remaining supernatant Sr was measured with ICP-MS. The precipitations thus obtained were dried/ashed and pressed into the cathodes for the sputter ion source. Each cathode was sputtered with Cs^+, and the Sr beam intensity was measured using a Faraday cup. Analogue samples of SrO+ZrO_2 and SrF_2+ZrF_4 were also sputtered with Cs^+ to observe the intensities of interference Zr beams (ZrO^- or ZrF_3^-)

Experiment 2. Purification of Sr from natural water samples   In addition to the Sr resin method above [1], we hired MC1GEL (cation exchange resin) to remove zirconium (Zr) from the samples. Furthermore, a self-distilled reagent was also used for the final Sr solution. In combination with the appropriate precipitation method from Experiment 1, a blank sample was prepared. The signal counts from Zr for the blank sample were checked with an ionization chamber after accelerating the ions.

Experiment 3. Application of a lanthanide co-precipitation method   As for a lanthanide-fluoride co-precipitation method from Experiment 1, lanthanum (La), praseodymium (Pr), europium (Eu), thulium (Tm) and lutetium (Lu) coprecipitation methods were attempted. The precipitation yields and Sr ion beam intensity of each precipitation were observed using the same method as in Experiment 1.

For all the Sr precipitations, except for $Sr_3(PO_4)_2$ and SrF_2, the precipitation rates are in the range 89.9 to 98.8%. Of these precipitations, the best is thought to be SrF_2+EuF_3, which gives the highest Sr beam intensity and the lowest Zr intensity. The newly developed purification method for Sr showed a higher Sr chemical yield with a lower Zr intensity. In fact, the Zr count-rate of more than 100 kcps in the case of the previous method could be decreased to 1.5 kcps, and ^{90}Sr in an analogue riverine water sample (IAEA-PT-222) was measured as ^{90}Sr/^{88}Sr = 4.98×10^{-10} using ca. 400 ml of the sample. As for the lanthanide-fluoride co-precipitation methods, they showed a variety of Sr beam intensities depending on the lanthanide element used. Interestingly, a correlation between the Sr beam intensity and the first

---

ionization energy of lanthanide was found. The reason for this correlation is currently not clear, suggesting that further research is needed using other lanthanide elements.

Reference

[1] S. Hosoya, Developments of accelerator mass spectrometry for hardly measurable nuclides by 6MV tandem accelerator, Master thesis 2018, University of Tsukuba.

3.3 ^{36}Cl record in the Antarctic ice core around the AD774/5 cosmic-ray event and development of ^{10}Be AMS

K. Takano, K. Sasa, T. Takahashi, M. Matsumura, Y. Ochiai, K. Sueki, F. Miyake[1], K. Horiuchi[2], H. Matsuzaki[3]

Galactic cosmic rays are high energy particles that come to the earth from outside the solar system. They interact with atoms and molecules in the atmosphere, which is essential for the production of cosmogenic nuclides such as ^{14}C, ^{10}Be, ^{26}Al, and ^{36}Cl. Therefore, concentrations of cosmogenic nuclides reflect intensities of incoming cosmic rays. Miyake et al. [1] measured ^{14}C contents in tree rings with a time resolution of 1- to 2-year and found a large ^{14}C increase from AD 774 to AD 775 (AD 774/775 event). Moreover, Miyake et al. [2] measured ^{10}Be concentrations for the period approximately AD 763 – 794 in the Antarctic Dome Fuji ice core, and detected a significant increase of the ^{10}Be concentration around AD 775.

A multi-nuclide analysis provides original cosmic ray information, e.g. an energy spectrum of cosmic rays. We therefore investigated the temporal variation of ^{36}Cl concentration, corresponding to the case for another cosmogenic nuclide, in the ice core samples from the Dome Fuji around the periods where cosmic ray events were identified. ^{36}Cl is mainly produced in the atmosphere by the spallation reaction of incoming cosmic rays with ^{40}Ar, and it falls down and deposits in the ice core. We measured ^{36}Cl concentrations around AD 774/5 event using the 6 MV AMS system at the University of Tsukuba [3]. Each sample was taken at a depth interval of 20 cm which corresponds to a time resolution of ~4 year. We added Cl carrier of ~0.5 mg to each sample (approximately 100 – 120 g in weight), which resulted in the measured ^{36}Cl/Cl ratios of 8.0×10^{-14} – 12.3×10^{-14} around the AD 774/5 event. Table 1 shows that the ^{36}Cl concentrations in the Dome Fuji ice core are in the range of 0.9×10^4 to 1.4×10^4 atoms g^{-1}.

Table 1. ^{36}Cl concentrations in the Dome Fuji ice core around the AD 774/5 event.

Sample ID	Depth (m)	Year (AD)	Weight (g)	Cl conc. ($\times 10^4$ atoms g^{-1})	Error ($\times 10^4$ atoms g^{-1})
DF1-123-11 ~ DF1-123-14	57.6	792.7	121.9	0.89	0.05
DF1-124-1 ~ DF1-124-5	57.8	788.8	118.8	1.09	0.05
DF1-124-6 ~ DF1-124-10	57.9	784.6	118.6	1.06	0.10
DF1-124-11 ~ DF1-124-15	58.1	780.4	117.9	1.38	0.09
DF1-124-16 ~ DF1-125-4	58.2	776.0	100.0	0.94	0.08
DF1-125-4 ~ DF1-125-10	58.4	770.5	110.0	0.96	0.05
DF1-125-11 ~ DF1-125-15	58.5	765.0	112.7	0.89	0.06

---

[1] Nagoya University

[2] Hirosaki University

[3] The University of Tokyo

We confirmed the increase of both [10]Be and [36]Cl concentrations around AD 780. Similar increase of [10]Be and [36]Cl fluxes was reported by F. Mekhaldi et al. [4], who analyzed ice core samples from Greenland. These results indicate that the AD 774/5 event was confirmed in both hemispheres.

In this study, it is of essential importance to compare the [36]Cl-AMS data with the [10]Be-AMS data. Therefore, we have developed [10]Be-AMS by the Tsukuba-AMS system for measurements of [10]Be in the ice core samples. For [10]Be-AMS, [10]BeO$^-$ was extracted from BeO samples mixed with Nb and accelerated to 6.0 MeV. The maximum [9]BeO$^-$ beam current was ~ 7 μA from the ion source. Figure 1 shows 2D spectra for the standard reference material KNBe5-1 ([10]Be/Be = 2.709 × 10^{-11}) [5], measured with a run time of 120 s, and for [10]Be from a blank sample, measured with a run time of 300 s. As a result, we have achieved the [10]Be/Be background level of 3 × 10^{-15} and confirmed the extraction of enough [9]BeO$^-$ beam current from the ion source. At present, we have measured [10]Be concentrations in the rain, meteorite samples and so on.

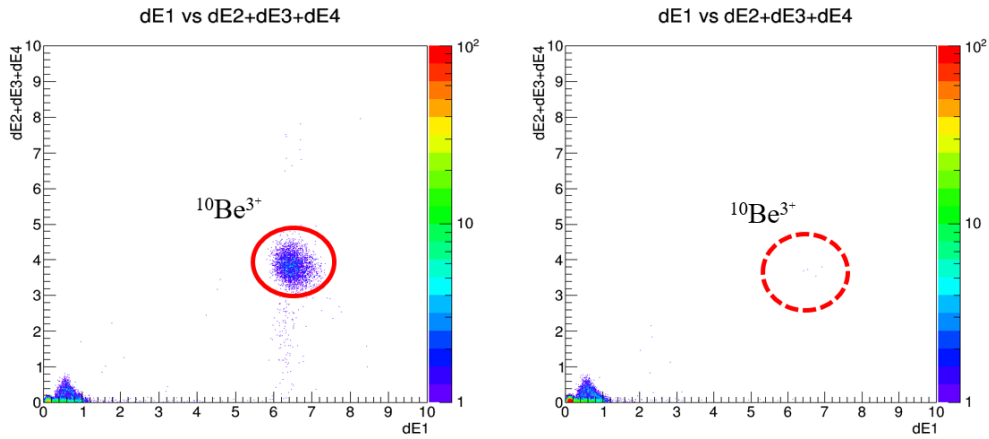Fig. 1. Comparison of measured 2D spectra for a standard reference sample (left) and a blank sample (right).

References

[1] F. Miyake et al., Nature 486 (2012) 240.

[2] F. Miyake et al., Geophys. Res. Lett. 42 (2015) 84.

[3] K. Sasa et al., Nucl. Instr. Meth. Phys. Res. B 437 (2018) 98.

[4] F. Mekhaldi et al., Nature Com. 6 (2015) 8861.

[5] K. Nishiizumi et al., Nucl. Instr. Meth. Phys. Res. B 258 (2007) 403.

3.4 Measurements of cosmogenic ^{10}Be and ^{36}Cl in precipitation during 2015 − 2016

Y. Ochiai, K. Sasa, Y. Tosaki[1], T. Takahashi, M. Matsumura, K. Takano, Y. Ota, K. Sueki

^{10}Be (half-life = 1.36×10^6 years) and ^{36}Cl (half-life = 3.01×10^5 years) are cosmogenic nuclides, which are produced by nuclear reactions between cosmic rays and elements constituting the Earth, e.g., ^{14}N(n, X)^{10}Be or ^{40}Ar(n, X)^{36}Cl. After the production, ^{10}Be and ^{36}Cl are attached to rainwater or aerosols and are deposited on the surface of the Earth. In the present work, ^{10}Be and ^{36}Cl deposition fluxes were measured with monthly rainwater samples. It is found that the ^{36}Cl deposition flux correlates with the ^{10}Be flux, while the ratio of ^{36}Cl to ^{10}Be fluctuates monthly.

We have collected monthly rainwater samples at the University of Tsukuba (36°06'N, 140°06'W) since April 2004. In this study, ^{10}Be and ^{36}Cl deposition fluxes during 2015 − 2016 were analyzed. After adding Be carrier of 0.5 mg, Be^{2+} and Cl$^-$, which exist in the chemical forms of Be and Cl in the rainwater samples, were extracted by the ion exchange method. Be^{2+} was precipitated as Be(OH)$_2$ with 15 M NH$_4$OH and converted to BeO by heating in the electric furnace at 850 °C. Cl$^-$ was precipitated as AgCl with 0.3 M AgNO$_3$ and washed with ultrapure water and ethanol. ^{10}Be and ^{36}Cl were measured with the accelerator mass spectrometry system at UTTAC [1]. The background values are ^{10}Be/Be < 1.0×10^{-15} and ^{36}Cl/Cl < 3×10^{-15}, and the precision for both ^{10}Be and ^{36}Cl analyses is ~2%. The measured values were corrected with KN standards prepared by Nishiizumi [2, 3].

Figure 1 shows (a) the temporal variation of ^{10}Be and ^{36}Cl deposition fluxes and (b) precipitation amount at the sampling site during 2015 − 2016. The ^{36}Cl measurement of the sample in January 2016 was unsuccessful due to serious contamination of sulfur. The ^{10}Be and ^{36}Cl deposition fluxes range from $(1.70 \pm 0.03) \times 10^2$ to $(8.8 \pm 0.6) \times 10^2$ atoms m^{-2} s^{-1} and from 9.2 ± 1.3 to $(1.14 \pm 0.04) \times 10^2$ atoms m^{-2} s^{-1}, respectively. The ^{10}Be deposition flux correlates with ^{36}Cl strongly, corresponding to the
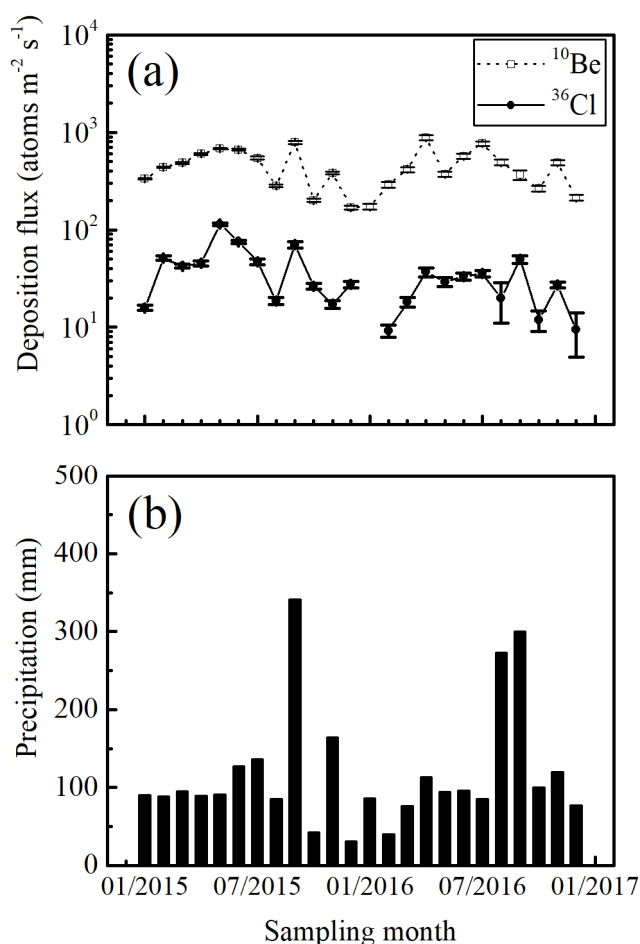
Fig.1 (a) ^{10}Be and ^{36}Cl deposition fluxes and (b) precipitation amount during 2015 − 2016.

correlation number r = 0.7. Although previous studies concluded that ^{10}Be or ^{36}Cl deposition flux correlates with precipitation amount [4, 5], the present work demonstrates that the correlation between precipitation and either ^{10}Be or ^{36}Cl is as weak as r = 0.5 and 0.3, respectively. The strong correlation between ^{10}Be and ^{36}Cl is caused not by precipitation dependence of the deposition flux, but by their similar behavior in the environment.

Figure 2 shows monthly variation of the ratio of ^{36}Cl to ^{10}Be deposition flux during 2015 – 2016. The average of the monthly ratio ^{36}Cl/^{10}Be = 0.079 ± 0.002 is lower than the ratio of ^{36}Cl/^{10}Be = 0.10

Fig. 2. Monthly variation of the ratio of ^{36}Cl to ^{10}Be deposition flux during 2015 – 2016.

± 0.01 which was estimated from the production rates in the whole Earth [6]. This would indicate that ^{10}Be or ^{36}Cl is deposited heterogeneously on the surface of the Earth. Hence, further investigations are needed to understand the mechanism. We now plan to measure rainwater samples in other sites.
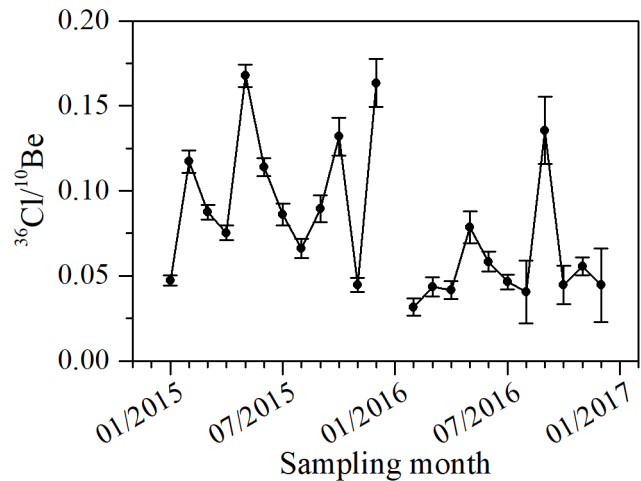
References

[1] K. Sasa et al., Nucl. Instr. Meth. Phys. Res. B 437 (2018) 98.

[2] K. Nishiizumi et al., Nucl. Instr. Meth. Phys. Res. B 258 (2007) 403.

[3] P. Sharma et al., Nucl. Instr. Meth. Phys. Res. B 52 (1990) 410.

[4] I. Graham et al., Geochim. Cosmochim. Ac. 67 (2003) 361.

[5] F. M. Phillips, Chlorine-36 In: Environmental Tracers in Subsurface Hydrology, P. G. Cook and A. L. Herczeg (Eds.), Kluwer Academic (2000) 299.

[6] J. Masarik and J. Beer, J. Geophys. Res. 114 (2009) D11103.

3.5 Depth profiles of organic ^{36}Cl derived from the Fukushima Dai-ichi Nuclear Power Plant

Y. Ota, K. Sueki, T. Takahashi, M. Matsumura, S. Hosoya, K. Takano, Y. Ochiai, T. Matsunaka[1], Y. Satou[2], K. Sasa.

A large amount of radionuclide was released into the environment by the Fukushima Dai-ichi Nuclear Power Plant (FDNPP) accident that has been caused on March 11, 2011 and afterwards. The long-lived radionuclide, ^{36}Cl ($T_{1/2} = 3.01 \times 10^5$ yr) might also be released. However, there were few reports quantifying ^{36}Cl with environmental samples because the analysis of ^{36}Cl requires an AMS system [1]. Therefore, we measured the ratio ^{36}Cl/Cl of chloride in soil water with 31 surface soil samples around the FDNPP, and reported high values of the ratios [2, 3].

In soil, chlorine exists as chloride in soil water (Cl_{inorg}), chlorinated organic matter (Cl_{org}), and chloride in minerals ($Cl_{mineral}$). In the past, chlorine was believed to be present in soil only as Cl_{inorg}. However, recent studies have shown that Cl_{inorg} is easily converted to Cl_{org} by biotic and abiotic processes [4, 5]. Thus, ^{36}Cl released from the FDNPP accident was probably deposited as Cl_{inorg} and later converted partly to Cl_{org}. Therefore, we also have to measure ^{36}Cl/Cl of Cl_{org} in order to investigate whether ^{36}Cl released from the FDNPP accident remains as Cl_{org}.

We used 30-cm-long soil cores at Namie-machi, Fukushima (37° 33′ 39″E, 140° 49′ 41″N) on June 12, 2013, June 17, 2016 and September 10, 2017, whose ^{36}Cl/Cl ratios of Cl_{inorg} have already been measured [3]. After acid extraction of Cl_{inorg} [3], the soil was vacuum-freeze-dried and grinded using a mortar and pestle.

Separation procedure of Cl_{org} from the soil was developed by referring to the method for ^{129}I analysis in soil by AMS [6]. In this procedure, the soil is combusted and Cl_{org} is decomposed into HCl or Cl_2. These volatile chlorines are collected as chloride ions with absorbent solution containing H_2O_2. The combustion apparatus is shown in Fig.1. The soil sample of about 2 g in a ceramic boat was combusted by tubular furnace at 550°C under a flow of O_2 gas. The ceramic boat was inserted slowly to the tubular furnace taking 10 minutes and combusted at the middle point for 15 minutes. The volatilized chlorine was collected with 120 mL of trap solution containing 0.5% H_2O_2, 2.7 mM Na_2CO_3 and 0.3 mM $NaHCO_3$. Then, 30% H_2O_2 of 5 mL was added to the absorbent solution and it was left overnight. We have to remember that the volatile chlorine cannot be trapped in absorbent solution by incomplete combustion. In this case, Cl_{org} is not decomposed. Therefore, we combusted a little soil with O_2 gas flow of over 1000 mL/min.
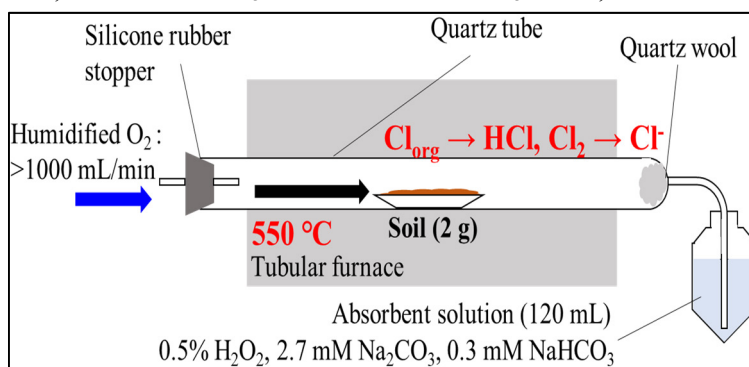
Fig.1. The combustion apparatus of soil for Cl_{org} separation.

[1] Kanazawa University
[2] Japan Atomic Energy Agency (JAEA)

It is notable that we used the low temperature (550 °C) combustion of soil in order to separate Cl_{org} from $Cl_{mineral}$ that is originated not from the FDNPP accident.

From the absorbent solution, 5 ml aliquot was taken for analysis of stable chlorine by ion chromatography. Then, appropriate amount of chlorine carrier $^{36}Cl/Cl \approx (5 - 8) \times 10^{-15}$ was added to the absorbent solution. Lastly, the sample solution was purified by the procedure described previously in order to remove ^{36}S that interferes ^{36}Cl-AMS, and then chlorine was precipitated as AgCl [2]. The $^{36}Cl/Cl$ ratio was measured by the AMS system at UTTAC. The terminal voltage was 6.0 MV and the detected ion was $^{36}Cl^{8+}$. The measured ratios were normalized using the ^{36}Cl standard ($^{36}Cl/Cl = 5.00 \times 10^{-13}$) developed by Sharma et al. [7].

Figure 2 shows the depth profiles of Cl_{org} concentration, $^{36}Cl/Cl$, and $^{36}Cl_{org}$ concentration in 2013, 2016, and 2017. The high ratios of $^{36}Cl/Cl$ are observed for Cl_{org} as well as for Cl_{inorg} [3]. However, the depth profiles of $^{36}Cl/Cl$ for Cl_{org} seem to have broad peaks, while those of $^{36}Cl/Cl$ for Cl_{inorg} are monotonically decreasing [3]. We may therefore assume that the fast isotope exchange of Cl_{inorg} started right after the FDNPP accident and, in parallel, Cl_{inorg} was converted to Cl_{org}. In consequence, the $^{36}Cl/Cl$ ratios for Cl_{org} are those before fast isotope exchange of Cl_{inorg} has ended.
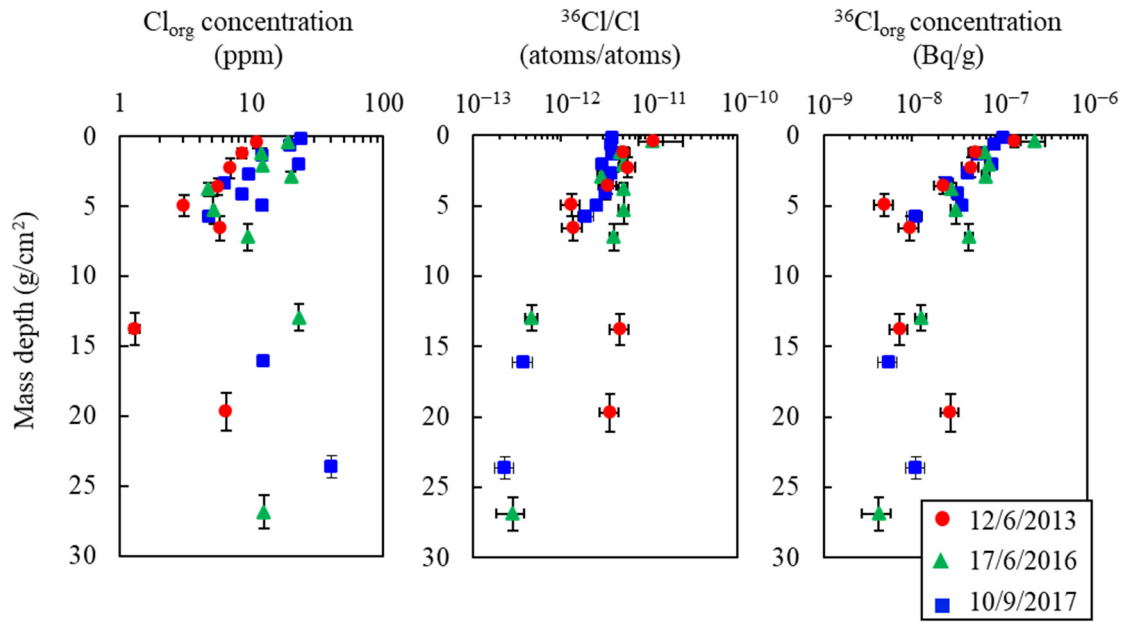
Fig.2. Depth profiles of Cl_{org} concentration, $^{36}Cl/Cl$, and $^{36}Cl_{org}$ concentration in soil at Namie-machi, Fukushima (37° 33′ 39″E, 140° 49′ 41″N) on June 12, 2013, June 17, 2016, and September 10, 2017.

References

[1] Y. Miyake et al., Nucl. Instr. Meth. Phys. Res. B 361 (2015) 627.

[2] Y. Ohta et al., UTTAC Annual Report 2016 (2017) 20.

[3] Y. Ota et al., UTTAC Annual Report 2017 (2018) 19.

[4] G. Öberg et al., Applied Microbiology and Biotechnology (2002) 565.

[5] D. Bastviken et al., Geochimica et Cosmochimica Acta (2007) 3182.

[6] Y. Muramatsu et al., Quaternary Geochronology (2008) 291.

[7] P. Sharma et al., Nucl. Instr. Meth. Phys. Res. B 52 (1990) 410.

3.6 Distribution of ^{129}I inventory in difficult-to-return zones in Fukushima Prefecture

H. Yokoyama, K. Sueki, K. Sasa, T. Matsunaka[1], T. Takahashi, M. Matsumura, K. Takano, Y. Ochiai, R. Hasegawa, Y. Ota

Due to the Fukushima Dai-ichi Nuclear Power Plant (FDNPP) accident in March 2011, large amount of radionuclide was released from FDNPP. In particular, the total amount of ^{131}I (half-life: 8.01 d), ^{134}Cs (half-life: 2.06 y) and ^{137}Cs (half-life: 30.1 y) released into the atmosphere was estimated to be approximately 16, 1.8, and 1.5 PBq, respectively [1]. ^{131}I is one of the harmful radionuclides released from FDNPP because of causing thyroid cancer in children, and therefore, it is urgent to elucidate environmental dynamics of ^{131}I. However, it is difficult to do this by direct measurements of ^{131}I owing to its short life. Instead, reproduction of distribution of ^{131}I inventory employing long-lived ^{129}I (half-life: 1.57×10^{7} y) has been now under way, and as one of the approaches, the weighted average of ^{131}I/^{129}I ratio at Fukushima on March 11, 2011 was determined to be $(4.02 \pm 0.81) \times 10^{-2}$ [2]. On the other hand, ^{134}Cs and ^{137}Cs remain a lot in the soil several years after the FDNPP accident and possibly influence human health, so that we must grasp the distribution of ^{134}Cs and ^{137}Cs inventory. Currently, the regional distributions of deposited ^{131}I and ^{129}I have been reported [2-4], but the deposition near FDNPP has little been reported. Thus, we observed the deposition amounts of ^{129}I, ^{134}Cs, and ^{137}Cs in the surface soils of the vicinity of FDNPP and discussed the relation between radioactive iodine and cesium released from FDNPP.

In this study, 44 soil samples were collected at Namie, Futaba, and Okuma, in Fukushima Prefecture. After they were homogenized, ^{134}Cs and ^{137}Cs activities were measured with a Ge gamma-ray detector (IGC25190, Princeton Gamma Tech). For the homogenized soil of 0.5 g, iodine was extracted by pyrohydrolysis with 0.5 g V_2O_5 [5]. Iodine thus obtained was purified by solvent extraction and then it was precipitated as AgI. The isotope ratio ^{129}I/^{127}I was measured by accelerator mass spectrometry (AMS). In addition, ^{127}I concentration in the trap solvent obtained by pyrohydrolysis was measured with the inductively coupled plasma-mass spectrometer (ICP-MS, Agilent 8800).

As a result, the deposition amounts of ^{129}I, ^{134}Cs, and ^{137}Cs in the surface soil on March 11, 2011 are estimated to be $0.0385 - 5.11$ Bq m^{-2}, $0.0663 - 37.1$ MBq m^{-2}, and $0.0668 - 38.1$ MBq m^{-2}, respectively. The radioactivity ratio of ^{129}I/^{137}Cs is $(0.0603 - 4.83)\times 10^{-6}$. Distributions of ^{129}I inventory and radioactivity ratio of ^{129}I/^{137}Cs are shown in Fig. 1. A positive correlation between ^{129}I and ^{137}Cs radioactivity concentrations is recognized, especially in the area where the radioactive plumes passed through. For example, in the area more than 13 km northwest of FDNPP, the correlation coefficient between ^{129}I and ^{137}Cs is 0.92 and the ratio of ^{129}I/^{137}Cs is $(2.3 \pm 0.2) \times 10^{-7}$. In the north-northwest of FDNPP, the correlation coefficient is 0.98 and the ratio of ^{129}I/^{137}Cs is $(2.7 \pm 0.2) \times 10^{-7}$. These ratios agree well with the calculated values of $\sim 3 \times 10^{-7}$ using ORIGEN 2.2 code [6].

---

[1] Kanazawa University
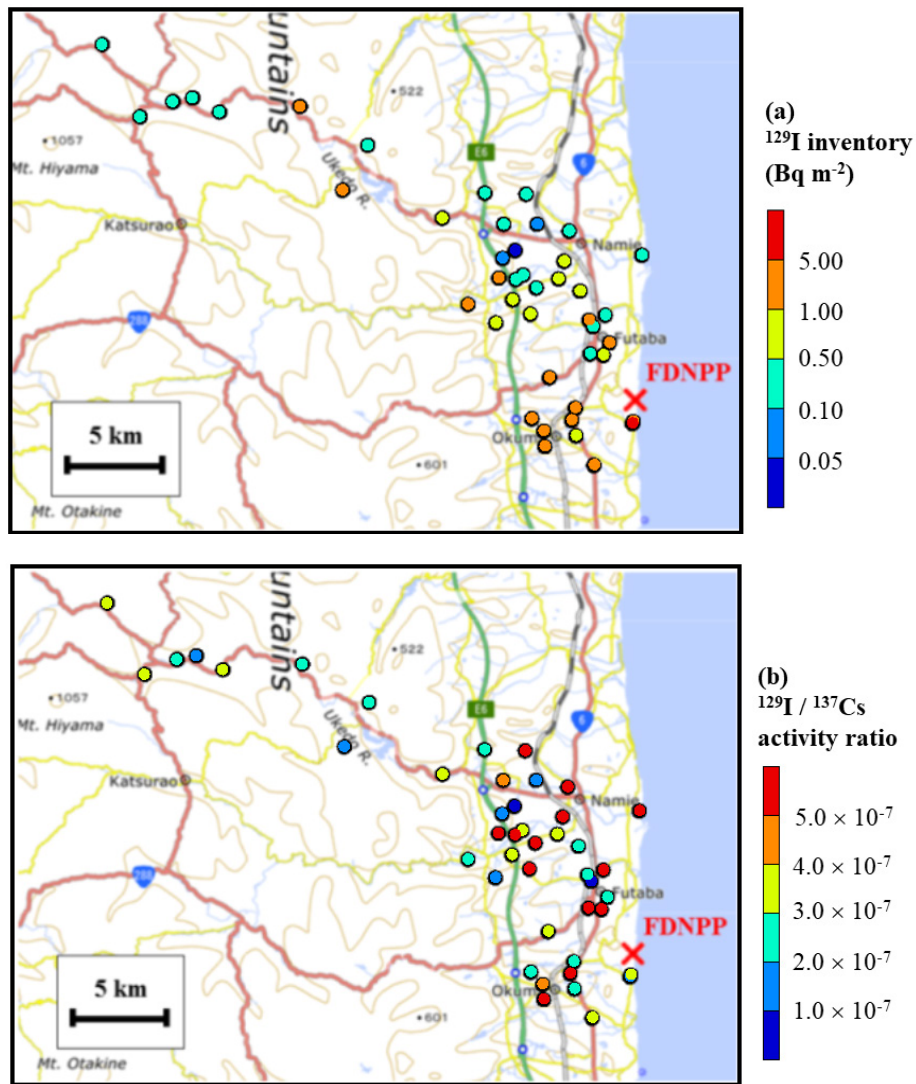
Fig.1. (a) Distributions of ^{129}I inventory and (b) radioactivity ratio of ^{129}I/^{137}Cs.
The base maps of these figures were made by Geographical Survey Institution
in Japan.

References

[1] METI (Ministry of Economy, Trade and Industry in Japan), Revised Total Release of Radionuclides (in Japanese), 2011.   http://warp.da.ndl.go.jp/info:ndljp/pid/3487098/www.meti.go.jp/press/2011/10/20111020001/20111020001.pdf

[2] K. Sasa et al., UTTAC annual report 2013, p. 35

[3] Y. Miyake et al., Geochemical Journal, 46 (2012) 327.

[4] Y. Muramatsu et al., Journal of Environmental Radioactivity, 139 (2015) 344.

[5] Y. Muramatsu et al., Quaternary Geochronology, 3 (2008) 291.

[6] K. Nishihara et al., JAEA-Data/Code 012-018 (2012) (in Japanese).

3.7 Anthropogenic iodine-129 in the Japan Sea and Okhotsk Sea during 2017−2018

T. Matsunaka[1], S. Nagao[1], M. Inoue[1], S. Ochiai[1], T. Morita[2], S. Miki[2], N. Honda[2], T. Aramaki[3], I. Kudo[4], T. Takikawa[5], K. Sueki, T. Takahashi, K. Sasa

Long-term oceanographic observation revealed that warming and oxygen decrease of the Japan Sea Bottom Water (JSBW) are responding to air temperature raise in winter [1]. Investigation of water dynamics in the Japan Sea using a radioactive tracer is essential for elucidating the interaction between climate change and the convection system. Recent progress in our research program using the ^{129}I tracer is reported.

Anthropogenic ^{129}I ($T_{1/2}$ = 15.7 million years) produced from the thermal neutron fission is released dominantly from nuclear fuel reprocessing plants in Europe. To investigate the availability of ^{129}I as a tracer of surface circulation and vertical convection in the Japan Sea, AMS at UTTAC was used to measure the horizontal and vertical distributions of ^{129}I in the large area of the sea in 2017–2018. The radioactivity of ^{129}I dissolved in surface water in the East China Sea and the Japan Sea varied from 15.1±0.7 to 25.1±0.8 nBq L^{-1}, and was negatively correlated with salinity (R^2 = 0.94, n = 18), see Fig. 1.

The salinity dependence of the distribution has revealed that ^{129}I dissolved in the area is controlled by mixing of water mass from the Liman Current and the Tsushima Current. Meanwhile, ^{129}I dissolved in the JSBW observed in the layer of 2450–3500 m of the Japan Basin in 2017 and 2018 were 4.2±0.6 nBq L^{-1} and 4.2±0.5 nBq L^{-1}, shown respectively in Fig. 2, which increased by 1.2 nBq L^{-1} from that in 2007 [2]. Further studies using the ^{129}I tracer is now under way.
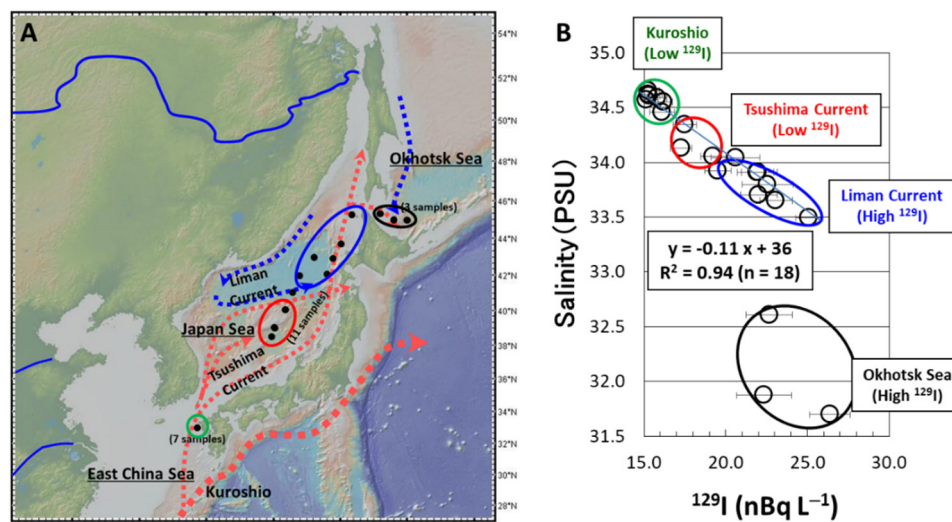
Fig. 1. Sampling sites of surface seawater in the East China Sea, Japan Sea, and Okhotsk Sea (A). The correlations between ^{129}I activities in seawater and salinity (B). The linear regression lines and coefficients of determination (R^2) are shown in the correlation diagram.
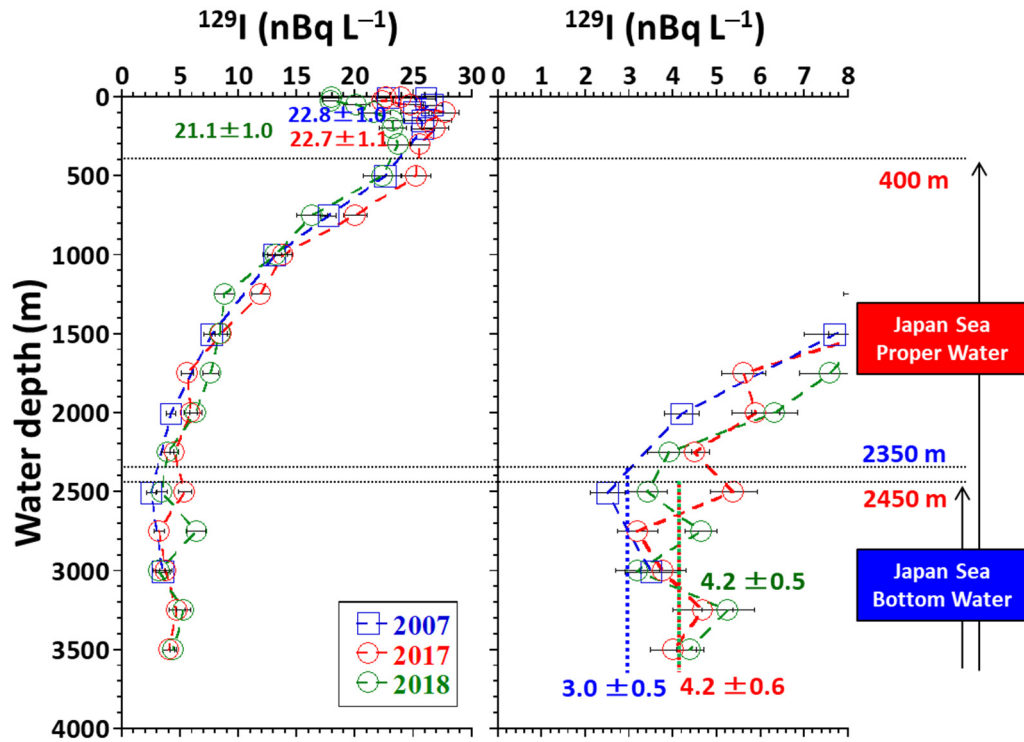
Fig. 2. Vertical distributions of ^{129}I in the Japan Basin observed in 2007 [2], 2017, and 2018. The boundaries of the proper water and bottom water are also shown.

References

[1] T. Gamo, Trends Anal. Chem. 30 (2011) 1308

[2] T. Suzuki et al., Nucl. Instr. Meth. Phys. Res. B 268 (2010) 1229

3.8 Performance of Iodine-129 AMS measurements at the University of Tsukuba

M. Matsumura, K. Sasa, T. Takahashi, K. Takano, Y. Ochiai, H. Yokoyama, T. Matsunaka[1], K. Sueki

Improvement of accelerator mass spectrometry (AMS) at the University of Tsukuba has been continued since its setup in 2015. This report focuses on the development of the standard reference materials (STD) in the near future for ^{129}I-AMS. Details of the ^{129}I measurement conditions with the 6MV tandem accelerator were described in the references [1, 2].

We measured 294 samples of ^{129}I from April 2018 to March 2019, as shown in Fig. 1. The test samples were chosen from environmental materials such as soil, rain water, sea water and coral. The ^{129}I/^{127}I ratio of sea water and coral samples are extremely low, on the order of 10^{-13}. Thus it is important to keep a low background level in ^{129}I-AMS. Figure 2 shows the measured background values using blank samples for
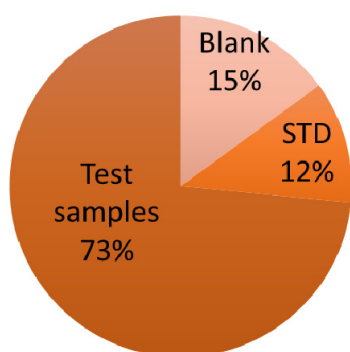
Fig. 1. ^{129}I samples measured by the AMS system in fiscal 2018.
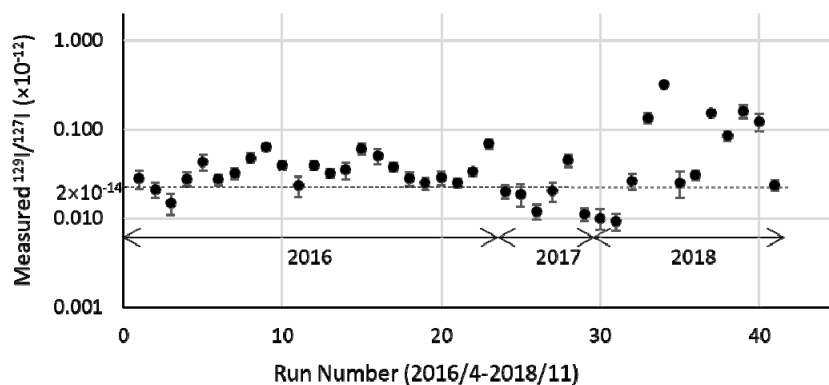
Fig. 2. ^{129}I/^{127}I ratios for blank samples.

the past 3 years. "Old Iodine" provided from Deepwater corporation has the extremely low background, as low as ^{129}I/^{127}I ~2×10^{-14}, while the machine background is estimated to be lower, i.e., ^{129}I/^{127}I~10^{-15}. However, sometimes, the measured values of ^{129}I/^{127}I for blank samples are ten times higher than for the Old Iodine. This might be mainly attributed to the memory effect, discussed previously [3].

We performed Cs irradiation to the cathode filled with Nb powder only, considering that the same Nb powder was used for the cathode disk which results in the high ^{129}I/^{127}I ratio of 10^{-11}~10^{-10}. After measuring these samples of high ^{129}I/^{127}I ratios, we measured the Nb-filling sample. As shown in Figs. 3 and 4, there certainly exists the memory effect. The detector system appears to have a memory of ^{129}I^{5+}, since the ^{129}I^{5+} counts from the Nb-filling sample decreases with increasing the irradiation time. Even 100 minutes later, approximately 5, rather than 0, counts were detected, so that it seems difficult to completely remove the memory effect. The enhanced background level obtained from blank samples in 2018 is likely to be caused by this memory effect. Therefore, low-level samples must be carefully measured, i.e., not in the same series of analysis including other samples of greatly different isotope ratios.

---

[1] Kanazawa University
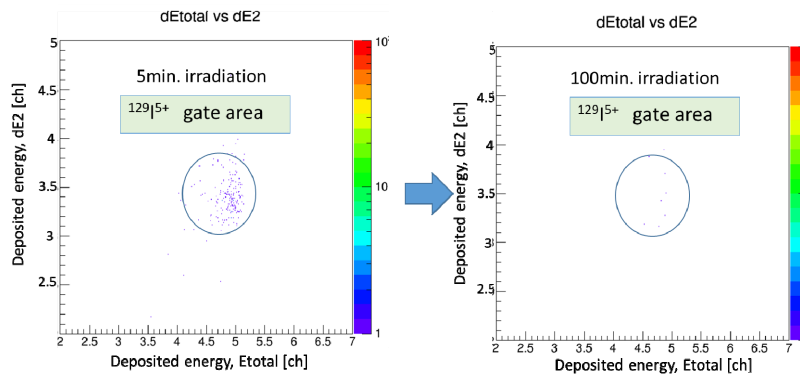
Fig. 3. The ^{129}I spectra from the Nb-filling sample.
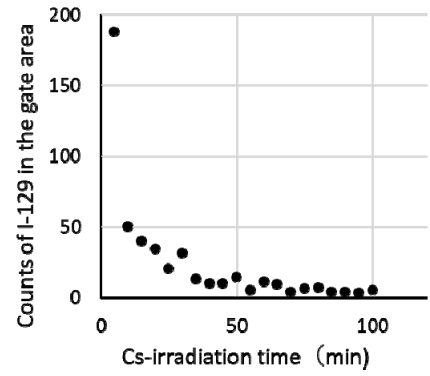
Fig. 4. Time variation of ^{129}I counts.

References

[1] K. Sasa et al., Nucl. Instr. Meth. Phys. Res. B 437 (2018) 98.

[2] M. Matsumura et al., UTTAC Annual Report 2016 (2017) 25.

[3] M. Matsumura et al., Proceedings of the 21th Symposium on The Japanese Society of Accelerator Mass Spectrometry Research (2018), in press.

4.

BEAM AND ISOTOPE APPLICATIONS

4.1 Free volumes introduced by fractures of CFRP probed using positron annihilation

A. Uedono, K Sako, W. Ueno, M. Kimura[1]

A void formation at nanoscale and a crack initiation at micrometer scale in CFRP during a tensile test were investigated by means of positron annihilation and X-ray computed tomography (X-CT). Free volumes in bisphenol-A epoxy resin in CFRP were probed, and a mean diameter of free volumes at room temperature was determined to be 0.49 nm. The crack initiation and propagation in the CFRP sample were observed by in-situ measurements of X-CT during a tensile test. For the sample after the tensile test, free volumes with a mean diameter of 0.70 nm were introduced near fractures locations. In the same locations, the density of free volumes which intrinsically existed in the polymer resins decreased. Thus, the introduction of the free volumes was attributed to breaks in molecular chains upon fracture and a resultant agglomeration of intrinsic free volumes in the polymer matrix.
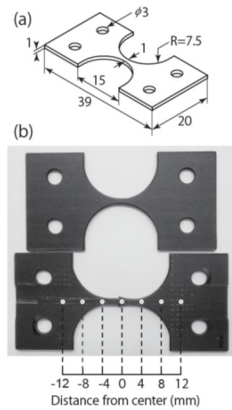
Fig.1. (a) illustration of CFRP sample, and (b) pictures of sample before (above) and after tensile test (below). Positions of lifetime measurements are shown as white open circles on the sample after the tensile test.

Fig.2. Stress and strain curve for CFRP sample. Measurements were interrupted three times for X-CT measurements (denoted as b, c, and d). Fracture of sample occurred at $\varepsilon = 7.6\%$.

Fig.3. Reconstructed 3D images near center of sample at ε = (a) 0%, (b) 1.0%, (c) 2.1%, (d) 3.1%, and (e) 7.6%, which were obtained by *in-situ* X-CT measurements. Positions of delamination and/or cracks are denoted as 1, 2, 3, and 4.
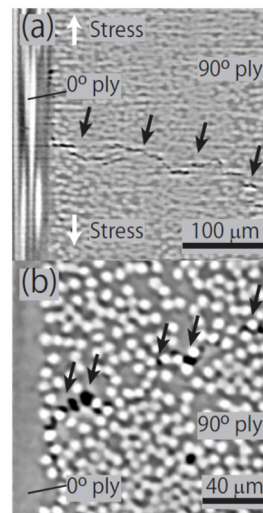
Fig. 4. Cross section of reconstructed images near center of sample with $\varepsilon = 3.1\%$ (a) and its magnified image (b). White arrows show the direction and stress and black arrows show transverse crack and voids near the carbon fibers, respectively.

[1]Institute of Materials Structure Science, KEK
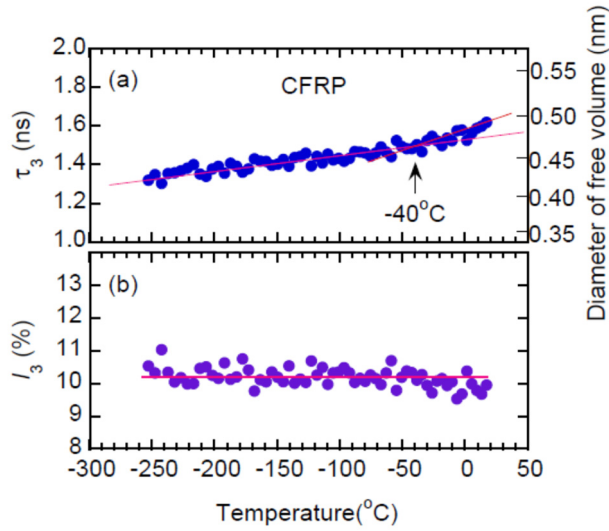
Fig.5. Temperature dependence of third lifetime (a) and corresponding intensity (b) for CFRP sample before tensile test. Diameter of free volumes corresponding to τ_3 is shown on right axis. Temperature gradient of τ_3 increased at −40°C.
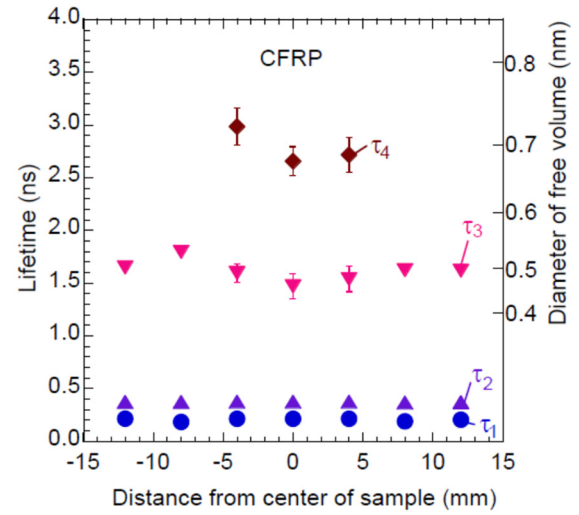
Fig.6. Positron lifetimes for CFRP sample after tensile test. Positions of measurements (horizontal axes) are shown in Fig. 1(b). First and second components were associated with the annihilation of positrons in both carbon fibers and polymer matrix. Third and fourth components were attributed to the pick-off annihilation of o-Ps in polymer matrix.
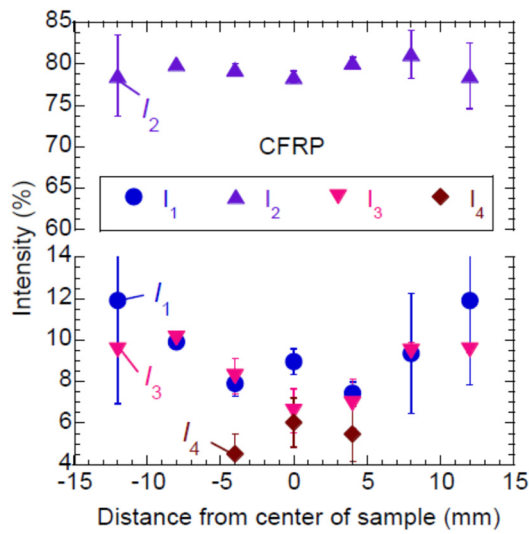
Fig.7. Relative intensities for CFRP sample after tensile test.
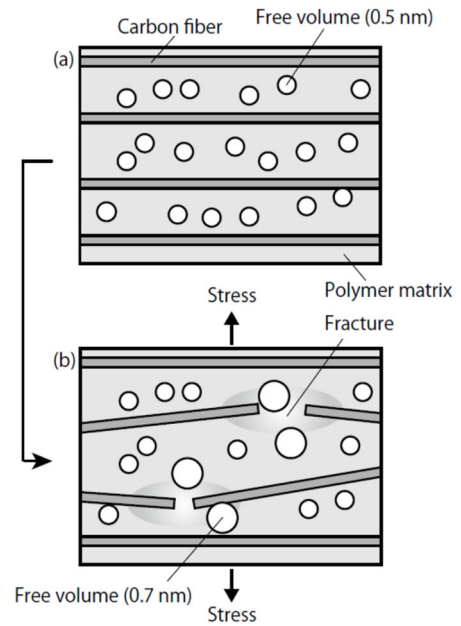
Fig.8. Schematic of free volumes and fractures in CFRP (a) before and (b) after tensile test.

Reference

[1] A. Uedono et al., Composites Part A 122 (2019) 54.

4.2 Preliminary micro-PIXE analysis of silicate glass particles released from Fukushima nuclear plant

M. Kurosawa, K. Sueki, K. Sasa, S. Ishii, M. Matsumura, K. Matsuo, T. Ishii

Radioactive silicate microparticles emitted from the Fukushima Daiichi nuclear power plant (FDNPP) have recently attracted attention as a transportation process of radioactive cesium to the natural environment [1–6]. Ono et al. [5] and Satou et al. [6] discovered a new type of radioactive silicate-glass particles with cesium in a soil sample collected at the northwestern region of the FDNPP. These radioactive particles are emitted certainly from reactor 1 of the FDNPP [5, 6]. Thus, chemical characterization of such glass particles is important to understand the formation processes and the situation inside the reactor 1 at the nuclear accident. For these reasons, we analyzed major to trace elements in the radioactive silicate glass particles by using micro PIXE to examine the chemical compositions. Glass-particle samples were collected by Ono et al. [5] and Satou et al. [6]. The two samples (T43 and T23) analyzed were a few hundred micrometer-sized and irregular-shaped aggregates of fused glass and glass particles with tiny solid inclusions and bubbles. The sample surfaces were polished and were coated with a carbon film to prevent electrostatic charging. Before the micro-PIXE analyses, major compositions of the samples were analyzed with a scanning electron microscope equipped with an energy-dispersive X-ray spectrometer (SEM–EDS) to determine the stopping power and X-ray attenuation factors of the samples. Major compositions of glass matrices in the two glass samples are quite homogeneous, but small

areas including tiny inclusions consist of high concentration of FeO or ZnO, TiO_2, BaO, and PbO. The glass matrices agreed in chemical composition with a typical soda-lime glasses (Table 1). Taking into account many bubbles in the glass matrices, the glass-particle samples could be emitted at high temperature conditions above melting points of soda-lime glasses (Table 1) from the FDNPP. Densities of the glass matrices were estimated by using the equation of Huggins and Sun [9].

PIXE analyses were performed at the 1MV Tandetron. A 0.1 nA beam of 1.92-MeV proton was focused to a 26.4×19.8 μm spot on the sample using slits and magnetic lenses. The beam was incident normal to the sample surface, and the X-ray measurement take-off angle was 45° [10]. The characteristic X-rays excited by the incident beam were collected by the Si(Li)

Table 1. Major chemical compositions of soda-lime glasses and glass matrices of T23 and T43.

wt.%	Soda-lime glasses			T23 and T43 glass matrices*[1]	
	Float glass[7]	Container glass[7]	Sample [8]	Average	std (1s)
Na_2O	13.50	13.10	13.40	10.26	(0.97)
MgO	3.80	0.10	1.70	3.20	(0.21)
Al_2O_3	1.80	1.80	1.20	3.93	(0.19)
SiO_2	72.60	72.50	72.50	74.21	(0.73)
SO_3	0.20	0.18	0.30	0.42	(0.19)
K_2O	0.00	0.80	0.40	0.43	(0.08)
CaO	7.90	11.20	10.60	7.02	(0.36)
TiO_2	0.00	0.00	0.00	0.39	(0.17)
MnO	0.00	0.00	0.00	0.02	(0.03)
FeO	0.10	0.03	0.00	0.09	(0.06)
Total	99.90	99.71	100.10	99.97	
Density*[2]	−	−	2.507	2.50	
Melting(°C) *[3]	−	1063	−	−	

*[1]Average chemical composition of T23 and T43 glasses determined by SEM－EDS and the standard deviations. *[2]Density(g/cm³) of soda-lime glass [8] was a measured value and those of T23 and T43 glasses were calculated by using the equation of Huggins and Sun [9] and the averaged chemical composition. *[3]Melting temperature [7].

X-ray-energy detector with a nominal resolution of 140 eV at 5.9 keV. We used a 55-μm-thick Mylar filter to prevent the scattered protons from entering the detector. The total charge was determined by integrating the target current, and all the samples were analyzed for the total charges of 0.31 μC to 0.33 μC. Analytical points were chosen based on optical viewing using a CCD camera mounted on the microscope. Quantification of the PIXE analyses was performed based on the model of Kurosawa et al. [10].

PIXE spectra of the glass samples, shown in Fig. 1, consist mainly of intense K X-ray peaks from Si, Ca, Ti, Fe, and Zn. The spectra also show K X-ray peaks from trace amounts of S, Cl, K, Cr, Mn, Sr, and Zr, and L X-ray peaks from Pb and Ba. X-ray intensities of Ti, Fe, Zn, Ba, and Pb depend on the measurement points, indicating a presence of tiny solid inclusions containing these elements. L X-ray peaks from trace Cs are not identified because of the overlapping with the intense Ti Kα peaks. Element concentrations of the two glasses, determined by PIXE, are as follows: 22.97–30.35 wt.% for Si, 6.10–6.76 wt.% for Ca, 0.27–6.40 wt.% for Ti, 0.34–0.47 wt.% for K, 0.06–0.74 wt.% for Zn, 0.14–0.23 wt.% for S, 0.00–0.23 wt.% for Ba, 0.02–0.13 wt.% for Cl and Pb, 0.00–0.03 wt.% for Cr, Mn, Cu, Sr, and Zr. These contents of the major elements agree with the SEM–EDS results (Table 1). Highly volatile elements such as Cl and S remain homogeneously in the glass samples. The presence of the volatile elements indicates a short-time heating at high-temperature conditions during the formation process of the glass particles. The glass particles can be quenched materials of fused soda-lime glass with the minor components melted by a flash heating (<1000 °C). Melting experiments of the glass particles may be useful to decode the thermal history. In addition, PIXE measurements of K X-ray peaks from Cs by using a 4-MeV proton beam would be suitable for detection of Cs in Ti-rich glass materials.
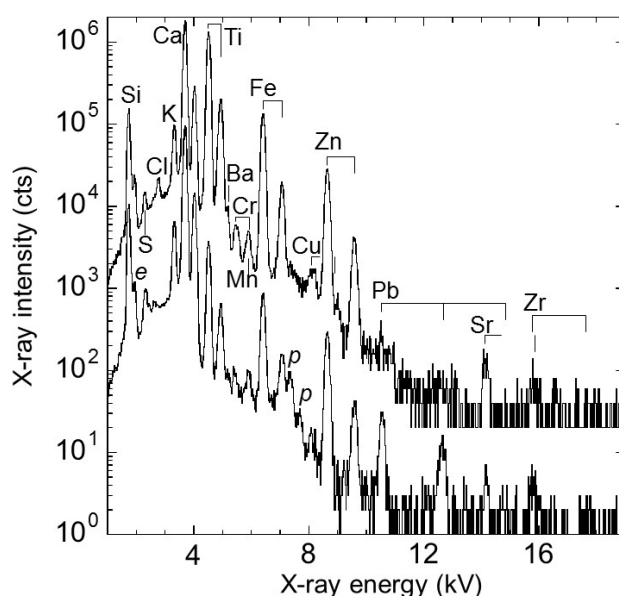
Fig.1. PIXE spectra of silicate glass particles emitted from the FDNPP [5, 6]. Upper spectrum: T23. Lower spectrum: T47. Escape and pile-up peaks are identified as follows: e (escape peak of Ca Kα), p (pile-up peaks of Ca Kα+Ca Kα and Ca Kα+Ca Kβ).

References

[1] K. Adachi et al., Sci. Rep. 3 (2013) 2554.

[2] Y. Abe et al., Anal. Chem. 86 (2014) 8521.

[3] N. Yamaguchi et al., Sci. Rep. 6 (2016) 20548.

[4] T. Kogure et al., Microscopy 65 (2016) 451.

[5] T. Ono et al., Bunseki Kagaku 66 (2017) 251.

[6] Y. Satou et al., Geochem. J., 52 (2018) 137.

[7] Glass Technology Handbook, eds. M. Yamane et al., Asakura shoten, Tokyo, 1999.

[8] P. Bingham, Glass Technol. 45 (2004) 255.

[9] M. Huggins and K. Sun, J. Amer. Ceramic. Soc. 26 (1943) 4.

[10] M. Kurosawa et al., Nucl. Instr. Meth. Phys. Res. B 266 (2008) 3633.

4.3 Kinetic energy measurements of 10−100 keV ions using superconducting tunnel junction

S. Tomita, S. Shiki[1], G. Fujii[1], M. Ukibe[1]

Superconducting tunnel junction (STJ) has a structure of a thin insulator film sandwiched by two superconducting films. The phonons excited by an impinging particle break Cooper pairs in the superconductor, and generate quasiparticles. By applying potential difference between the two superconductors, the quasiparticles tunnel through the insulator. The total amount of the tunneling current is approximately proportional to the amount of generated quasiparticles, i.e. the amount of deposited energy on the superconducting film. Therefore, STJ can be used as an energy sensitive detector. The amount of energy required to break a Cooper pair is on the order of ~meV, thus STJ can be used to measure kinetic energy of keV particles to which the conventional semiconductor detector cannot be applied.

The STJ detector has been successfully used to measure X-rays and ions of keV energies [1]. In particular, the application of the detector in combination with mass spectrometer enables us the separate measurement of ion mass m and ion charge q, while the conventional mass spectrometers can measure only m/q of ions [2]. The application of this technique to detect biomolecule ions could be quite useful to distinguish oligomers having the same m/q values. The protein molecules could have charge states of 10+ to 20+ when an electrospray ion source is used. These ions have kinetic energies of several tens keV. On the other hand, it is known that in the high energy range the pulse height of STJ signal deviates from the proportional response. The mechanism for the deviation is not understood yet, therefore we plan to investigate the STJ response of 10−100 keV carbon ion.

Experiments were performed with the 100-kV ion injector with a cesium sputtering ion source. The negatively charged carbon ions were accelerated and injected into the STJ detector after mass selection with a dipole magnet. The detectors have a structure of Nb/Al/AlO$_x$/Al/Nb, and mounted on a cryostat with the base temperature of about 290 mK. The size of the detector is 100×100 μm^2, and the magnetic field of 100 gauss was applied to eliminate tunneling current due to the Josephson effect. The pulse height distribution of the STJ signal is shown in Fig. 1 for the injection of 15 keV carbon ions. The peak shape has a long tail on the low energy side. This might be due to the escape of particles such as secondary electrons or sputtered particles, and backscattering of injected ion itself, as well. In Fig. 2, the mean value of the pulse heights of signals from the STJ detector is shown as a function of the kinetic energy of impinged ion. For the high energy particles, the deviation from proportional response is observed. We plan to perform a series of measurements of various ions with different energies to understand the mechanism of the deviation for detection of high energy particles.

---

[1] National Institute of Advanced Industrial Science and Technology (AIST)
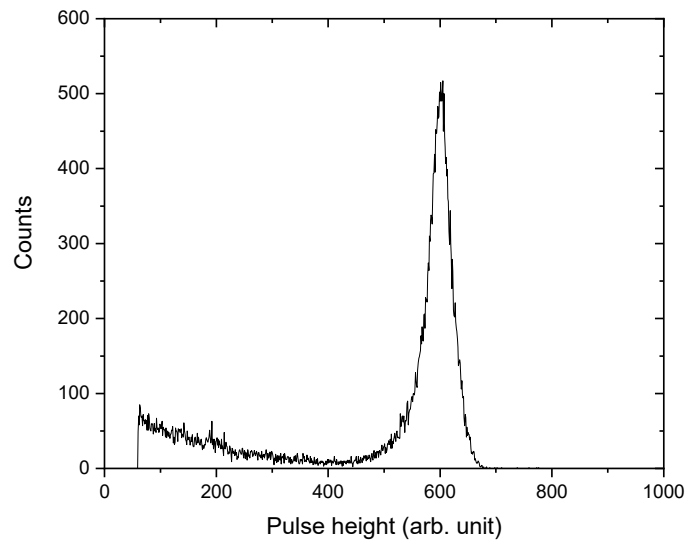
Fig. 1. Pulse height distribution of STJ signal for the detection of 15 keV carbon ions.
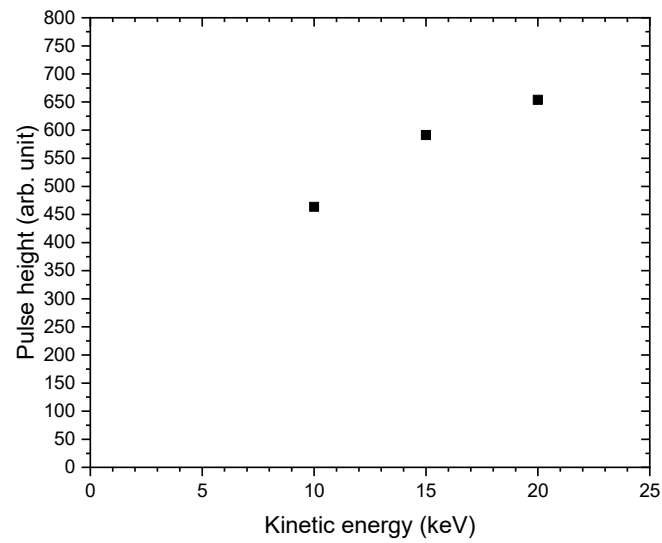
Fig. 2. Mean value of the pulse heights of signals from superconducting tunnel junction detector as a function of the kinetic energy of impinged carbon ions.

References

[1] M. Ohkubo et al., IEEE Transactions on Applied Superconductivity 24 (2014) 1.

[2] S. Shiki et al., Journal of Mass Spectrometry 43 (2008) 1686.

4.4　3D imaging of hydrogen distribution in H-charged Al

A. Yamazaki, S. Ishii, K. Sasa, S. Tomita, H. Naramoto, M. Sataka, H. Kudo

Analysis of hydrogen in materials, particularly acquisition of three-dimensional distribution of hydrogen has been a challenging issue since hydrogen contained as an impurity in the material affects the mechanical properties of the material even if the amount is small. Mainly based on the results of previous research on the formation of focused ion beams, we developed a method to acquire the three-dimensional distribution of hydrogen using elastic recoil detection analysis (ERDA).

In transmission ERDA, a probe ion beam is incident perpendicularly on a thin film sample and the recoil hydrogen is detected on the back side of the sample. By scanning the sample with a well-focused beam, hydrogen mapping with high position resolution can be achieved. Since the energy of recoil hydrogen depends on the depth from the surface of the sample, where hydrogen experiences a head-on collision with the ion, the hydrogen distribution as a function of depth can be deduced. Accordingly we may obtain the three-dimensional distribution of hydrogen in the material.

Figure 1 is a schematic diagram of the transmission ERDA method. The Al sample contains hydrogen which was incorporated by plasma-charging. The thickness of the sample was adjusted to 130 μm so that the incident He can be stopped within the sample, while the recoil hydrogen can pass through the sample. For effective detection of recoil hydrogen, 8-10 MeV He is advantageous because of the large recoil cross section due to the nuclear elastic collision. The sample was scanned with an 8-MeV He beam focused to a few-μm diameter, while measuring the energy spectrum of recoil hydrogen passed through the sample.
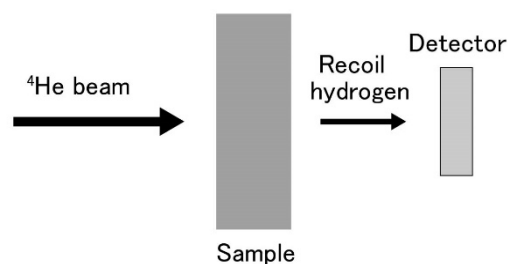
Fig. 1. Schematic diagram of the transmission ERDA.

Figure 2 shows the analysis result. The analyzed area on the Al sample is 500 μm × 500 μm, where the hydrogen signals are shown in yellow for the three sliced depths of 5 μm width. These maps indicate that hydrogen aggregates and changes probably to H_2 bubbles. Moreover, brightness of each yellow spot varies with increasing the depth, reflecting the 3D shape of the aggregates.

It is notable that the member of the UTTAC micro-beam group has filed a patent application as a hydrogen three-dimensional imaging method that can be obtained with "micrometer position resolution" and "low beam dose", combining the ion beam focusing technology with these research results.

Depth: 0–5 μm　　　5–10 μm　　　10–15 μm
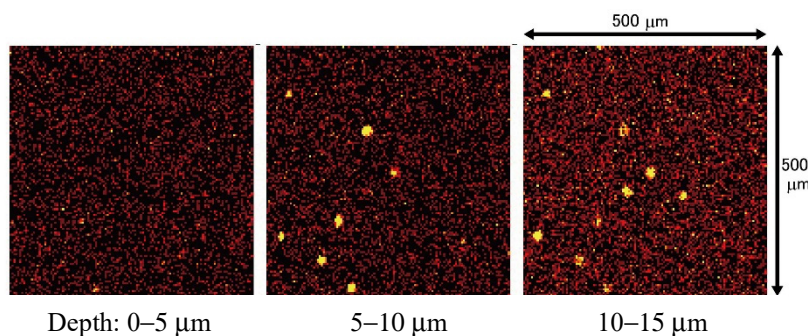
Fig. 2. Distribution of plasma-charged hydrogen in Al.

4.5   Reflection ERDA of hydrogen isotopes in DLC/Si using 15 MeV ^{16}O ions

H. Naramoto, M. Sataka, H. Kudo, A. Yamazaki, S. Sasa

Hydrogen profiling has been one of the important element analysis issues in materials science and several kinds of the profiling methods have been developed based on different kinds of ion-atom interactions. The elastic recoil process gives us a chance to detect several kinds of low Z elements simultaneously, which is inevitable to study their migration behavior influenced with each other among the low Z elements.

In the present study, 15 MeV ^{16}O ions were chosen to detect hydrogen isotopes simultaneously with reasonable depth resolution under the reflection ERDA mode. At this energy of oxygen ions, the interaction between the projectile and H(D) is governed by the non-Coulombic process, which results in larger recoil cross-sections than in the Coulomb case. The relatively large cross sections given numerically by the evaluated data-set are useful for sensitive detection of relevant elements [1]. In addition, the present energy condition of oxygen ions is also applicable to detect high Z elements with the good mass-separation under the standard RBS process [2, 3].

For reliable reflection ERDA, it is the inevitable first step to calibrate the recoil detection angles with respect to the incident beam direction. The recoil detection angle in the present ERDA was calibrated referring to the transmission ERDA spectra of hydrogen from Kapton/Al under the normal incidence of 15 MeV ^{16}O^{4+} ions. After the angle calibration of the detection system, the reflection ERDA with the same ion beam was performed on DLC (160nm thick, H:D=4:1)/Si sample with a Mylar filter (14μm) for selective stopping of reflected oxygen ions. The RBS spectra at different higher angles from the heavy elements were taken for the energy calibration in the same detection system without a Mylar filter, keeping the other experimental parameters unchanged.

Figure 1 illustrates the typical changes of leading edges in the transmitted recoil hydrogen spectra from Kapton(7.5μm)/Al(15μm) under the normal incidence of 15MeV ^{16}O^{4+} ions at non-calibrated (nominal) detection angles. In order to minimize the influence of irradiation effects on the recoil spectra of Kapton film, the integrated number of incident ions was limited to be as small as $1.5×10^{14}$ particles/cm^2 per spectrum, however, one can easily see the systematic changes of leading edge channels in the transmitted hydrogen recoil spectra. In this calibration, the recoil detection angles were scanned in the range
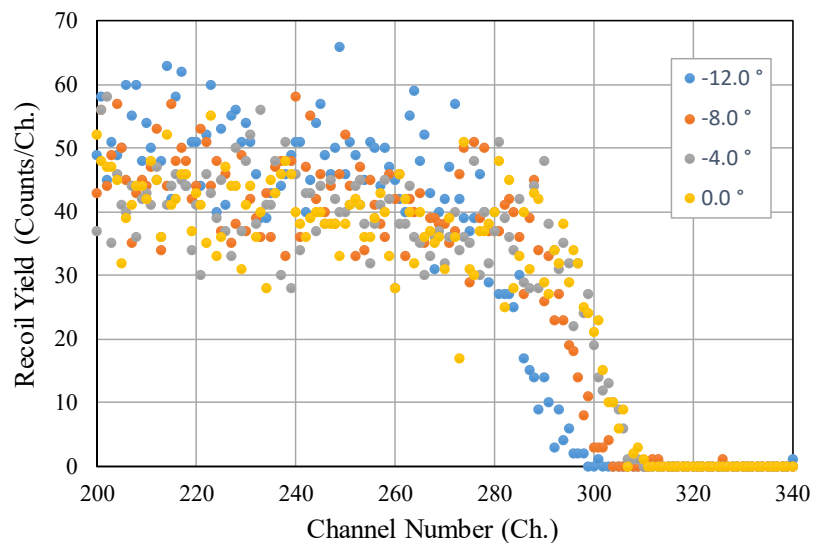
Fig. 1. Transmitted hydrogen recoil spectra under the normal incidence of 15 MeV ^{16}O^{4+} ions onto Kapton(7.5μm)/Al(15μm) film at nominal detection angles.

from −12° to +13°.

Figure 2 shows the symmetric change of leading edge positions in transmitted hydrogen recoil spectra plotted against non-calibrated detection angle with an interval of 0.2°. The real detection angle of 0° was found at the nominal angle of −1.06° assuming the symmetric change of leading edge positions. This deviation of 1.06° is small compared with the previous value of +3.13° for 8 MeV ^{4}He on the same beam line [4]. Since the angle calibration should depend sensitively on the beam transport conditions, it is recommended to perform the detection angle calibration if different beam transport conditions are employed.

Figure 3 shows the reflection ERDA spectrum at 30° from DLC(160nm thick, H:D=4:1)/Si under the oblique incidence of 15MeV ^{16}O^{4+} ions. One can see the reasonable separation of signal peaks from hydrogen and deuterium. This separation suggests a possibility of hydrogen profiling in a thicker DLC film without any peak interference. Also, one may expect appearance of an isolated ^{4}He signal peak on the higher energy side if there exists ^{4}He atoms [1]. In conclusion, it is confirmed that the employment of oxygen ions as the analyzing beam is effective for simultaneous hydrogen isotope profiling with limited influence of radiation effects compared with ERDA using much heavier ions.

Fig. 2. Recoil detection angle calibration for reflection ERDA analysis. The positions of leading edges in transmitted hydrogen spectra are plotted against nominal recoil detection angles under the normal incidence of 15 MeV ^{16}O^{4+} ions onto Kapton(7.5μm)/Al(15μm).
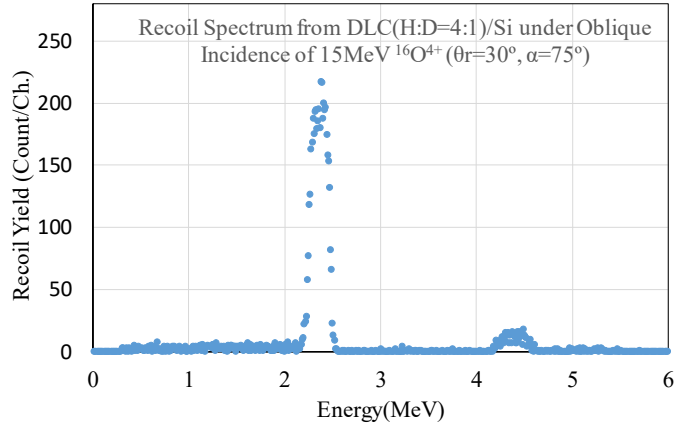
Fig. 3. Reflection recoil spectrum from DLC(160nm, H:D=4:1)/Si under the oblique incidence of 15 MV ^{16}O^{4+} ions (Θr=30°, α=75°). The peaks at higher and lower energies correspond to deuterium and hydrogen, respectively.

References

[1] E. Markina et al., Nucl. Instr. Meth. Phys. Res. B 269 (2011) 3094.

[2] M. Döbeli et al., Nucl. Instr. Meth. Phys. Res. B 63 (1992) 68.

[3] M. Nasir Khan et al., J. Appl. Phys. 86 (1999) 2307.

[4] H. Naramoto et al., UTTAC Annual Report 2017 (2018) 48.

4.6 Development of TOF−E telescope ERDA for depth profiling of light elements at UTTAC

Y. Sugisawa, D. Sekiba, I. Harayama

TOF−E telescope ERDA (Time-of-flight−energy telescope elastic recoil detection analysis) is a useful technique for quantitative depth profiling of light elements in thin films [1, 2]. In this method, the velocity and energy of the probe particle are measured in coincidence, and their relationship allows identification of the particle mass. In addition, high depth resolutions of several nanometers have been achieved by TOF−E telescope ERDA [1, 3]. This technique can be applied to the analysis of thin multilayer films. We have developed a similar system mainly for the O/N ratio determination with a depth resolution of several nanometers. This will enable us to investigate the structure of multi-layer films, in which each layer thickness is several tens of nanometers.

We installed the TOF−E telescope ERDA system at 1 MV Tandetron operated at UTTAC. Figure 1 shows the experimental setup of the scattering chamber and the TOF tube. We employed a pair of time-detectors (T1 and T2), each equipped with a micro-channel plate (MCP), and a solid state detector (SSD) with a 300 mm^2 sensitive area. T1 and T2 generate start and stop triggers, respectively, in the TOF measurement, while SSD determines the kinematic energy of the recoil particle. T1 is placed at 307 mm from the sample and the distance between the two time-detectors is 706 mm. SSD
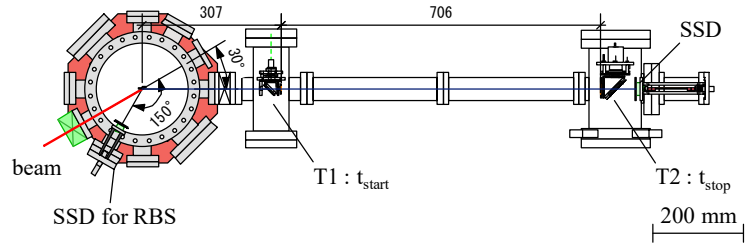
Fig. 1. Schematic view of the scattering chamber including the TOF tube. See text for arrangement of the sample.

is placed at 1092 mm from the sample, so that the SSD's effective sensitive area determines the acceptance solid angle 0.17 msr. in the measurement. In the present study, a 4 MeV $^{35}Cl^{4+}$ beam with 1×1 mm^2 size was incident on the sample at 75º from the surface normal. The recoil and backscattering angles are 30º and 150º from the beam direction, respectively. Typically, the beam current was several nA, and the data acquisition time for one sample was ~ 1 hour. The newly developed system was applied to analysis of two SiAlN films deposited on SiO$_2$ substrates. The samples were prepared under two different pressures, 0.3 and 0.5 Pa, of the process gas.

Figures 2 (a) and (b) show the two-dimensional histograms for the samples of low (0.3 Pa) and high (0.5 Pa) pressures, respectively, which were measured using the developed TOF−E telescope ERDA system. The elements assigned are also indicated in Figs. 2(a) and (b). We note that Si and Al are not distinguished. The depth profiles of elements in the films are shown in Figs. 3 (a) and (b) after recoil-energy to depth conversion using the stopping power. The interfaces between the SiAlN films and the SiO$_2$ substrates are clearly seen at about 59 and 36 nm for the two samples. This implies that the depth resolution of the newly developed system is satisfactory in the present case. Furthermore, N and O distributions are well separated. In Fig. 3(a), only N, Si and Al are recognized in the low-pressure sample,

while in Fig. 3(b) O and H, other than N, Si and Al, are recognized in the high-pressure sample. These results suggest that O and H impurities are introduced during the film deposition under the high-pressure gas. In Fig. 3(a), oxygen on the surface might be introduced by oxidation because there are no other signals associated with oxides coming from outside. Assuming that the Si/Al ratio is 9 which is estimated from the composition ratio in the sputter target, we derived the elemental composition ratios of the low- and high-pressure samples, Si : Al : N = 36.9 : 4.1 : 59 and Si : Al : N : O = 30.6 : 1.4 : 46 : 20, respectively. The depth resolution for this measurement is about 3.3 nm, which is estimated from the full width at half maximum of the surface oxygen peak in Fig. 3(a). As a next step, we are planning to apply the TOF-E telescope ERDA to three-layered films.
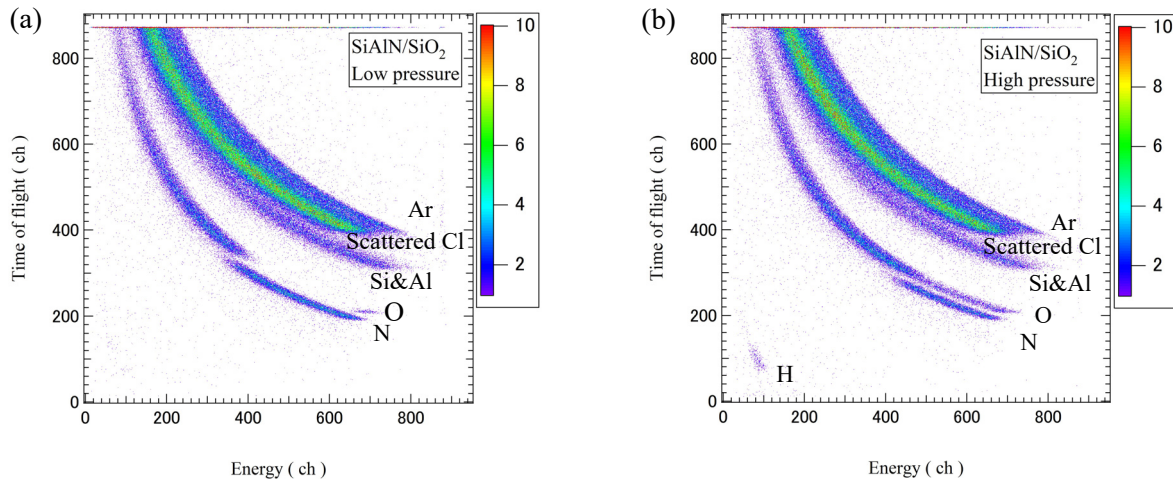
Fig. 2. Two-dimension histogram of the developed TOF−E telescope ERDA taken on SiAlN films deposited on SiO$_2$ substrates under (a) low and (b) high pressure of the process gas.
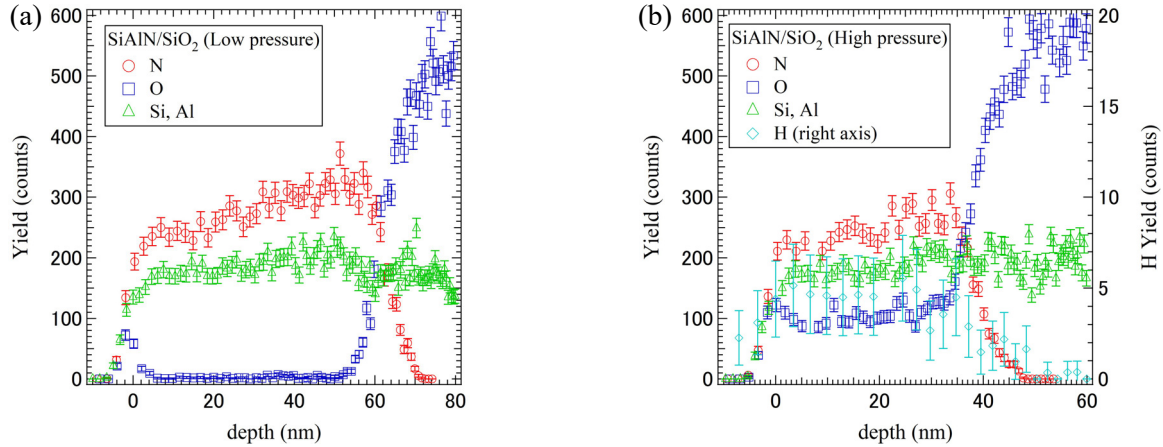
Fig. 3. Depth profiles of elements in SiAlN films deposited on SiO$_2$ substrates under (a) low and (b) high pressure of the process gas.

References

[1] M. Chicoine et al., Nucl. Instr. Meth. Phys. Res. B 406 (2017) 112.
[2] B. Brijs et al., Microelectron. Eng. 80 (2005) 106.
[3] S. Giangrandi et al., Nucl. Instr. Meth. Phys. Res. B 261 (2007) 512.

4.7 Hydrogen desorption from GaN induced by thermal plasma jet annealing

J. Kikuda, D. Sekiba

Development of a method for fabricating p-type semiconductor GaN has recently attracted much attention in the field of power electronics. While Mg is usually employed as the accepter for p-type GaN, it is known that most of the Mg atoms included in GaN do not play their required role. One of the possible reasons for this problem is the stable MgH formation of ion-implanted Mg and H, the latter of which is introduced for damage suppression. In order to remove hydrogen, various post-annealing techniques after the ion implantation have been tried. We investigated the hydrogen desorption process from GaN under the treatment of thermal plasma jet annealing (TPJ) [1]. The remained hydrogen in the GaN sample was quantified by RBS (Rutherford backscattering spectrometry)/ERDA (elastic recoil detection analysis). The effects of TPJ are discussed with a one-dimensional diffusion model.

The RBS/ERDA measurements employing 2.5 MeV ^{4}He^{2+} were carried out at the D-course of 1MV Tandetron in UTTAC. The scattering and the recoil angles were 150º and 30º with respect to the beam direction. The details of setup are described elsewhere [2]. We measured five samples: (#1) as-implanted, (#2) 10-cycle TPJ treatment, (#3) 30-cycle TPJ treatment, (#4) 50-cycle TPJ treatment and (#5) unprocessed GaN. The conditions of ion implantation and TPJ annealing are not open at present.
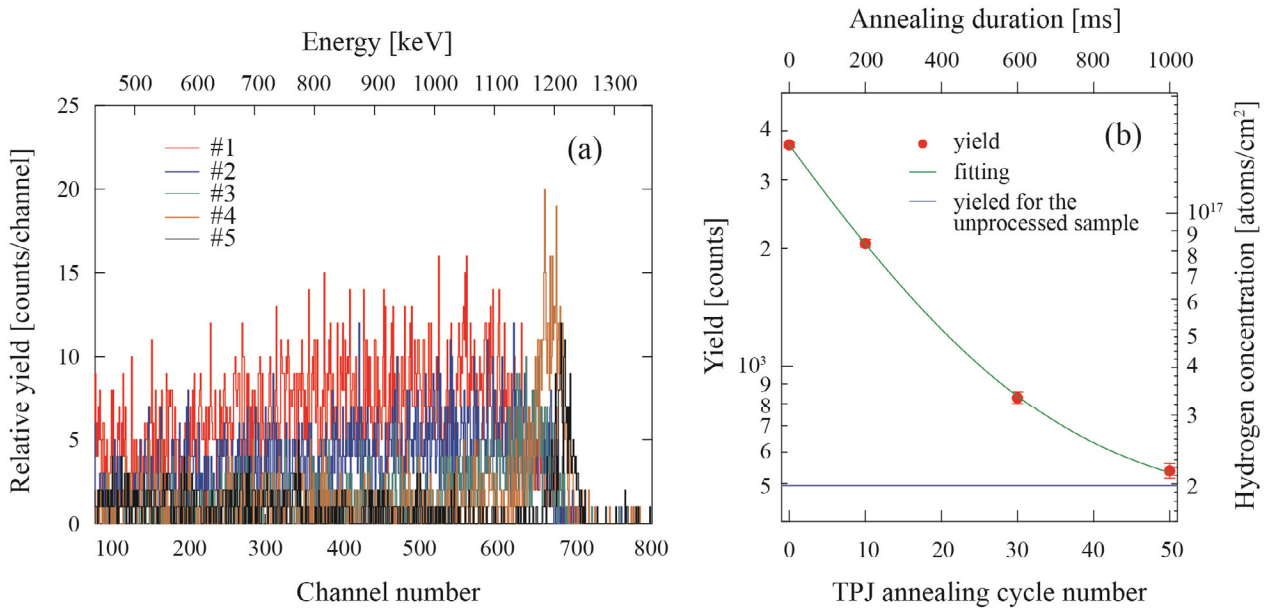
Fig. 1. (a) ERDA spectra taken for the five samples #1 ~ #5. (b) The integrated ERDA yield and fitted curves of hydrogen concentration produced from the ERDA spectra.

Figure 1(a) shows the ERDA spectra obtained for the five samples #1 ~ #5. In the spectrum for #1 (as-implanted sample), we see plateau-like yields from 350 to 600 channel. These yields decrease with increasing the TPJ annealing cycles. This behavior is more clearly seen in fig. 1(b), which shows the integrated yield from 100 to 600 channel as a function of the TPJ annealing cycle number. The horizontal

blue line, by the way, indicates the hydrogen yield obtained for the unprocessed sample, hence the unprocessed GaN substrate originally contains this amount of hydrogen. By taking into account the originally contained hydrogen, the integrated yield is well reproduced by the exponential function as $y(x) = A exp(-ax) + C$. Therefore, we see that the implanted hydrogen atoms are removed by the TPJ annealing and the hydrogen yield converges down to the original hydrogen concentration. It seems that the original hydrogen cannot be removed by ordinary annealing treatments.

One might have a question whether the non-equilibrium TPJ process corresponds to constant temperature for a certain period or the temperature rise in proportion to the cycle number. For the two cases, we applied simple one-dimensional diffusion models. For the former case, we obtained a diffusion coefficient of $D = 7.9 \times 10^{-9}$ cm^2/s. This value is not far from hydrogen diffusion coefficients determined for some typical metals that absorb hydrogen in bulk. On the other hand, we tried to plot the relation between ln D and 1/T with some assumptions of temperature increase with increasing the TPJ annealing cycles, as shown in Fig. 2. As a result, the hypothetic temperature increasing to 2000, 6000, and 10000 K gives a likely activation energy ~ 0.095 eV. The assumed temperature, however, is unlikely, because the melting point of GaN is estimated as ~ 2200 K. We may therefore conclude that the TPJ cycles play a role to keep a certain temperature, meanwhile the sample temperature could slightly increase with the TPJ cycles.
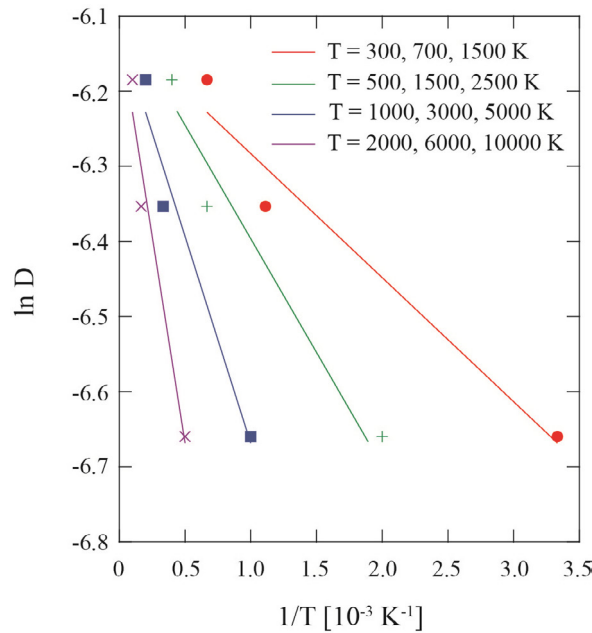
Fig. 2. Plots of the integrated yields with some assumptions of temperature increase by the TPJ cycles.

References

[1] H. Hanafusa et al., Jpn. J. Appl. Phys. 57 (2018) 06JH01.
[2] D. Sekiba et al., J. Appl. Phys. 106 (2009) 114912.

4.8 High-field Mössbauer measurements on Co-Ni spinel ferrites at successive stages of synthesis

S. Sharmin, M. Kishimoto, H. Latiff, H. Yanagihara, E. Kita

Magnetic nanoparticles with a distinctive synthesis route possess tremendous potential in technological applications for high-density information storage [1]. An understanding of the nature of anisotropy interactions in magnetic materials is often of great importance, both for unravelling the physics of these materials and for furthering the success of any technological applications. Because the hyperfine fields are usually 40–50T, the external fields must often amount to several tesla, to resolve the spectra of the opposite magnetic moments in ferrimagnetic materials [2].

We synthesized high-quality spinel cobalt-nickel ferrite nanoparticles by undergoing a succession of synthesis routes comprised of chemical co-precipitation, hydrothermal treatment, and etching in hydrochloric acid. The samples produced by chemical co-precipitation and then hydrothermal treatment are denoted by AP and HT respectively, while the samples produced as a result of etching after hydrothermal treatment are indicated by ET2 (HCl solution 2.0 mol/L), ET4 (4.0 mol/L),   and ET6 (6.0 mol/L).   Quite a difference in saturation magnetization and coercivity was obtained between the HT and ET samples from magnetization experiments, see Table 1.

Table 1. Saturation magnetization (M_s), squareness ratio (SR) and coercivity (H_c) at room temperature.

Samples	M_s (emu/g)	SR	Coercivity (Oe)
AP	21.5	0.51	4604
HT	52	0.67	4519
ET2	60.7	0.78	5605
ET3	60.4	0.77	6281
ET4	60.5	0.77	6562
ET6	59.9	0.7	6423

Mössbauer spectroscopic experiments at room temperature and 4.2 K with no applied magnetic field were first performed. However, from low-temperature data, it is not possible to distinguish the tetrahedral and octahedral sites because of the overlapping of the spectra corresponding to the two sites. Since the principal motivation for the study was to find out the fractional occupation of Fe atoms in tetrahedral and octahedral sites in the spinel Co-Ni ferrites, Mössbauer measurements under the application of an external magnetic field (5 T) were carried out on both the HT and ET2 samples and the results are shown in Fig. 1. In our configuration, the magnetic field was applied parallel to the gamma-ray direction.

With the application of the external magnetic field, the ^{57}Fe Mössbauer spectra split into two sextets corresponding to two anti-parallel sites. The outermost sextet corresponds to the site with the internal field

parallel to the applied field (resulting in a larger effective hyperfine field) and the inner sextet corresponds to the site with internal field antiparallel to the applied external magnetic field (resulting in a smaller effective hyperfine field). In usual spinel ferrites, the magnetic moments of the cations in the octahedral (B) sites are aligned parallel to the magnetic field, and the ones in the tetrahedral (A) sites are antiparallel. Because the direction of the hyperfine field is opposite to that of magnetic moments, the outer-most sextet corresponds to the tetrahedral site and the inner one corresponds to octahedral sites. The observed Mössbauer spectra were fitted by thus assuming only two sites. The obtained hyperfine parameters from the in-field Mössbauer data are shown in Table 2. One can see that there is significant variation in

Fig.1. ^{57}Fe Mössbauer spectra of HT and ET2 measured at room temperature in the presence of 5 T magnetic field applied parallel to the γ- ray direction. Dots represent the experimental data and the black solid curves show the best fit to the data.

the area between HT and ET2 samples. At tetrahedral sites, the area is more than at octahedral sites, indicating more Fe^{3+} at tetrahedral positions. However, the area decreases at the A site for the ET2 sample in comparison to that for the HT sample, while the area increases at the B site in ET2 sample as compared to that in the HT sample. Therefore, the process of etching leads to a significant variation of the Fe^{3+} distribution in the tetrahedral and octahedral sites of the Co-Ni spinel ferrite. We can conclude from the data that etching is effective for the Fe ions to occupy more octahedral sites.

Table 2. In-field Mössbauer spectra parameters of HT and ET2 samples at room temperature.

	A site (tetrahedral)				B site (octahedral)			
	Area (%)	H_{hf} (T)	Isomer shift (mm/s)	Line width (mm/s)	Area (%)	H_{hf} (T)	Isomer shift (mm/s)	Line width (mm/s)
HT	29.3	53.1	0.158	0.67	70.7	44.5	0.233	1.27
ET2	36.7	53.1	0.155	0.726	63.3	44.9	0.238	1.026

References

[1] V. Dupuis et al., MRS Online Proceedings Library Archive 1708 (2014).

[2] W. Keune, Hyperfine Interactions 204, 13-45B (2012).

4.9   Mössbauer spectra of Fe-based metallo-supramolecular polymers

T. Yoshida[1], M. Higuchi[1]

Metallo-supramolecular polymer which is formed from metal ions and organic ligands exhibits interesting functional features associated with, for example, electrochromism, ionic conductivity, and luminescence. In particular, the electrochromism is one of the promising properties to realize a new type of display [1]. Therefore, many scientists have improved the performance of electrochromic behavior of metallo-supramolecular polymer by changing metal ions and/or organic ligands.
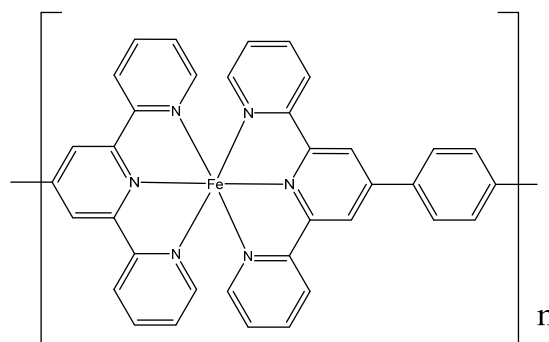
Fig. 1. Chemical structure of polymeric FeL.

It is required to establish the strategy of materials design through the study of electronic states of the relevant polymers. Here, we synthesized polymeric FeL ($[FeL]_n(OAc)_{2n}$, L = 1,4-di[[2,2':6',2"-terpyriidin]4'-yl]benzene) shown in Fig. 1, following the procedure described elsewhere [1], and carried out Mössbauer spectroscopic analysis at UTTAC.

The measured Mössbauer spectrum of discrete Fe^{2+} complex (FeL'$_2$: $[Fe(L')_2](OAc)_2$, L' = 2,2':6',2"-terpyridine), shown in Fig. 2, exhibits a clear doublet indicating that the Fe ion is in low spin Fe^{2+}. On the other hand, polymeric FeL gives an asymmetric doublet, shown in Fig. 3, which is understood in terms of the doublet of low spin Fe^{2+} superposed with the singlet of low spin Fe^{3+}, or possibly with the singlet arising from the internal magnetic field of Fe^{2+}. These results indicate that the electronic state of polymeric FeL is fluctuated comparing to the discrete Fe complex.
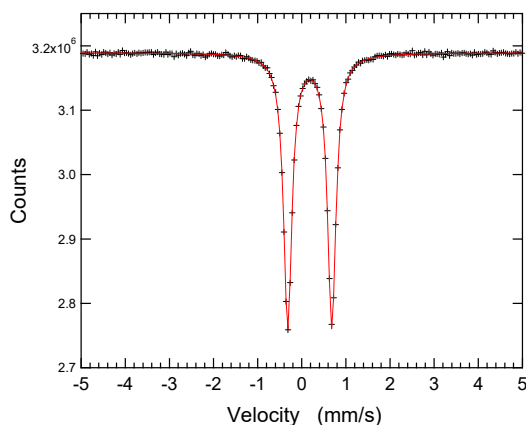
Fig. 2. Mössbauer spectrum of discrete FeL'$_2$.
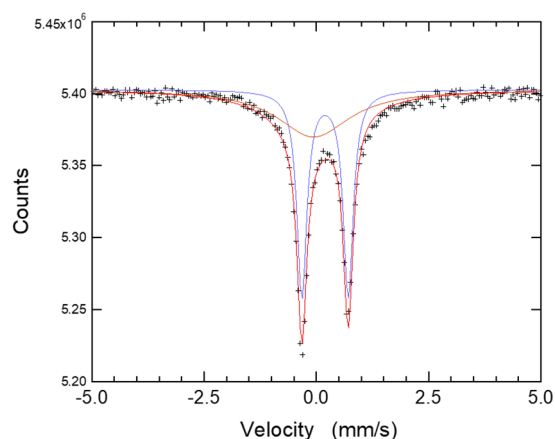
Fig. 3. Mössbauer spectrum of polymeric FeL, together with the fitted singlet and doublet curves.

Reference

[1] M. Higuchi, J. Mater. Chem. C 2 (2014) 9331.

---

[1] National Institute for Materials Science (NIMS)

4.10 Influence of oxygen introduction on magnetic properties of epitaxial NdH$_2$ thin films

D. Kutsuzawa[1], Y. Hirose[1], D. Sekiba

Rare earth hydrides have wide tunability of their physical properties, such as optical, electrical transport, and magnetic properties, by adjusting the hydrogen content [1]. A remarkable feature of fluorite-type rare earth dihydrides is their magnetism. Most of them are antiferromagnetic at low temperature owing to Fermi surface topology [2,3], while NdH$_2$ shows ferromagnetism with Curie temperature T_C of 6.8 K [4], possibly due to large magnetoelastic coupling [3]. The T_C value was suppressed by insertion of excess hydrogen (NdH$_{2+x}$) at the octahedral site with concomitant decrease of carrier density [5, 6]. Based on these observations, it has been argued that the magnetic interaction between Nd spins is mediated by conduction electrons (RKKY interaction). Oxygen doping is expected to modify the magnetic properties of NdH$_2$, because it would not only change the carrier density but also induce additional magnetic interaction between Nd ions through spatially more extended oxygen $2p$ orbital than hydrogen $1s$. Here, we synthesized NdD$_2$ epitaxial thin films doped with various amounts of oxygen, NdO$_x$D$_y$ ($0.05 \leq x \leq 1.4$) and investigated their magnetic properties.

NdO$_x$D$_y$ thin films were grown on CaF$_2$ (111) substrates by using a reactive pulsed laser deposition technique. A Nd metal plate was ablated by a KrF excimer laser. The substrate temperature was maintained at 250 °C. Note that deuterium, instead of hydrogen, was used to determine the hydrogen content in the film accurately, since the deuterium content is free from the contribution from surface adsorbed species such as water and hydrocarbon. The deuterium content y in the film was evaluated by elastic recoil detection analysis with a 2.5 MeV ^{4}He^{2+} beam (^{4}He-ERDA) conducted with the 1 MV electrostatic tandem accelerator at UTTAC. The oxygen content x in the film was determined by energy dispersive X-ray spectroscopy in conjunction with a scanning electron microscope, where the intensity was calibrated using a reference sample of which x was measured by a 38.4 MeV ^{35}Cl^{7+} beam (^{35}Cl-ERDA) using the 5 MV electrostatic tandem accelerator at the Micro Analysis Laboratory, Tandem accelerator, University of Tokyo [7]. Crystal structures of the films were determined by X-ray diffraction (XRD) with Cu Kα$_1$ radiation. Electrical transport measurements were performed by the van der Pauw method. Magnetic properties were evaluated by a superconducting quantum interference device (SQUID) magnetometer.

Figure 1(a) shows resistivity vs. temperature (ρ-T) curves of the NdO$_x$D$_y$ films with various anion compositions. All of the ρ-T curves showed metallic behavior ($d\rho/dT > 0$) in the temperature range of 2 to 300 K. The fluorite films ($x \leq 0.3$) exhibited almost the same ρ for the entire temperature range, while ρ of the mixture films ($x \geq 0.6$) increased with increasing x. The ρ-T curves of the oxygen-poor films (NdO$_{0.05}$D$_{2.0}$, NdO$_{0.1}$D$_{2.0}$ and NdO$_{0.2}$D$_{2.0}$) show a kink around 200 K, probably due to ordering of the deuterium sublattice, as observed in NdH$_{2+x}$ with a variety of hydrogen contents [6]. The kink disappeared in the fluorite film with

---

[1] The University of Tokyo

larger x (x = 0.3) and the mixture films ($x \geq$ 0.6), implying that oxygen incorporated into the deuterium site of fluorite NdD$_2$ suppressed the ordering of deuterium sublattice. The inset of Fig. 1(a) shows ρ-T curves at the low temperature region (T < 20 K), where ρ is normalized to the value at 20 K. All of the films show an abrupt drop of ρ around 10 K or lower. At this temperature, we observe in Fig. 1(b) the anomalous Hall effect with a hysteresis loop, of which the curve shape resembles the magnetization vs. magnetic field loop shown in Fig. 1(c). Therefore, we concluded that the NdO$_x$D$_y$ films underwent ferromagnetic transition at this temperature. The reduction of ρ below T_C can be attributed to suppression of electron scattering by randomly oriented spins, as reported for NdH$_{2+x}$ [4].

To discuss the influence of oxygen doping on the magnetic phase transition, we evaluated T_C from the ρ-T curves as an

Fig. 1. (a) Temperature dependence of resistivity of the NdO$_x$D$_y$ films. Inset shows the resistivity in the low temperature region ($T \leq 20$ K) normalized to the resistivity at 20 K. (b) Anomalous Hall resistivity and (c) magnetization of NdO$_{0.1}$D$_{2.0}$ film plotted against the magnetic field applied perpendicular to the film surface. (d) Temperature dependence of magnetization of the NdO$_{0.1}$D$_{2.0}$ film. Dashed lines are the results of linear fitting in the vicinity of the magnetic transition temperature. T_C was determined as an intersection point of these lines.

intersection of two linear lines obtained by fitting in the slightly higher and lower temperature regions. The T_C value deduced from the fluorite-NdO$_{0.1}$D$_{2.0}$ film was 9.6 K, which agrees well with that determined from the magnetization vs. temperature curve, i.e., T_C = 9.9 K indicated in Fig. 1(d). The least oxygen-doped film (NdO$_{0.05}$D$_{2.0}$) shows T_C of 7.4 K, which is comparable to the reported values for stoichiometric NdH$_2$ (5.6 K [8] and 6.8 K [4]). With increasing x, T_C increases and reaches 10.0 K in NdO$_{0.3}$D$_{1.6}$, in sharp contrast to NdH$_{2+x}$, in which T_C is lowered by introduction of excess hydrogen. No further increase of T_C was observed in the mixture films ($x \geq 0.6$).

References

[1] J. N. Huiberts et al., Nature 380 (1996) 231.

[2] G. Wiesinger and G. Hilscher, in Handb. Magn. Mater. (1991) 511.

[3] S. H. Liu, Solid State Commun. 61 (1987) 89.

[4] S. Senoussi et al., J. Less Common Met. 130 (1987) 55.

[5] R. C. Heckman, J. Chem. Phys. 48 (1968) 5281.

[6] J. N. Daou et al, Philos. Mag. B 65 (1992) 127.

[7] I. Harayama et al, Nucl. Instr. Meth. Phys. Res. B 384 (2016) 61.

[8] R. L. Carlin et al., J. Appl. Phys. 2634 (1982) 53.

5.

BEAM IRRADIATION EFFECT

5.1 PSoC device radiation tolerance evaluation toward space application

T. Kameda, A. Nagata

PSoC (Programmable System-on-Chis) is recently attracting more attention in space application than before because of its programming flexibility and low power consumption, however, it is necessary to evaluate its tolerance to space radiation for practical application. In this study, we choose PSoC_5LP shown in Fig. 1 and measure the SEL (Single Event Latch-up) and SEU (Single Event Upset) occurrence.
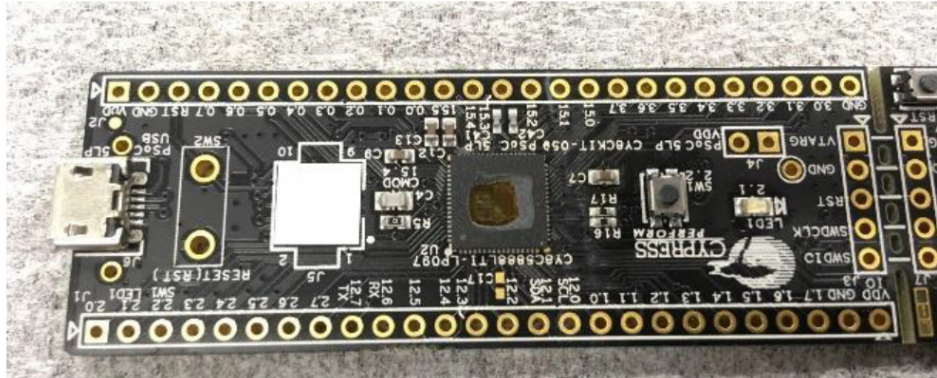
Fig. 1. PSoC_5LP used for evaluation of the radiation tolerance.

In this study, the 6MV tandem accelerator at UTTAC is used and experimental parameters for the evaluation test are shown in Table 1.

Table 1. Experimental parameters for the evaluation test.

Ion	LET [MeV/(mg/cm^2)]	Range in silicon [μm]	Charge state	Energy [MeV]
F	7.2	14.3	3+	24
Cl	17.3	14.2	7+	48

The measurement system in this study is shown in Fig. 2. The raspberry-PI based system is used for automatic measurement and data acquisition.
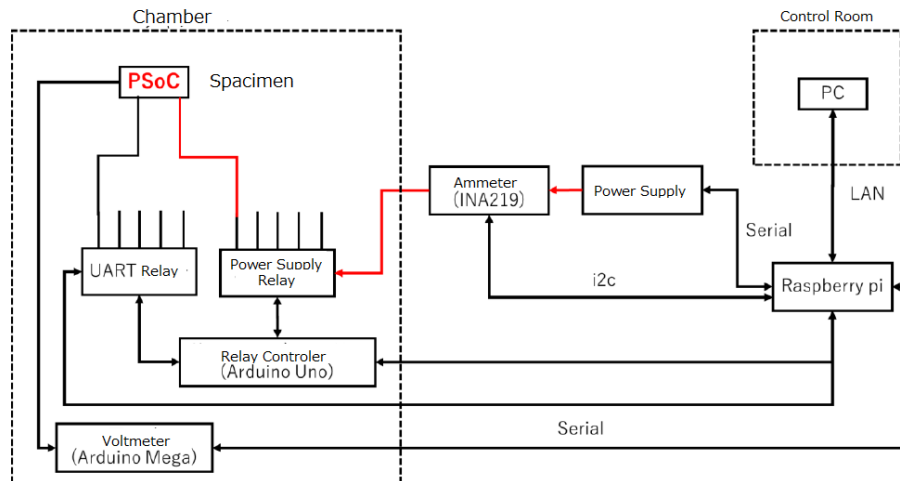
Fig. 2. Measurement system diagram.

Relationships obtained between SEL Cross-section and LET, and also between SEU Cross-section and LET are shown in Figs. 3 and 4, respectively. The test result for total SEL occurrence is shown in Table 2. Further investigation will be continued for reliability evaluation in order to conduct the conclusion.
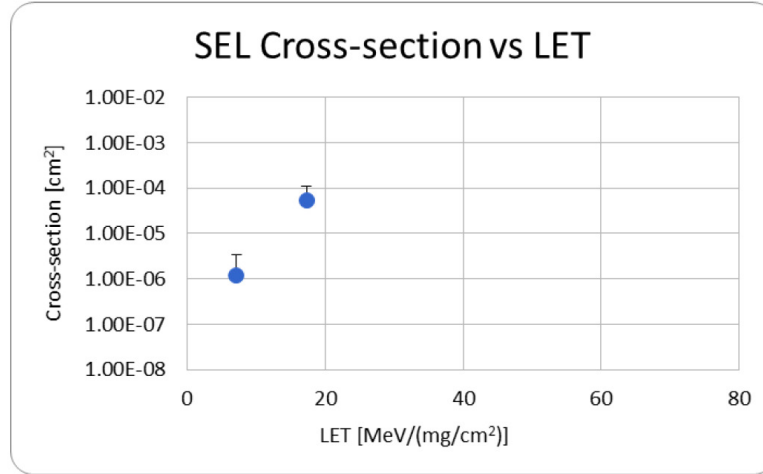
Fig. 3. SEL cross-section vs. LET.
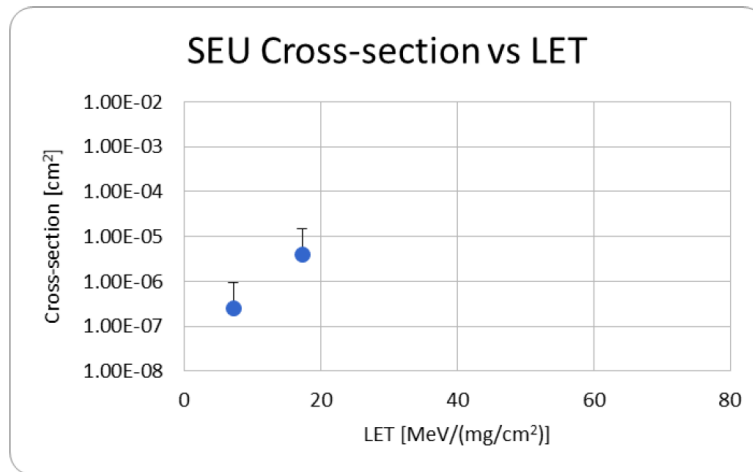
Fig. 4. SEU cross-section vs. LET.

Table 2. Total test duration and SEL occurrence.

Ion	Total test duration [min]	SEL occurrence [times]
Cl	33.0	51
F	83.1	14

References

[1] Y. Chiba, E. Asai, H. Tomioka, T. Kameda, M. Sataka, JAEA-Review 2013-057/p.73, 2014-03.

[2] Y. Chiba, E. Asai, H. Tomioka, R. Shimazu, T. Kameda, JAEA-Review 2013-059/p.13, 2014-03.

6.

LIST OF PUBLICATIONS AND PRESENTATIONS

6.1 Journals

ACCELERATOR AND RELATED FACILITIES

1. Kimikazu Sasa, Tsutomu Takahashi, Tetsuya Matsunaka, Seiji Hosoya, Masumi Matsumura, Hongtao Shen, Maki Honda, Kenta Takano, Yuta Ochiai, Aya Sakaguchi, Keisuke Sueki, Mark Stodola, and Mark Sundquist, "The 6 MV multi-nuclide AMS system at the University of Tsukuba, Japan: First performance report", Nuclear Instruments and Methods in Physics Research B 437 (2018) 98-102. [DOI: 10.1016/j.nimb.2018.09.011]

NUCLEAR AND ATOMIC PHYSICS

1. S. Iguchi, T. Moriguchi, M. Yamazaki, Y. Hori, K. Koshino, K. Toyoda, J. Teuho, S. Shimochi, Y. Terakawa, T. Fukuda, J. Takahashi, J. Nakagawara, S. Kanaya, H. Iida, "System evaluation of automated production and inhalation of 15O-labeled gaseous radiopharmaceuticals for the rapid 15O-oxygen PET examinations", European Journal of Nuclear Medicine and Molecular Imaging, 5 (2018) 37-58.

2. T. Moriguchi, A. Ozawa, Y. Yamato, S. Suzuki, M. Amano, D. Kamioka, D. Nagae, Y. Abe, "Lamb-shift Polarized ion Source at UTTAC", Proceeding of Science(PSTP2017) 018 (7 pages) (2018).

3. Y. Ito, P. Schury, M. Wada, F. Arai, H. Haba, Y. Hirayama, S. Ishizawa, D. Kaji, S. Kimura, H. Koura, M. MacCormick, H. Miyatake, J. Y. Moon, K. Morimoto, K. Morita, M. Mukai, I. Murray, T. Niwase, K. Okada, A. Ozawa, M. Rosenbusch, A. Takamine, T. Tanaka, Y. X. Watanabe, H. Wollnik, and S. Yamaki, "First Direct Mass Measurements of Nuclides around Z=100 with a Multireflection Time-of-Flight Mass Spectrograph", Phys. Rev. Lett. 120 (2018) 152501.

4. D. T. Tran, H. J. Ong, G. Hagen, T. D. Morris, N. Aoi, T. Suzuki, Y. Kanada-En'yo, L. S. Geng, S. Terashima, I. Tanihata, T. T. Nguyen, Y. Ayyad, P. Y. Chan, M. Fukuda, H. Geissel, M. N. Harakeh, T. Hashimoto, T. H. Hoang, E. Ideguchi, A. Inoue, G. R. Jansen, R. Kanungo, T. Kawabata, L. H. Khiem, W. P. Lin, K. Matsuta, M. Mihara, S. Momota, D. Nagae, N. D. Nguyen, D. Nishimura, T. Otsuka, A. Ozawa, P. P. Ren, H. Sakaguchi, C. Scheidenberger, J. Tanaka, M. Takechi, R. Wada, and T. Yamamoto, "Evidence for prevalent $Z = 6$ magic number in neutron-rich carbon isotopes", Nature communications 9 (2018) 1594.

5. C. Y. Fu, Y. H. Zhang, X. H. Zhou, M. Wang, Yu. A. Litvinov, K. Blaum, H. S. Xu, X. Xu, P. Shuai, Y. H. Lam, R. J. Chen, X. L. Yan, T. Bao, X. C. Chen, H. Chen, J. J. He, S. Kubono, D. W. Liu, R. S. Mao, X. W. Ma, M. Z. Sun, X. L. Tu, Y. M. Xing, P. Zhang, Q. Zeng, X. Zhou, W. L. Zhan,

S. Litvinov, G. Audi, T. Uesaka, Y. Yamaguchi, T. Yamaguchi, A. Ozawa, B. H. Sun, Y. Sun, and F. R. Xu, "Masses of the Tz = -3/2 nuclei ^{27}P and ^{29}S", Phys. Rev. C 98 (2018) 014315.

6. Y. H. Zhang, P. Zhang, X. H. Zhou, M. Wang, Yu. A. Litvinov, H. S. Xu, X. Xu, P. Shuai, Y. H. Lam, R. J. Chen, X. L. Yan, T. Bao, X. C. Chen, H. Chen, C. Y. Fu, J. J. He, S. Kubono, D. W. Liu, R. S. Mao, X. W. Ma, M. Z. Sun, X. L. Tu, Y. M. Xing, Q. Zeng, X. Zhou, W. L. Zhan, S. Litvinov, K. Blaum, G. Audi, T. Uesaka, Y. Yamaguchi, T. Yamaguchi, A. Ozawa, B. H. Sun, Y. Sun, and F. R. Xu, "Isochronous mass measurements of Tz = -1 fp-shell nuclei from projectile fragmentation of ^{58}Ni", Phys. Rev. C 98 (2018) 014319.

7. Y. M. Xing, K. A. Li, Y. H. Zhang, X. H. Zhou, M. Wang, Yu. A. Litvinov, K. Blaum, S. Wanajo, S. Kubono, G. Martinez-Pinedo, A. Sieverding, R. J. Chen, P. Shuai, C. Y. Fu, X. L. Yan, W. J. Huang, X. Xu, X. D. Tang, H. S. Xu, T. Bao, X. C. Chen, B. S. Gao, J. J. He, Y. H. Lam, H. F. Li, J. H. Liu, X. W. Ma, R. S. Mao, M. Si, M. Z. Sun, X. L. Tu, Q. Wang, J. C. Yang, Y. J. Yuan, Q. Zeng, P. Zhang, X. Zhou, W. L. Zhan, S. Litvinov, G. Audi, T. Uesaka, Y. Yamaguchi, T. Yamaguchi, A. Ozawa, C. Frohlich, T. Rauscher, F.-K. Thielemann, B. H. Sun, Y. Sun, A. C. Dai, and F. R. Xu, "Mass measurements of neutron-deficient Y, Zr, and Nb isotopes and their impact on rp and vp nucleosynthesis processes", Phys. Lett. B 781 (2018) 358.

8. M. Rosenbusch, Y. Ito, P. Schury, M. Wada, D. Kaji, K. Morimoto, H. Haba, S. Kimura, H. Koura, M. MacCormick, H. Miyatake, J.Y. Moon, K. Morita, I. Murray, T. Niwase, A. Ozawa, M. Reponen, A. Takamine, T. Tanaka, and H. Wollnik, "New mass anchor points for neutron-deficient heavy nuclei from direct mass measurements of radium and actinium isotopes", Phys. Rev. C 97 (2018) 064306.

ACCELERATOR MASS SPECTROMETRY

1. Tetsuya Matsunaka, Kimikazu Sasa, Tsutomu Takahashi, Seiji Hosoya, Masumi Matsumura, Yukihiko Satou, Shen Hongtao, and Keisuke Sueki, "Radiocarbon variations in tree rings since 1960 near the Tokai nuclear facility, Japan", Nuclear Instruments and Methods in Physics Research B 439 15 (2019) 64-69. [DOI: 10.1016/j.nimb.2018.12.009]

2. Tetsuya Matsunaka, Kimikazu Sasa, Seiji Hosoya, Shen Hongtao, Tsutomu Takahashi, Masumi Matsumura, and Keisuke Sueki, "Radiocarbon measurement using a gas/solid hybrid ion source and an automated sample preparation system at the University of Tsukuba", Nuclear Instruments and Methods in Physics Research B 455 (2019) 204-208. [DOI:10.1016/j.nimb.2018.11.042]

3. Aya Sakaguchi, Rui Inaba, Kimikazu Sasa, Tetsuya Matsunaka, Seiji Hosoya, Tsutomu Takahashi, Maki Honda, Hiroya Yamano, Keiichi Sasaki, Shinya Yamasaki, Tsuyoshi Watanabe, and Keisuke Sueki,

"Reconstruction of anthropogenic ^{129}I temporal variation in the Japan Sea using a coral core sample", Marine Environmental Research 142 (2018) 91-99. [DOI: 10.1016/j.marenvres.2018.09.003]

4. Seiji Hosoya, Kimikazu Sasa, Tsutomu Takahashi, Tetsuya Matsunaka, Masumi Matsumura, Hongtao Shen, Yuki Ota, Kenta Takano, Yuta Ochiai, and Keisuke Suekia, "Isobar suppression for ^{36}Cl accelerator mass spectrometry at the University of Tsukuba", Nuclear Instruments and Methods in Physics Research B 438 (2018) 131-135. [DOI: 10.1016/j.nimb.2018.07.001]

5. Michio Murakami, Takao Nirasawa, Takao Yoshikane, Keisuke Sueki, Kimikazu Sasa, and Kei Yoshimura, "Estimation of dietary intake of radionuclides and effectiveness of regulation after the Fukushima accident and in virtual nuclear power plant accident scenarios", International Journal of Environmental Research and Public Health 15(8) (2018) 1589. [DOI:10.3390/ijerph15081589]

BEAM AND ISOTOPE APPLICATIONS

1. A. Uedono, K. Sako, W. Ueno, and M. Kimur, "Free volumes introduced by fractures of CFRP probed using positron annihilation", Composites A 122 (2019) 54-58.
[DOI:10.1016/j.compoistesa.2019.04.020]

2. M. Sumiya, K. Fukuda, S. Takashima, S. Ueda, T. Onuma, T. Yamaguchi, T. Honda, and A. Uedono, "Structural disorder and in-gap states of Mg-implanted GaN films evaluated by photothermal deflection spectroscopy", J. Cryst. Growth. 511 (2019) 15-18. [DOI: 10.1016/j.jcrysgro.2019.01.021]

3. Y. Sato, S. Shibata, A. Uedono, K. Urabe, and K. Eriguchi, "Characterization of the distribution of defects introduced by plasma exposure in Si substrate", J. Vac. Sci. Technol. A 37 (2019) 011304(1-5). [DOI: 10.1116/1.5048027]

4. S. Iwashita, K. Denpoh, M. Kagaya, T. Kikuchi, N. Noro, T. Hasegawa, T. Moriya, and A. Uedono, "Ion energy control and its applicability to plasma enhanced atomic layer deposition for synthesizing titanium dioxide films", Thin Solid Films 660 (2018) 865-870. [DOI: 10.1016/j.tsf.2018.03.001]

5. P. Rajesh, S. Sellaiyan, A. Uedono, T. Arun, and R. Justin Joseyphus, "Positron Annihilation Studies on Chemically Synthesized FeCo Alloy", Sci. Reports 8 (2018) 9764(1-9). [DOI: 10.1038/s41598-018-27949-2]

6. S. F. Chichibu, A. Uedono, K. Kojima, H. Ikeda, K. Fujito, S. Takashima, M. Edo, K. Ueno, and S. Ishibashi, "The origins and properties of intrinsic nonradiative recombination centers in wide bandgap GaN and AlGaN", J. Appl. Phys. 123 (2018) 161413(1-13). [DOI: 10.1063/1.5012994]

7. K. Koike, M. Yano, S. Gonda, A. Uedono, S. Ishibashi, K. Kojima, and S. F. Chichibu, "Polarity-dependence of the defect formation in c-axis oriented ZnO by the irradiation of an 8 MeV proton beam", J. Appl. Phys. 123 (2018) 161562(1-6). [DOI: 10.1063/1.5010704]

8. A. Uedono, T. Nabatame, W. Egger, T. Koschine, C. Hugenschmidt, M. Dickmann, M. Sumiya, and S. Ishibashi, "Vacancy-type defects in Al$_2$O$_3$/GaN structure probed by monoenergetic positron beams", J. Appl. Phys. 123 (2018) 155302(1-8). [DOI: 10.1063/1.5026831]

9. S. Iwashita, T. Moriya, T. Kikuchi, M. Kagaya, N. Noro, T. Hasegawa, and A. Uedono, "Effect of ion energies on the film properties of titanium dioxides synthesized via plasma enhanced atomic layer deposition", J. Vac. Sci. Technol. A 36 (2018) 021515(1-8). [DOI: 10.1116/1.5001552]

10. H. Okumura, S. Suihkonen, J. Lemettinen, A. Uedono, Y. Zhang, D. Piedra, and T. Palacios, "AlN metal-semiconductor field-effect transistors using Si-ion implantation", Jpn. J. Appl. Phys. 57 (2018) 04FR11(1-5). [DOI: 10.7567/JJAP.57.04FR11]

11. A. Uedono, S. Takashima, M. Edo, K. Ueno, H. Matsuyama, W. Egger, T. Koschine, C. Hugenschmidt, M. Dickmann, K. Kojima, S. F. Chichibu, and S. Ishibashi, "Carrier trapping by vacancy-type defects in Mg-implanted GaN studied using monoenergetic positron beams", Phys. Stat. Sol. B255 (2018) 1700521(1-9). [DOI: 10.1002/pssb.201700521]

12. K. Shima, H. Iguchi, T. Narita, K. Kataoka, K. Kojima, A. Uedono, and S. F. Chichibu, "Room-temperature photoluminescence lifetime for the near-band-edge emission of (000^{-1}) p-type GaN fabricated by sequential ion-implantation of Mg and H", Appl. Phys. Lett. 113 (2018) 191901. [DOI:10.1063/1.5050967]

13. S. F. Chichibu, K. Shima, K. Kojima, S. Takashima, M. Edo, K. Ueno, S. Ishibashi, and, A. Uedono, "Large electron capture-cross-section of the major nonradiative recombination centers in Mg-doped GaN epilayers grown on a GaN substrate", Appl. Phys. Lett. 112 (2018) 211908(1-5). [DOI: 10.1063/1.5030645]

14. A. Uedono, T. Yamada, T. Hosoi, W. Egger, T. Koschine, C. Hugenschmidt, M. Dickmann, and H. Watanabe, "Annealing behavior of open spaces in AlON films studied by monoenergetic positron beams", Appl. Phys. Lett. 112 (2018) 182103(1-4). [DOI: 10.1063/1.5027257]

15. M. Sumiya, S. Ueda, K. Fukuda, Y. Asai, Y. Cho, L. Sang, A. Uedono, T. Sekiguchi, T. Onuma, and T. Honda, "Valence band edge tail states and band gap defect levels of GaN bulk and InxGa1−xN films detected by hard X-ray photoemission and photothermal deflection spectroscopy", APEX 11 (2018) 021002(1-4). [DOI: 10.7567/APEX.11.021002]

16. A. Uedono, T. Tanaka, N. Ito, K. Nakahara, W. Egger, C. Hugenschmidt, S. Ishibashi, and M. Sumiya, "Vacancy-Type Defects and Their Carrier Trapping Properties in GaN Studied by Monoenergetic Positron Beams", ECS Transactions, 86 (2018) 149-160. [DOI: 10.1149/08610.0149]

17. 上殿明良, "陽電子消滅による空孔型欠陥の評価", New Diamond 34 (2018) 49-52.

18. Y. Shiina, R. Kinoshita, S. Funada, M. Matsuda, M. Imai, K. Kawatsura, M. Sataka, K. Sasa, and S. Tomita, "Measurement of Auger electrons emitted through Coster-Kronig transitions under irradiation of fast C_2^+ ions", Nuclear Instruments and Methods in Physics Research B (2019) in press. [DOI: 10.1016/j.nimb.2018.10.041]

19. Akiyoshi Yamazaki, Hiroshi Naramoto, Kimikazu Sasa, Satoshi Ishii, Shigeo Tomita, Masao Sataka, Hiroshi Kudo, Masataka Ohkubo, and Akira Uedono, "Two-dimensional mapping of hydrogen and other elements in materials with microbeam-based transmission ERDA and PIXE", Nuclear Instruments and Methods in Physics Research B, (2019) in press. [DOI: 10.1016/j.nimb.2018.10.015]

20. Y. Hase, K. Satoh, A. Chiba, Y. Hirano, S. Tomita, Y. Saito, and K. Narumi, "Experimental Study on the Biological Effect of Cluster Ion Beams in Bacillus subtilis Spores", Quantum Beam Science 3 (2019) 8.

21. D. Kutsuzawa, Y. Hirose, A. Chikamatsu, S. Nakao, Y. Watahiki, I. Harayama, D. Sekiba, and T. Hasegawa, "Strain-enhanced topotactic hydrogen substitution for oxygen in $SrTiO_3$ epitaxial thin film", Applied Phys. Lett. 113 (2018) 253104.

22. A. Suzuki, Y. Hirose, T. Nakagawa, S. Fujiwara, S. Nakao, Y. Matsuo, I. Harayama, D. Sekiba, and T. Hasegawa, "Enhanced electrical conduction in anatase TaON via soft chemical lithium insertion toward electronis application", ACS Applied Nano Materials 1 (2018) 3981-3985.

23. D. Sekiba, T. Tamura, I. Harayama, Y. Watahiki, S. Ishii, K. Ozeki, and N. Fukata, "Development of high-resolution ERDA with double MCP system and determination of detection limit for H and D", Nuclear Instruments and Methods in Physics Research Section B 430 (2018) 6-10.

6.2 Reviews and books

1. 加速器ハンドブック（丸善出版）
   日本加速器学会 編（神谷 幸秀 編集委員長） 編纂委員 笹 公和
   2018 年 4 月刊行　　ISBN 978-4-621-08901-9
   執筆　7 章 2 静電加速器 P111–114、15 章 加速器質量分析 P448–449
   総ページ数　571.

2. 笹 公和，加速器質量分析法（AMS）による極微量放射性核種の高感度分析手法の開発，放射化分析研究会誌「放射化分析」 No.32, 19-22，2018 年 12 月.

6.3 Poster or oral presentations at academic meetings

1. A. Uedono, T. Tanaka, N. Ito, K. Nakahara, W. Egger, C. Hugenschmidt, S. Ishibashi, and M. Sumiya, "Vacancy-Type Defects and Their Carrier Trapping Properties in GaN Studied by Monoenergetic Positron Beams", Electro Chemical Soc. and Americas Int. Meeting Electrochem. Solis state Science, Cancun, Mexico, 2nd October 2018. (Invited)

2. A. Uedono, W. Egger, C. Hugenschmidt, and S. Ishibashi, "Carrier Trapping and Detrapping Processes in Wide Bandgap Semiconductors Studied by Positron Annihilation", Int. Conf. Positron Annihilation, Orland, USA, 19th August 2018. (Invited)

3. 上殿明良，M. M. Islam，櫻井岳暁，秋本克洋，"陽電子消滅による CIGS 薄膜中の空孔型欠陥の検出"，第 79 回応用物理学会秋季学術講演会，名古屋国際会議場，名古屋，2018 年 9 月 18 日.（招待講演）

4. 上殿明良，"学術界における量子ビーム利用－陽電子消滅法を例に－"，第 1 回量子ビームクラブ研究会，産総研，つくば，2018 年 7 月 27 日.（招待講演）

5. 上殿明良，"陽電子消滅法による p-GaN エピ層,イオン注入層の点欠陥評価"，第 149 回結晶工学分科会研究会，名古屋大学，名古屋，2018 年 6 月 15 日.（招待講演）

6. K.Sasa, "New System Setup of the 6MV Pelletron Tandem Accelerator at the Univ. of Tsukuba", 51st Symp. of North East Accel. Personnel, SNEAP2018, University of Wisconsin, Madison, USA, September 23-27, 2018. (Invited)

7. Shigeo Tomita, "Transport of convoy electrons in solid under fast molecular ion penetration", SHIM-ICACS 2018, Caen, France, July 1-6, 2018. (Invited)

8. 笹　公和，"フェムト同位体分析のための加速器質量分析システムの開発"，日本質量分析学会・日本プロテオーム学会 2018年合同大会，ホテル阪急エキスポパーク　大阪，2018年5月15-18日．（招待講演）

9. 笹　公和，"難測定核種の加速器質量分析法による高感度検出手法の開発"，第79回応用物理学会秋季学術講演会，名古屋国際会議場，名古屋，2018年9月18-21日．（招待講演）

10. 笹　公和，高橋　努，松村万寿美，高野健太，落合悠太，太田祐貴，細谷青児，本多真紀，松中哲也，坂口　綾，末木啓介，"筑波大学6 MV タンデム加速器質量分析装置における多核種AMSの技術開発"，第21回AMS シンポジウム，日本大学文理学部　百周年記念館，東京，2018年12月17-18日．（基調講演）

11. 笹　公和，"最近の加速器質量分析法の現状について"，第 57 回核化学夏の学校，旅館横倉，長野，2018 年 8 月 26-28 日．（招待講演）

12. 森口哲朗、"核物理利用者（不安定核・軽イオン）から見た教育訓練の現状と課題"，大型加速器施設の利用に関する放射線業務従事者訓練のあり方に関するワークショップ –法令改正に向けて–，大阪大学核物理研究センター，大阪，2018 年 6 月 21-22 日．（招待講演）

13. A. Ozawa, "Mass measurements in Rare-RI Ring in RIBF", Workshop on "Physics at HIAF High-Energy Beam Lines", Beihang University, Peking, P. R. China, December 13-15, 2018. (Invited)

14. S. Ishibashi, A. Uedono, H. Kino, T. Miyake, and K. Terakura, "Correlation between local structures and positron annihilation parameters for vacancy clusters in nitride semiconductor alloys", CSW2019, Tokyo, Japan, 16th January 2019.

15. S. F. Chichibu, K. Shima, K. Kojima, S. Takashima, K. Ueno, M. Edo, H. Iguchi, T. Narita, K. Kataoka, S. Ishibashi, and A. Uedono, "Room-temperature photoluminescence lifetime for the near-band-edge emission of epitaxial and ion-implanted Mg-doped GaN on GaN structures", Int. Workshop on Nitride Semiconductor 2018, Kanazawa, Japan, 13rd November 2018.

16. K. Fukuda, Y. Asai, L. Sang, A. Yoshigoe, A. Uedono, T. Onuma, T. Yamaguchi, T. Honda, and M. Sumiya, "Evaluation of Al2O3/n-, p-GaN samples by photothermal deflection spectroscopy", Int. Workshop on Nitride Semiconductor 2018, Kanazawa, Japan, 13rd November 2018.

17. Y. Asai, A. Yoshigoe, M. Sumita, A. Uedono, and M. Sumiya, "Study of the dependence of GaN surface oxidation on the crystalline plane by in-situ XPS during O_2 molecular beam irradiation", Int. Workshop on Nitride Semiconductor 2018, Kanazawa, Japan, 13rd November 2018.

18. A. Uedono, K. Sakou, and W. Ueno, "Free volume properties in epoxy resins for CFRP probed by positron annihilation", 4th Symposium on Innovative Measurement and Analysis for Structural

Materials, Tokyo Headquarters (Science Plaza) JST, Tokyo, Japan, 13rd November 2018.

19. A. Yamazaki, K. Sasa, S. Ishii, S. Tomita, H. Naramoto, M. Sataka, H. Kudo, G. Itoh, A. Hashimoto, A. Yousefi, A. Uedono, and M. Ohkubo, "Three-Dimensional Imaging of Hydrogen in Structural Materials by Transmission ERDA", 4th Symposium on Innovative Measurement and Analysis for Structural Materials, Tokyo Headquarters (Science Plaza) JST, Tokyo, Japan, 13rd November 2018.

20. K. Sakou, W. Ueno, A. Uedono, T. Ishii, Y. Takeichi, and M. Kimura, "Free volume in CFRP after tensile test probed by positron annihilation", 4th Symposium on Innovative Measurement and Analysis for Structural Materials, Tokyo Headquarters (Science Plaza) JST, Tokyo, Japan, 13rd November 2018.

21. W. Ueno, K. Sakou, A. Uedono, Y. Taniguchi, and K. Hayashi, "Temperature dependence of free volumes in bisphenol A with carbon fiber studied by positron lifetime spectroscopy", 4th Symposium on Innovative Measurement and Analysis for Structural Materials, Tokyo Headquarters (Science Plaza) JST, Tokyo, Japan, 13rd November 2018.

22. S. Iwashita, T Moriya, K. Denpoh, and A. Uedono, "Ion energy control in capacitively coupled discharges for PEALD processes", 2nd Asia-Pacific Conf. Plasma Physics, Kanazawa, Japan, 12nd November 2018.

23. K. Yuge, T. Nabatame, Y. Irokawa, A. Ohi, N. Ikeda, A. Uedono, L. Sang, Y. Koide, and T. Ohishi, "Analysis of deep traps at Al_2O_3/n-GaN interface using photo-assisted C-V measurement", 2018 Int. Conf. Solid State Devices and Materials, The Univ. Tokyo, Tokyo, Japan, 10th September 2018.

24. M. Sumiya, K. Fukuda, S. Takashima, T. Yamaguchi, T. Onuma, T. Honda, and A. Uedono, "Structural disorder and in-gap states of Mg-implanted GaN films evaluated by photothermal deflection spectroscopy", 19TH Int. Conf. Metalorganic Vapor Phase Epitaxy, Nara Kasugano Int. Forum, Nara, Japan, 3rd June 2018.

25. A. Uedono, S. Armini, R. Krause-Rehberg, and A. Wagner, "Characterization of porous low-k dielectric films by using positron annihilation", Japan Science Days, Rule University Bochum, Bochum, Germany, 5th July 2018.

26. A. Uedono, S. Takashima, M. Edo, K. Ueno, H. Matsuyama, W. Egger, T. Koschine, C. Hugenschmidt, M. Dickmann, K. Kojima, S. Chichibu, and S. Ishibashi,"Carrier Trapping Properties of Defects in Mg-implanted GaN Probed by Monoenergetic Positron Beams", 45th Int. Sym. Compound Semiconductors, 30th Int. Conf. Indium Phosphide and Related Materials, Compound Semiconductor Week 2018, Boston, USA, 30th April 2018.

27. Hidetsugu Tsuchida, Noriko Nitta, Shigeo Tomita, Kimikazu Sasa, Koichi Hirata, Hiromi Shibata, Yoichi Saitoh, Kazumasa Narumi, Atsuya Chiba, Keisuke Yamada, Yoshimi Hirano, and Yasushi Hoshino, "Formation of nano-porous surface structures by fast C_{60} beam bombardments", 10th International Symposium on Swift Heavy ions in Matter & 28th International Symposium on Atomic Collisions in solids, SHIM-ICACS Caen, France, July 1-6, 2018.

28. Shigeo Tomita, Yoko Shiina, Ryo Kinoshita, Makoto Imai, Kiyoshi Kawatsura, Makoto Matsuda, Kimikazu Sasa, and Masao Sataka, "Transport of convoy electrons in solids under fast molecular ion penetration", 10th International Symposium on Swift Heavy ions in Matter & 28th International Symposium on Atomic Collisions in solids, SHIM-ICACS Caen, France, July 1-6, 2018. (Invited)

29. Tetsuya Matsunaka, Kimikazu Sasa, Tsutomu Takahashi, Keisuke Sueki, and Hiroyuki Matsuzaki. "Pre- and post-accident C-14 levels in tree rings within 25 km of the Fukushima Dai-ichi Nuclear Nuclear Power Plant", The 23rd International Radiocarbon Conference (RADIOCARBON2018), Trondheim, Norway, June 7-22, 2018.

30. Kimikazu Sasa, Tetsuya Matsunaka, Tsutomu Takahashi, Seiji Hosoya, and Keisuke Sueki . "Performance of the New Tsukuba 6 MV AMS Facility for Radiocarbon Dating", The 23rd International Radiocarbon Conference (RADIOCARBON2018), Trondheim, Norway, June 7-22, 2018.

31. Kimikazu Sasa, Akiyoshi Yamazaki, Shigeo Tomita, Satoshi Ishii, Hiroshi Naramoto, Masao Sataka, Hiroshi Kudo, Akira Uedono, and Masataka Ohkubo, "Accelerator Facilities for Ion Beam Analysis of Structural Materials", The 4th Symposium on Innovative measurement and analysis for structural materials (SIP-IMASM 2018), Tokyo Headquarters (Science Plaza), Japan Science and Technology Agency (JST), Tokyo, Japan, November 13-15, 2018.

32. Y. Shiina, S. Tomita, R. Kinoshita, M. Imai, K. Kawatsura, M. Matsuda, K. Sasa, and M. Sataka, "Coster-Kronig transition of fast cluster ions studied by zero-degree electron specctroscopy", SHIM-ICACS 2018, Caen, France, July 1-6, 2018.

33. Akiyoshi Yamazaki, Kimikazu Sasa, Satoshi Ishii, Shigeo Tomita, Hiroshi Naramoto, Masao Sataka, Hiroshi Kudo, Toshihito Ohmi, Go Ozeki, A. Toshimitsu Yokobori, Jr. , Goroh Itoh, Akira Uedono, and Masataka Ohkubo, "Direct Detection and Mapping of Hydrogen in Structural Materials Using Ion Microbeams", The 4th Symposium on Innovative measurement and analysis for structural materials (SIP-IMASM 2018), Tokyo Headquarters (Science Plaza), Japan Science and Technology Agency (JST), Tokyo, Japan, November 13-15, 2018.

34. T. Moriguchi, "Reaction cross-section measurement with a proton target", The workshop on "Proton and Neutron Densities and Radii in Nuclei and Related Topics", Beihang University, Peking, China, December 17-19, 2018.

35. M. Mukai, "Development of a multi-segmented proportional gas counter for beta-decay spectroscopy at KISS" EMIS2018, CERN, September 16-21, 2018.

36. D. Kamioka, "Developments of time-of-flight detector for mass measurements with the Rare-RI Ring", Fifth Joint Meeting of the Nuclear Physics Division of the American Physics Society and the Physical Society of Japan, HAWII 2018, Hilton Waikoloa, Hawaii, USA, Octorber 23-27 2018.

37. 上殿明良，高島信也，江戸雅晴，上野勝典，松山秀昭，W. Egger, T. Koschine, C. Hugenschmidt, M. Dickmann，小島一信，秩父重英，石橋章司，"陽電子を用いたイオン注入 GaN の空孔型欠陥の評価"，SIP 次世代パワーエレクトロニクス公開シンポジウム，東京ガーデンテラス紀尾井町，東京，2019 年 3 月 29 日．

38. 高島信也，上野勝典，田中　亮，松山秀昭，江戸雅晴，嶋　紘平，小島一信，秩父重英，上殿明良，"容量測定を用いた p-GaN エピへの低濃度 Mg 注入と共注入影響の評価"，第 66 回応用物理学会春季学術講演会，東工大，東京，2019 年 3 月 11 日．

39. 秩父重英，嶋　紘平，井口紘子，成田哲生，片岡恵太，小島一信，上殿明良，"注入深さ・極性面の異なる Mg イオン注入 GaN のフォトルミネッセンス"，第 66 回応用物理学会春季学術講演会，東工大，東京，2019 年 3 月 11 日．

40. 秩父重英，嶋　紘平，小島一信，高島信也，上野勝典，江戸雅晴，井口紘子，成田哲生，片岡恵太，石橋章司，上殿明良，"エピタキシャル成長およびイオン注入 Mg 添加 GaN 中の非輻射再結合中心"，第 216 回研究集会　シリコンテクノロジー分科会，大阪大学中之島センター，大阪，2019 年 2 月 28 日．

41. 山崎明義，笹　公和，石井　聡，冨田成夫，楢本　洋，左高正雄，工藤　博，伊藤吾朗，橋本　明, Afshin Yousefi，大見敏仁，尾関　郷，横堀壽光，上殿明良，大久保雅隆，"集束イオンビームを用いた構造材料中の水素分析　〜手法と測定例〜"，　第 4 回革新的構造材料　先端計測拠点　国際会議・国際連携会議，科学技術振興機構　東京本部（サイエンスプラザ），東京，2018 年 11 月 13 日．

42. 秩父重英，小島一信，小池一歩，矢野満明，權田俊一，石橋章司，上殿明良，"高純度 ZnO 中の SRH 型非輻射再結合中心の起源と捕獲断面積"，第 79 回応用物理学会秋季学術講演会，名古屋国際会議場，名古屋，2018 年 9 月 20 日．

43. 松木伸行，松井卓矢，満汐孝治，ブライアン オローク，大島永康，上殿明良，"a-Si:H/c-Si ヘテロ界面近傍のボイド構造解析 –a-Si:H 中の陽電子消滅に対するドーピングの影響–"，第 79 回応用物理学会秋季学術講演会，名古屋国際会議場，名古屋，2018 年 9 月 20 日．

44. 福田清貴，浅井祐哉，関　慶祐，Sang Liwen，吉越章隆，上殿明良，石垣隆正，尾沼猛儀，山口智広，本田　徹，角谷正友，"Al_2O_3/n-, p-GaN 構造の光熱偏向分光法による評価"，第 79 回応用物理学会秋季学術講演会，名古屋国際会議場，名古屋，2018 年 9 月 19 日．

45. 浅井祐哉，関　慶祐，吉越章隆，隅田真人，石垣隆正，上殿明良，角谷正友，"分子線酸素ビーム照射下その場観察 XPS による GaN 表面酸化の面方位依存性"，第 79 回応用物理学会秋季学術講演会，名古屋国際会議場，名古屋，2018 年 9 月 19 日．

46. 福田清貴，高島信也，尾沼猛儀，山口智広，本田　徹，上殿明良，角谷正友，"光熱偏向分光法による Mg イオン注入 GaN 層の評価"，第 79 回応用物理学会秋季学術講演会，名古屋国際会議場，名古屋，2018 年 9 月 19 日．

47. 山下雄大，佐藤拓磨，都甲　薫，上殿明良，末益　崇，"化合物カルコゲナイド太陽電池の最新技術 - CIGS 系・CZTS 系・CTS 系太陽電池の高効率化とその課題 -"，第 79 回応用物理学会秋季学術講演会，名古屋国際会議場，名古屋，2018 年 9 月 19 日．

48. 角谷正友，福田清貴，上田茂典，浅井祐哉，Cho Yujin，関口隆史，上殿明良，尾沼猛儀，Sang Liwen，山口智広，本田　徹，　"III-V 族窒化物の価電子帯構造およびギャップ内準位の評価"，第 79 回応用物理学会秋季学術講演会，名古屋国際会議場，名古屋，2018 年 9 月 20 日．

49. 笹　公和，石井　聡，大島弘行，高橋　努，田島義一，大和良広，松村万寿美，森口哲朗，関場大一郎，上殿明良，"筑波大学タンデム加速器施設 UTTAC の現状（2017 年度）"，第 31 回「タンデム加速器及びその周辺技術の研究会」，東京都市大学，東京，2018 年 7 月 13 日．

50. 清水美智子，R. Álvarez-Asencio，N. Nordgren，上殿明良，"水処理膜への応用を目指した CNF/CA 複合膜の作製と特性解析"，セルロース学会第 25 回年次大会，京都大学，京都，2018 年 7 月 5 日．

51. A. Uedono, "Vacancy-type defects in hydrogen implanted GaN probed by positron annihilation" Workshop on Plasma and Material Science, Univ. of Tsukuba, Tsukuba, 14th March 2019.

52. A. Uedono, "University of Tsukuba Campus-in-Campus program with University of Grenoble Alpes", Japan Academic Network, Lyon, France, 21th November 2018.

53. A. Uedono, "Characterization of materials for semiconductor devices by means of positron annihilation -Vacancy-type defects in metals, insulators, and semiconductors-" Seminar, Technische Univ. München, 9th July 2018.

54. 笹　公和，石井　聡，高橋　努，大和良広，田島義一，森口哲朗，上殿明良，"筑波大学タンデム加速器施設の現状報告"，第15回日本加速器学会年会，ハイブ長岡，長岡，2018年8月8-10日．

55. 笹　公和，細谷青児，高橋　努，高野健太，落合悠太，大浦泰嗣，末木啓介，"6 MV タンデム加速器質量分析装置における難測定核種 ^{41}Ca の高感度検出技術の進展"，日本原子力学会 2018 年秋の大会，岡山大学，岡山，2018 年 9 月 5-7 日．

56. 村尾吉輝，新田紀子，土田秀次，冨田成夫，笹　公和，平田浩一，柴田裕実，平野貴美，山田圭介，千葉敦也，斉藤勇一，鳴海一雅，星野　靖，"C$_{60}$クラスターイオンビームを照射したSiとGeの表面構造評価"，日本金属学会 2019年春期大会，東京電機大学，東京，2019年3月20-22日．

57. 村尾吉輝，新田紀子，土田秀次，冨田成夫，笹　公和，平田浩一，柴田裕実，星野　靖，平野貴美，山田圭介，千葉敦也，斉藤勇一，鳴海一雅，"C$_{60}$クラスターイオンビームを照射したSiとGeの表面構造"，QST高崎サイエンスフェスタ2018，高崎シティーギャラリー，高崎，2018年12月11-12日．

58. 村尾吉輝，新田紀子，土田秀次，冨田成夫，笹　公和，平田浩一，柴田裕実，平野貴美，山田圭介，千葉敦也，斉藤勇一，鳴海一雅，星野　靖，"クラスターイオンを照射したSiとGeの形状比較"，ナノテク研シンポジウム2018，高知工科大学，高知，2018年11月3日．

59. Tetsuya Matsunaka, Seiya Nagao, Mutsuo Inoue, Shinya Ochiai, Takami Morita, Shizuho Miki, Takafumi Aramaki, Isao Kudo, Naoto Honda, Tetsutaro Takikawa, Kimikazu Sasa, Maki Honda, and Keisuke Sueki, "Anthropogenic iodine-129 in the Japan Sea Bottom Water and Dense Shelf Water of Okhotsk Sea"，日本地球惑星科学連合 2018 年大会，幕張メッセ，千葉，2018 年 5 月 20-24 日．国際会議

60. 池端　慶，服部浩一，三橋武史，黒澤正紀，小室光世，笹　公和，石井　聡，三好陽子，島田和彦，戸塚修平，石橋純一郎，"中部沖縄トラフ伊平屋北海丘熱水域海底下の熱水変質鉱物の地球化学的特徴"，2018 年度資源地質学会年会，東京大学小柴ホール，東京，2018 年 6 月 27-29 日．

61. 松中哲也，長尾誠也，井上睦夫，落合伸也，笹　公和，森田貴己，三木志津帆，本多直人，工藤　勲，滝川哲太郎，荒巻能史，本多真紀，末木啓介，"ヨウ素 129 を用いた日本海における海洋循環研究"，2018 年放射化学会年会，京都大学，京都，2018 年 9 月 18-20 日．

62. 松村万寿美，笹　公和，高橋　努，松中哲也，高野健太，落合悠太，横山大輝，末木 啓介，"筑波大学におけるヨウ素 129 の AMS 測定性能（2018 年度）"，第 21 回 AMS シンポジウム，日本大学文理学部 百周年記念館，東京，2018 年 12 月 17-18 日．

63. 高野健太，笹　公和，高橋　努，松村万寿美，落合悠太，末木啓介，三宅芙沙，堀内一穂，松崎浩之，"宇宙線イベントにおける南極ドームふじアイスコア中の宇宙線生成核種 ^{36}Cl 変動"，第 21 回 AMS シンポジウム，日本大学文理学部 百周年記念館，東京，2018 年 12 月 17-

18 日.

64. 落合悠太, 笹　公和, 戸崎裕貴, 高橋　努, 松村万寿美, 高野健太, 太田祐貴, 末木啓介, "つくば市における宇宙線生成核種 ^{10}Be, ^{36}Cl の降下フラックス変動評価", 第 21 回 AMS シンポジウム, 日本大学文理学部　百周年記念館, 東京, 2018 年 12 月 17-18 日.

65. 松中哲也, 長尾誠也, 井上睦夫, 落合伸也, 笹　公和, 高橋　努, 本多真紀, 末木啓介, 森田貴己, 三木志津帆, 本多直人, 荒巻能史, "2017-2018 年における日本海固有水中のヨウ素 129 分布", 第 21 回 AMS シンポジウム, 日本大学文理学部　百周年記念館, 東京, 2018 年 12 月 17-18 日.

66. 横山大輝, 末木啓介, 笹　公和, 松中哲也, 高橋　努, 松村万寿美, 高野健太,　落合悠太, 長谷川　涼, 太田祐貴, "福島県の帰還困難区域における I-129 の分布状況", 第 21 回 AMS シンポジウム, 日本大学文理学部　百周年記念館, 東京, 2018 年 12 月 17-18 日.

67. 松中哲也, 笹　公和, 松村万寿美, 平尾茂一, 脇山義史, "I-129/Cs-137 比を用いた新田川における放射性のヨウ素とセシウムの動態解析", 第 5 回福島大学環境放射能研究所成果報告会「避難区域の再生~現状とこれから~」, 福島大学, 福島, 2019 年 3 月 14-15 日.

68. 笹　公和, 細谷青児, 本多真紀, 高橋　努, 佐藤志彦, 高野健太, 落合悠太, 末木啓介, "加速器質量分析法によるストロンチウム 90 の迅速かつ高感度な検出手法の開発", 2018 年度　日本地球化学会年会第 65 回年会, 琉球大学, 沖縄, 2018 年 9 月 11-13 日.

69. 落合悠太, 笹　公和, 戸崎裕貴, 高橋　努, 松村万寿美, 高野健太, 太田祐貴, 末木啓介, "加速器質量分析法を用いた宇宙線生成核種 ^{36}Cl の降下フラックス変動評価", 2018 年度　日本地球化学会年会第 65 回年会, 琉球大学, 沖縄, 2018 年 9 月 11-13 日.

70. 高野健太, 笹　公和, 高橋　努, 松村万寿美, 落合悠太, 末木啓介, 三宅芙沙, 堀内一穂, 松崎浩之, "宇宙線生成核種 ^{10}Be と ^{36}Cl を用いた 5480 BC 宇宙線イベントの原因解明に向けた研究", 2018 年度　日本地球化学会年会第 65 回年会, 琉球大学, 沖縄, 2018 年 9 月 11-13 日.

71. 平田浩一, 山田圭介, 斎藤勇一, 鳴海一雅, 千葉敦也, 平野貴美, 冨田成夫, 笹　公和, "高感度微小領域分析を目指した高速クラスターイオン照射の高度化", 日本物理学会第 74 回年次大会, 九州大学（伊都キャンパス）, 福岡, 2019 年 3 月 14～17 日.

72. 坂口　綾, 浅井駿佑, 山﨑信哉, 笹　公和, 高橋　努, 落合悠太, Ismail Md. Mofizur Rahman, 末木啓介, "環境中 ^{90}Sr 測定における加速器質量分析の性能評価", 第 5 回福島大学環境放射能研究所成果報告会「避難区域の再生~現状とこれから~」, 福島大学, 福島, 2019 年 3 月 14-

15 日.

73. 森口哲朗, "筑波大学 6MV タンデム加速器施設における偏極陽子ビームを用いた核モーメントの測定", 第 10 回 停止・低速 RI ビームを用いた核分光研究会, 九州大学伊都キャンパス, 福岡, 2019 年 03 月 18-19 日.

74. 森口哲朗, "固体水素標的を用いた ^{17}Ne の反応断面積測定", 日本物理学会第 74 回年次大会、九州大学伊都キャンパス, 福岡, 2019 年 03 月 14-17 日.

75. 森口哲朗, "固体水素標的を用いた不安定核のスキン厚導出手法の開発", H29 年度 HIMAC 共同利用研究成果発表会, ホテルポートプラザ千葉, 千葉, 2018 年 4 月 16-17 日.

76. 向井もも, "稀少 RI リングにおける中性子過剰 Ni 領域の質量測定", 核データと重元素合成を中心とする宇宙核物理研究会, 北海道大学、札幌, 2019 年 3 月 6-8 日.

6.4   UTTAC seminars

2018.11.8   β-γ spectroscopy of neutron-rich nucleus ^{195}Os, *Murad Ahmed* (*University of Tsukuba*)

2018.11.26   Measurement of the sixth order cumulant of net-charge distributions in Au+Au collisions at the STAR experiment, *Tetsuro Sugiura* (*University of Tsukuba*)

2018.12.3   Study of event-plane dependent di-hadron correlations with event shape engineering at the STAR experiment, *Ryo Aoyama* (*University of Tsukuba*)

2018.12.4   Measurements of inclusive charged jet properties in pp and Pb-Pb collisions at $\sqrt{s_{NN}}$ = 5.02 TeV with the ALICE experiment at the LHC, *Ritsuya Hosokawa* (*University of Tsukuba*)

2018.12.12   Nuclear magnetic moment of neutron-rich nucleus ^{21}O, *Yoko Ishibashi* (*CYRIC, Tohoku University*)

2019.1.15   Study of directed flow to clarify the structure of the first-order phase transition in $\sqrt{s_{NN}}$ = 4.5 GeV Au+Au collisions at the STAR Fixed Target experiment, *Hiroki Kato* (*University of Tsukuba*)

2019.1.15   Study of transverse momentum and multiplicity dependence of heavy-flavour production via single electrons in pp collisions at $\sqrt{s}$ = 13 TeV with ALICE at the LHC, *Toma Suzuki* (*University of Tsukuba*)

2019.1.15   Measurement of electrons and jets from heavy flavour in pp collisions at $\sqrt{s}$ = 5.02 TeV and p-Pb collisions at $\sqrt{s_{NN}}$ = 8.16 TeV with ALICE at the LHC, *Daichi Kawana* (*University of Tsukuba*)

2019.1.15   Azimuthal angle dependence of quantum interferometry relative to the event plane in $\sqrt{s_{NN}}$ = 200 GeV Au+Au and Cu+Au collisions at RHIC-STAR, *Yota Kawamura* (*University of Tsukuba*)

2019.1.16   Study of cosmic ray events and measurements of cosmogenic radionuclide ^{36}Cl by accelerator mass spectrometry, *Kenta Takano* (*University of Tsukuba*)

2019.1.16   Development of time-of-flight detector and position-sensitive detector using secondary electrons emitted from a thin foil, *Daiki Kamioka* (*University of Tsukuba*)

2019.1.16   Measurement of multiplicity dependent di-hadron correlations in $\sqrt{s_{NN}}$ = 200 GeV d+Au collisions at STAR, *Kazuya Nakagawa* (*University of Tsukuba*)

7.

THESES

Doctor theses

Murad Ahmed   β-γ spectroscopy of neutron-rich nucleus ^{195}Os

Yoko Ishibashi   Nuclear magnetic moment of neutron-rich nucleus ^{21}O

Yoko Shiina   Response of electrons in solid under irradiation of fast cluster ions

Master theses

Daiki Kamioka   Development of time-of-flight detector and position-sensitive detector using secondary electrons emitted from a thin foil

Kenta Takano   Study of cosmic ray events and measurements of cosmogenic radionuclide ^{36}Cl by accelerator mass spectrometry

Yuki Ota   Evaluation of ^{36}Cl in soil around Fukushima Daiichi nuclear power plant using AMS

Junichi Kikuda   Observation of hydrogen in *p*-type GaN using RBS/ERDA and channeling NRA

Naoka Hiruta   Beam optics analysis of hydrogen recoils in high-resolution ERDA

Yuki Sugisawa   Development of TOF-E telescope ERDA for light element quantification in multi-layer films

Undergraduate theses

Yusuke Iwai   Detection of 10-100 keV particles using Superconducting Tunnel Junction

Hiroki Yokoyama   Distribution of ^{129}I inventory in difficult-to-return zones in Fukushima Prefecture

Shunsuke Asai   Development/improvements of analytical technique for Sr-90 measurement using AMS

8.

LIST OF PERSONNEL

Tandem Accelerator Complex

A. Uedono	Director, Professor
K. Sasa	Associate Professor
D. Sekiba	Lecturer
T. Moriguchi	Assistant Professor
Y. Tajima	Mechanical Engineer
S. Ishii	Mechanical Engineer
T. Takahashi	Electrical Engineer
Y. Yamato	Electrical Engineer
M. Matsumura	Technical Assistant
S. Kuramochi	Administrative Staff
M. Satoh	Administrative Staff
H. Muromachi	Administrative Staff

Research Members[1]

Division of Physics

A. Ozawa	T. Moriguchi	K. Sasa	S. Suzuki
T. Yamaguchi*	M. Mukai		

Division of Applied Physics

E. Kita	D. Sekiba	S. Sharmin	S. Tomita
A. Uedono	H. Yanagihara	M. Ohkubo**	

Division of Geoscience

M. Kurosawa	K. Ikehata

Division of Chemistry

K. Sueki	A. Sakaguchi	S. Yamasaki

Division of Information and Systems

T. Kameda

---

[1] The "research members" include the authors and coauthors within 5 years back from this fiscal year, as well as the members of research projects running at UTTAC.
* Cross appointment from Saitama University.
**Visiting Prcofessor from National Institute of Advanced Industrial Science and Technology [AIST].

Staff of Open Advanced Facilities Initiative

H. Kudo	H. Naramoto	M. Sataka

K. Awazu (National Institute of Advanced Industrial Science and Technology [AIST])

S. Aoki (Comprehensive Research Organization for Science and Society [CROSS])

Staff of Joint Research Projects with Other Organizations

A. Yamazaki (Cross-ministerial Strategic Innovation Promotion Program [SIP])[2]

Graduate students

Graduate School of Pure and Applied Sciences

Graduate School of Life and Environmental Sciences

M. Ahmed	Y. Shiina	Y. Liu	H. Latiff
Y. Hisamatsu	T. Tainosho		
D. Kamioka	K. Takano	Y. Ochiai	R. Kagesawa
H. Onoda	H. Koizumi	R. Shigesawa	M. Hagiwara
T. Itou	A. Ogura	N. Onozato	Y. Ota
Y. Sugisawa	J. Kikuda	A. Nagata	A. Yasuda
M. Hashimoto	M. Date	K. Hattori	Y. Asai
R. Mase	S. Yaguchi	W. Ueno	S. Ando
R. Suganuma			

Undergraduates

A. Taira	S. Yamada	Y. Iwai	K. Kimura
R. Abe	T. Okamoto	S. Asai	H. Yokoyama
Y. Takahara	R. Yaguchi		

External users and collaborators

Y. Tosaki	National Institute of Advanced Industrial Science and Technology (AIST)
K. Hirata	National Institute of Advanced Industrial Science and Technology (AIST)
S. Shiki	National Institute of Advanced Industrial Science and Technology (AIST)
S. Yamashita	The University of Tokyo
Y. Katou	The University of Tokyo
N. Nagakura	The University of Tokyo
K. Fujii	The University of Tokyo

---

[2] Also, a staff of *Open Advanced Facilities Initiative*

S. Kajiwara   The University of Tokyo

T. Mogi   The University of Tokyo

Y. Hirose   The University of Tokyo

D. Kutsuzawa   The University of Tokyo

T.Wakasugi   The University of Tokyo

T. Matsunaka   Kanazawa University

H. Arakawa   Saitama University

K. Inomata   Saitama University

K. Nishimuro   Saitama University

T. Kobayashi   Saitama University

Y. Inada   Saitama University

S. Hosoi   Saitama University

M. Sakaue   Saitama University

K. Yokota   Saitama University